

Control of Bionanoparticles with Electric Fields

Dissertation
zur Erlangung des Doktorgrades
an der Fakultät für Mathematik, Informatik und Naturwissenschaften
Fachbereich Physik
der Universität Hamburg

vorgelegt von

Jannik Lübke

Hamburg

2022

Gutachter/innen:

Prof. Dr. Jochen Küpper
Prof. Dr. Arwen R. Pearson

Zusammensetzung der Prüfungskommission:

Prof. Dr. Sadia Bari
Prof. Dr. Henry N. Chapman
Prof. Dr. Arwen R. Pearson
Prof. Dr. Michael Potthoff
Prof. Dr. Jochen Küpper

Vorsitzender der Prüfungskommission:

Prof. Dr. Michael Potthoff

Datum der Disputation:

12. 12. 2022

Vorsitzender des Fach-Promotionsausschusses PHYSIK:

Prof. Dr. Wolfgang J. Parak

Leiter des Fachbereichs PHYSIK:

Prof. Dr. Günter H. W. Sigl

Dekan der Fakultät MIN:

Prof. Dr.-Ing. Norbert Ritter

Summary

Single-particle imaging (SPI) is a method that promises high-resolution structure determination of artificial or biological nanoparticles, including proteins. In a thin stream, these particles are guided into the brilliant flashes of free-electron lasers. Upon interception, incoming photons diffract off randomly-oriented individual nanoparticles in the gas phase. The low-signal snapshots are then classified and combined to retrieve the real-space structure of the investigated molecules. Since this is the result from averaging over hundreds of thousands of individual images, in order to achieve atomic resolution with SPI, the nanoparticles need to be identical on the same length scales. For various reasons, biological molecules, like proteins, have structural variability. Different oligomeric or conformational states may co-exist already in solution and multiple charges, for example acquired in the process of aerosolization, deform soft proteins due to Coulomb stretching. When not accounted for, these and other morphologic deviations introduce positional ambiguity and effectively reduce the overall achievable experimental resolution. In light of these challenges, methods to characterize and control the particles to deliver high-purity particle beams in SPI experiments need to be developed.

Here I present experimental results on the production of beams of aerosolized nanoparticles with well-characterized charge- and oligomeric states and ways to modulate their charge-state distributions. Furthermore, based on computational modeling, an electrostatic deflection setup to enable the spatial separation of conformers is proposed, in which charge-neutral biological macromolecules can be separated according to their conformational states. These findings are crucial steps toward atomic-resolution imaging of identical macromolecules in the gas phase, which can be directly applied in SPI experiments.

Zusammenfassung

Single-Particle Imaging (SPI) ist eine Methode, die hochauflösende Strukturbildgebung von künstlichen oder biologischen Nanopartikeln wie Proteinen verspricht. Diese Teilchen werden in einem dünnen Strahl in die brillanten Pulse von Freie-Elektronen-Lasern gelenkt. Bei einem Treffer werden wenige Photonen an zufällig orientierten einzelnen Nanopartikeln in der Gasphase gestreut. Die signalschwachen Schnappschüsse werden klassifiziert und kombiniert, um die Raumstruktur der untersuchten Moleküle zu bestimmen. Da dies das Ergebnis der Mittelung hunderttausender einzelner Bilder ist, müssen die Nanopartikel strikt identisch sein, um mit SPI atomare Auflösung zu realisieren. Biologische Moleküle, wie zum Beispiel Proteine, weisen jedoch aus verschiedenen Gründen strukturelle Variabilität auf. Verschiedene Oligomere oder Konformationszustände können bereits in Lösung koexistieren, und Mehrfachladungen, die beispielsweise bei der Aerosolisierung entstehen, verformen flexible Proteine aufgrund Coulomb'scher Streckung. Wenn nicht berücksichtigt, führen diese und andere morphologische Abweichungen zu Positionsambiguität und verringern die experimentell erreichbare Strukturauflösung. Angesichts dieser Herausforderungen müssen Methoden zur Charakterisierung und Kontrolle der Partikel entwickelt werden, um hochreine Partikelstrahlen für SPI-Experimente zu generieren.

In dieser Arbeit werden experimentelle Ergebnisse zur Erzeugung von Strahlen aerosolierter Nanopartikel mit eingehend charakterisierten Ladungs- und Oligomerzuständen sowie Möglichkeiten zur Modulation ihrer Ladungszustandsverteilungen vorgestellt. Darüber hinaus wird auf Grundlage von Simulationen ein elektrostatischer Deflektor beschrieben, mit dem ladungsneutrale biologische Makromoleküle entsprechend ihrer Konformationszustände getrennt werden können. Diese Erkenntnisse sind entscheidende Schritte auf dem Weg zu atomar aufgelöster Bildgebung identischer Moleküle in der Gasphase, die unmittelbar in SPI-Experimenten angewendet werden können.

Contents

Acronyms	III
1. Introduction	1
2. Fundamental Concepts	5
2.1. Physical Basics	5
2.1.1. Charges, Electric Potential, Field, and Field Gradient	5
2.1.2. Interaction between Charges and Fields	6
2.1.3. Optical Scattering	9
2.2. Experimental Details	9
2.2.1. Aerosolization Concepts	10
2.2.2. Neutralizer	12
2.2.3. Scanning Mobility Particle Sizer	12
2.2.4. Particle-Beam Characterization and the Electric Deflector	15
2.3. Samples	18
2.3.1. Proteins in Solution and in the Gas Phase	18
2.3.2. Artificial Nanoparticles	19
2.4. Simulation Details	20
3. Charge-State Distribution of Aerosolized Nanoparticles	23
3.1. Introduction	23
3.2. Methods	24
3.3. Results and Discussion	24
3.4. Conclusion	28
4. Characterization and Control of the Charge-State Distribution of Neutralized Nanoparticles	29
4.1. Introduction	29
4.2. Methods	30
4.3. Results and Discussion	30
4.4. Conclusions	33
5. Size and Charge-State Purified Dense Beams of Macromolecules for Single-Particle Imaging Experiments	35
5.1. Introduction	35
5.2. Methods	36
5.3. Results and Discussion	38
5.4. Conclusion	42

6. Toward Deflection of Neutral Molecules for Single-Particle Imaging Experiments	43
6.1. Introduction	43
6.2. Methods	44
6.3. Results and Discussion	48
6.4. Conclusion	50
7. Conclusion and Outlook	51
A. Evaporation of Nanodroplets	55
A.1. Evaporation of Nanoscopic Droplets in the Gas Phase	55
B. Further Details on Light-Scattering Imaging	61
B.1. Analysis of the Scattering Signal of cw-Illuminated Particles	61
B.2. Optical Aberration	63
B.3. Particle Size Determination in the Side-View Imaging Setup	64
Publications	67
Beamtimes	69
Acknowledgments	71
Bibliography	73
Eidesstattliche Versicherung / Declaration on Oath	94

Acronyms

2D	Two-dimensional
3D	Three-dimensional
ALS	Aerodynamic-lens stack
BSA	Bovine serum albumin
CO ₂	Carbon dioxide
CPC	Condensation particle counter
cryo-EM	Cryo-electron microscopy
CSD	Charge-state distribution
cw	Continuous wave
DMA	Differential mobility analyzer
ESI	Electrospray ionization
EuXFEL	European X-ray Free-Electron Laser
FEL	Free-electron laser
FLASH	Free-Electron Laser in Hamburg
FWHM	Full width at half maximum
GDVN	Gas-dynamic virtual nozzle
IQR	Interquartile range
MS	Mass spectrometry
N ₂	Nitrogen
NMR	Nuclear magnetic resonance spectroscopy
PDB-IDs	Protein data bank identifiers
pI	Isoelectric point
PS	Polystyrene
PSD	Probabilistic size distribution
Q1,2,3	Quartiles 1, 2 (i. e., the median), and 3
SMPS	Scanning mobility particle sizer
SPI	Single-particle imaging

1. Introduction

We humans are naturally curious. The desire to understand and learn is deeply rooted in human nature and integral to our development [1], and one of the first steps to learning is asking questions. From “What do you get if you multiply six by seven?” to “How many roads must a man walk down?” to “What is the answer to life, the universe, and everything?” [42], they let us embark on a quest for knowledge, seek information, and return with answers. We organize systematically derived new bits of knowledge in the framework “science” [2]. Three scientific branches are the fields of physics, chemistry, and biology, which help us answer some of the grand challenges of society by exploring the fundamentals of matter and life. In interdisciplinary fields like medicine, they come together and enable the curing of disease, protecting from illness, or saving of lives.

For example, one of the current major medical challenges is emergent antibiotic resistance of pathogens under high evolutionary pressure [3, 4]. An increasing number of bacterial strains has developed evasion mechanisms, rendering them inert against virtually all available pharmaceutical agents [5]. Whether mutational alterations of drug targets, production of specific agent-inactivating enzymes, or expression of specialized drug-efflux membrane pumps, frequently, these mechanisms include proteins [6].

Proteins also play a role in pharmaceutical countermeasures: synthetically derived antibiotics, a class of therapeutic peptides and proteins, can be expected to show long-term effectiveness against pathogens [7–10]. The success of these laboratory-made compounds relies on identification of protein-molecular pathways, and so, the key to rational drug development is fundamental understanding of structure, function, and the form-function correlation of the involved molecules [11, 12]. The latter principle states that the structure and the function of proteins are tightly correlated. In other words, when attempting to comprehend physiological processes involving proteins or developing peptides with predicted specific function on biological targets, i. e., with predicted dynamics, one needs to learn about and understand their structure [13–15]: “It is very easy to answer many fundamental biological questions; you just look at the thing!” [16]

But how can we look at the “things”? A diffraction-limited optical microscope resolves details on length scales of few hundreds of nanometers [17], but higher performance is needed in structural biology: for distinguishing between the functional side chains of proteins, imaging resolution of 0.3 nm is required, and at 0.2 nm length scales, holes in aromatic rings can be resolved [18, 19]. Different methods have emerged over the last decades to shine light on protein structure, interaction with ligands, and protein dynamics in general. The three major players in structural biology are x-ray crystallography, nuclear magnetic resonance (NMR) methods, and, as a historically young technique, cryo-electron microscopy (cryo-EM) [20].

Since over a hundred years, x-ray crystallography helps determining structure and composition of crystals [21–24]. These crystals can be inorganic or organic: formation of protein crystals was described already in 1840 [25]. By analyzing x-ray Bragg peaks from diffraction off periodically-ordered crystals, potentially atomically-resolved structure of the

molecules within is elucidated [26]. Major achievements with this technique were discovery of DNA- [27] or ribosomal structure [28]. Also, in modified versions, protein dynamics were explored [29–31].

However, not all protein sample can be readily crystallized [32]. Furthermore, effects of confining arrangement in a crystal on structure and function of proteins were observed [33–35], and so, universal applicability of crystallographic methods for protein-structure-and-dynamics determination seems limited.

Cryo-EM is a fast-growing [36], atomic-resolution [37] imaging technique which does not rely on formation of crystals [38, 39]. Instead, the sample is studied at cryogenic temperatures in thin layers of vitreous ice, and large sets of images of electron-microscopically-imaged molecules are combined for structure determination [40]. Cryo-EM faces its own challenges, for example during sample preparation: reproducible production of vitrified sample has proven difficult and is a persistent bottleneck in the cryo-EM workflow [41, 43–45].

NMR [46, 47] has the advantage of working with non-ionizing radiation on sample in solution. With it, relaxation of magnetic spins provides information about average inter-atomic distances, and thus, sample structure is retrieved [48]. One of its drawbacks is comparatively low sensitivity [49] and fast magnetization relaxation in larger proteins, limiting this method to smaller complexes, even though research efforts have allowed structure investigation of massive biological structures [50–52].

With the help of the aforementioned methods, well over 100,000 different protein structures could be resolved on an atomic level to date [53]. This extensive experimental data, archived in the Protein Data Bank [54], for instance improved artificial-intelligence-based approaches to understanding proteins, such as the AlphaFold algorithm [55], promising high predictive power of three-dimensional (3D) protein structures from amino acid sequences. At some point, these frameworks may assist *in silico* design of new drugs [56].

As seen on the example of multi-drug resistant microbes (*vide supra*), there is a major incentive to study biomolecules: profound and detailed investigation of protein structure and dynamics is crucial for tackling some of the current challenges of society.

There are, however, gray areas on the knowledge map: many aspects about the functionality of proteins, and especially their fast dynamics, are still unknown [57–59]. One open question is: do the experimentally determined protein structures, being the basis for data-driven drug design [60], really reflect the structure of natural proteins, i. e., to which degree are physiological conditions preserved for the molecules under investigation? For example, does confinement in a crystal as used in crystallographic methods change the structure or function of a protein [33, 61]? This would significantly affect our ability to understand biological processes.

One complementary approach to the methods mentioned above for investigating biological sample, like proteins, in a quasi-native state is the single-particle imaging (SPI) initiative [62, 63]. Its basic principle is application of x-ray crystallography on the smallest possible “crystals”: individual molecules. Thus, in SPI experiments, isolated, individual nanoparticles in the gas phase are successively guided into the focused, highly intense x-ray beam generated by free-electron lasers (FELs), for example the Linac Coherent Light Source (LCLS) in Stanford, the Free-Electron Laser in Hamburg (FLASH), and the European X-ray Free-Electron Laser (EuXFEL). FELs generate brilliant x-rays by undulating relativistic electron

beams. The periodic movement of electrons results in forward emission of photons, which themselves interact with the electrons in a process called microbunching. Being now spatially separated by integer multiples of the x-ray radiation wavelength, the electrons start emitting coherent light that is guided into experimental endstations at up to MHz repetition rates [64, 65].

These pulsed x-ray photons are focused into a tight volume [66], intersecting a beam of aerosolized and individual sample molecules. When a molecule is hit by one of the pulses, the photons scatter and a diffraction snapshot of a single molecule is recorded. With each pulse having a temporal full width at half maximum of femtoseconds, i. e., 10^{-15} s, ultrafast images of undistorted molecules are acquired before they explode, which coined the term “diffraction-before-destruction” [67–69]. Each arbitrarily oriented molecule yields signal on the order of few photons [70]. Due to the inherently low signal, tens to hundreds of thousands of diffraction patterns of identical nanoparticles need to be recorded [71]. From this data, the 3D structure of the molecules is retrieved [72–76]. Over the last years, this method was employed to image the structure of artificial nanoparticles [77] and biological complexes like viruses [78, 79] and proteins [80]. On gold nanoparticles, resolution of < 3 nm could be achieved [81].

One envisioned exciting research case for SPI is resolving the structure of biological molecules along the successive structural changes of a reaction pathway, as was recently initially shown [82, 83]. Assembled one after the other, they would then show a “molecular movie” of isolated proteins in action [84, 85]. Even getting a still picture of a macromolecule, however, is not an easy feat: due to low scattering signal from nanoscopic objects, tens of thousands up to millions of individual images have to be recorded to reconstruct the structure in question. They are a collaborative result of extensive preparations, months-in-advance submission of research proposals to FEL infrastructures for so-called beamtimes, and intensive data collection and -processing at the scientific instruments of FEL facilities. In other words, successful SPI experiments call for careful planning and preparation and well-executed experimental work and theoretical analysis during and after the beamtime.

Among others, the achieved resolution, as a metric for the quality of the data, depends on the ability to expose structurally identical versions of nanoparticles to the pulsed FEL. With the approach of increasing the scattering signal by averaging over many images of copies of the same molecule, undefined atomic positions translate as uncertainty into the calculated 3D structure. An example for intermolecular morphological differences is a protein in random folding states, co-existing in the aerosolized ensemble. If the signal-to-noise ratio of each snapshot is high enough, conformational states of single molecules can be identified computationally and accounted for in data processing [83], but for weakly-scattering particles, this is difficult to achieve and resolution limitation persists. Being directly correlated with achievable resolution, structural heterogeneity of the sample is a bottleneck toward atomic-resolution SPI experiments [86].

Sources of heterogeneity in biological sample like proteins are different folding states, thermal motion, or charge-induced stretching [87–89]. Methods to filter gas-phase macromolecules and produce aerosol with increased levels of uniformity are for example explored in the context of mass spectrometry (MS), which is another technique for determining the structure of biological sample. With it, nanoparticles, like proteins, are transferred

into the gas phase and ionized, which allows precise determination of the mass-to-charge ratio of intact proteins or fragments using electric fields, for example in quadrupole mass analyzers [90]. Used as single-stage device or in combination with further characterization techniques, information about the atomic composition and structure of the particles can be inferred [91]. For example, a variation of MS is ion mobility spectrometry. Gas-phase mobility of charged sample is determined with it, extending the mass determination ability of pure MS toward analysis of conformational states of charged particles [92].

When it comes to controlling molecules and nanoparticles, their charge is a convenient handle that is not only exploited in scientific, but also in technical applications [93]. In addition, methods exist for controlling charge-neutral molecules. For example, by interacting with their dipole moments, conformers of a neutral dipeptide could be spatially separated in an electric field [94].

Preparing homogeneous sample in the gas phase is the scope of this work: how can measures of control, more specifically, using electric fields, be used on aerosolized nanoparticles to generate pure particle beams for SPI experiments?

This is detailed in the following chapters of this thesis. First, a brief overview of the fundamental concepts is given in chapter 2, providing scientific background and an overview over the methods used throughout this dissertation. The following results then focus on gas-phase sample purification and characterization with respect to charge, oligomeric states, and conformational states.

In chapter 3, I describe gas-focused liquid-jet-aerosolization of artificial nanoparticles, which are then focused into a particle beam and electrostatically deflected. The dispersed particles are detected with an optical-microscopy light-sheet method. The observed spatial distribution is analyzed and can be used to characterize the particle beam using numerical modeling. Despite not having been actively charged, significant amounts of charges on the sample were found.

Following this, in chapter 4, few charges are observed and quantified in electrospray-aerosolized artificial nanoparticles. Variation of aerosolization parameters is used to manipulate the observed charge-state distribution. Higher fractions of charge-neutral particles can be prepared this way.

Analysis of deflected particle beams as described above could be then transferred from artificial model systems to biological macromolecules. In chapter 5, a particle beam of $\text{MDa} = 1 \cdot 10^6 \text{ u}$ protein complexes with identical charge states is analyzed in regard to its oligomeric composition. Within the electrically dispersed, charge-purified beam, areas of high-purity monomeric protein complexes are identified.

In chapter 6, the focus is shifted from charged to charge-neutral particles. Numerical simulations show how in a proposed experimental setup, a beam of protein can be purified into pure conformational states based on differences in their dipole moments. This result opens the path for even more extensive species control in SPI experiments.

After an summarizing conclusion, an outlook is given in chapter 7, sketching the path toward possible future applications of SPI experiments.

2. Fundamental Concepts

This chapter provides an overview on the physical and biological concepts used throughout this thesis. Experimental and simulation details are presented.

2.1. Physical Basics

First, the necessary physical fundamentals are introduced, along with the quantities, which will be referred to in the results chapters below. If not explicitly referenced, these basics were compiled from and are described in greater detail in [95–98].

2.1.1. Charges, Electric Potential, Field, and Field Gradient

Electric charge is a fundamental property of matter. As demonstrated by Millikan [99], it is expressed as integer multiples of the elementary charge $e_0 = 1.6022 \cdot 10^{-19} \text{ C}$ and can have positive or negative sign. Electric charges produce an electric field around them, which interacts with other charges. While the potential Φ describes the necessary work to move a probe charge from infinity to a given point in the field, the electric-field magnitude E is described by the derivative of the potential. The derivative of E , i. e., the second derivative of the potential, is the field gradient ∇E :

$$\begin{aligned} E(x, y) &= \sqrt{\left(\frac{\partial\Phi}{\partial x}\right)^2 + \left(\frac{\partial\Phi}{\partial y}\right)^2} \\ \nabla E(x, y) &= \sqrt{\left(\frac{\partial E}{\partial x}\right)^2 + \left(\frac{\partial E}{\partial y}\right)^2}, \end{aligned} \tag{2.1}$$

where:

Φ	electric potential in V,
E	electric-field strength in V m^{-1} ,
∇E	electric-field gradient in V m^{-2} , and
x, y	coordinates in m.

Each of these quantities can be visualized by indicating isolines. If the direction and magnitude of the electric field are constant at each point, it is homogeneous. In contrast, two wire electrodes next to each other generate an inhomogeneous field and have a potential, field, and field gradient as shown in Figure 2.1.

When an object like a molecule has asymmetrically distributed partial charges q , i. e., it has a positively and a negatively charged side, it is considered a polar molecule. In this case, it has a permanent dipole moment μ_p , which can be calculated by averaging over the charges, spatially weighted by their corresponding x , y , and z positions in the molecular frame:

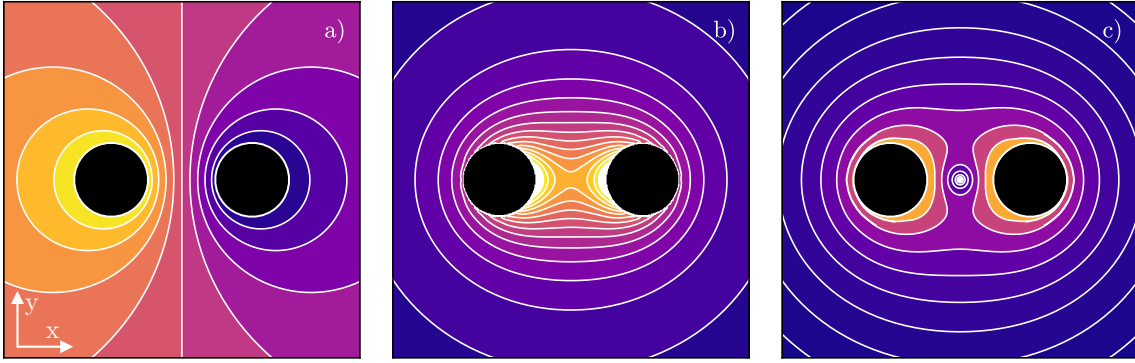


Figure 2.1.: Electrostatics between two wire electrodes, which are depicted in each panel by two solid black circles. The steps of the contour plots were chosen arbitrarily for illustrative purpose. a): Potential contours. Isopotential lines are shown in white, their density is highest between the two electrodes. b): Electric-field contours. Being the derivative of the potential, the field is strongest where the spacing between the isopotential lines in a) is smallest, which is between the electrodes. Along the white lines, the field has constant magnitude and direction. c): Field gradient, the derivative of the electric field. The contours are displayed with logarithmic spacing. In the center between the electrodes, the gradient changes approximately linearly.

$$\mu_{x,y,z} = \sum_n q_n \cdot \{x, y, z\}_n \quad (2.2)$$

$$\mu_p = \sqrt{(\mu_x^2 + \mu_y^2 + \mu_z^2)},$$

where:

- $\mu_{x,y,z}$ permanent dipole moment components in C m,
- n index of partial charge,
- q charge in C, and
- μ_p permanent dipole moment in C m.

The dipole moment is often expressed in Debye: $1 \text{ D} \approx 3.33564 \cdot 10^{-30} \text{ C m}$. In case of a protein in solution, the partial charges are associated with its amino acids: as laid out in subsection 2.3.1, its functional groups and side chains have pH-dependent ionization states. This can be used to calculate the permanent dipole moment even of very large biological molecules, based on protein data bank structures [100].

2.1.2. Interaction between Charges and Fields

Charges generate and interact with electric fields. Between two charges q_1 and q_2 acts the Coulomb force of magnitude F_C , which diminishes with the reciprocal squared distance l_{12} between the carriers:

$$F_C = \frac{q_1 q_2}{4\pi\epsilon\epsilon_0 l_{12}^2}, \quad (2.3)$$

where:

F_C	Coulomb force in N,
q	charge in C,
ε	relative permittivity without units,
ε_0	vacuum permittivity in F m^{-1} , and
l_{12}	distance between charges in m.

Depending on their polarity, this force is attractive or repulsive, as can be observed for example on a water droplet. On its surface, the Coulomb force causes charges with the same sign to repel and evenly distribute, while counteracting the surface tension of the droplet. Exceeding a maximum amount of charges q_R , called the Rayleigh limit [101], the repulsive forces destabilize the droplet and eventually cause its breakup:

$$q_R = 8\pi \cdot \sqrt{\varepsilon_0 \cdot \gamma \cdot r^3}, \quad (2.4)$$

where:

q_R	maximum charge on a droplet in C,
γ	surface tension in N m^{-1} , and
r	droplet radius in m.

In the experiments described below, the accumulated field \vec{E} from charges on electrodes were employed to accelerate (\vec{a}) and deflect charged gas-phase particles with mass m :

$$\vec{F} = q \cdot \vec{E} = m \cdot \vec{a}, \quad (2.5)$$

where:

\vec{E}	electric field in V m^{-1} ,
m	mass in kg, and
\vec{a}	acceleration in m s^{-2} .

If a molecule accommodates partial charges of opposite sign, they tend to locally displace under the influence of an external field. This displacement tendency is described by the polarizability α , which leads to the field-induced dipole moment μ_{ind} :

$$\mu_{\text{ind}} = \alpha E, \quad (2.6)$$

where:

μ_{ind}	induced dipole moment in C m and
α	polarizability in $\text{C m}^2 \text{V}^{-1}$,

which are given here as scalar values: when accounting for non-parallel orientation between μ_{ind} and the field, the dipole moment and the field are expressed as vectors, and the polarizability as rank-two tensor.

Often, polarizability is expressed as the polarizability volume:

$$\alpha' = \alpha \cdot \frac{1}{4\pi\varepsilon_0}, \quad (2.7)$$

where:

α'	polarizability volume in m^3 .
-----------	---

The polarizability can be analytically derived for objects with geometric shapes [102]. For complex objects like a protein, numerical methods are employed. In first approximation, the protein is considered to be a perfect conductor and the corresponding polarizability volume is calculated by computational tools like ZENO [103]. Scaling these perfect-conductor results to values of physiological protein afterwards was shown elsewhere [104].

Placed inside an electric field, a torque acts on molecules with a permanent or field-induced dipole moment. Depending on the field strength and magnitude of the respective dipole moments, the molecules align or orient along the field axis. “Alignment of molecules” here refers to confining an axis of the molecules to an axis in the laboratory frame, and “orientation of molecules” to have them in addition point into the same direction [105]. For example, a sufficiently strong homogeneous electric field causes molecules with a permanent dipole moment to orient along the field, i. e., all point along the field and into the same direction.

The interaction energy between dipole and field in relation to the energy $k_{\text{B}}T$ of the molecule describes the imposed confinement: for a hot and fast-rotating molecule, stronger fields are necessary to impose directionality onto it then for a cold, slowly-rotating one. Orientation in the field is expressed as the angle θ between the field and the dipole. The dipole-field interaction (Stark-) energy can be described as [106–110]:

$$W_{\text{p}} = -\mu_{\text{p}} \cdot E \langle \cos \theta \rangle \quad (2.8)$$

$$W_{\text{ind}} = -\mu_{\text{ind}} \cdot E \langle \cos^2 \theta \rangle = \frac{1}{2} \alpha E^2 \langle \cos^2 \theta \rangle, \quad (2.9)$$

where:

$W_{\text{p,ind}}$	interaction energy of permanent and induced dipole moments with the electric field in $\text{kg m}^2 \text{s}^{-2}$,
$\mu_{\text{p,ind}}$	permanent and induced dipole moments in C m, and
θ	the angle between the respective dipole moment vector and the electric-field direction in rad.

In combination, the permanent and the induced dipole moment make up the effective dipole moment of a molecule, which is the derivative of the combined interaction energies with respect to the field:

$$\mu_{\text{eff}} = -\frac{\partial(W_{\text{p}} + W_{\text{ind}})}{\partial E} = \mu_{\text{p}} \langle \cos \theta \rangle + \alpha E \langle \cos^2 \theta \rangle, \quad (2.10)$$

where:

μ_{eff}	effective dipole moment in C m.
--------------------	---------------------------------

Oriented in an inhomogeneous electric field with non-zero gradient ∇E , the partial charges of a dipole are exposed to asymmetric local field strengths. Instead of only a torque, additionally, a net force F acts on the dipole:

$$\vec{F} = \mu_{\text{eff}} \vec{\nabla} E, \quad (2.11)$$

where:

$\vec{\nabla} E$	electric-field gradient in V m^{-2} .
------------------	--

This force causes spatial deflection of dipoles along the field, as was first proposed by Kallmann and Reiche [111] and experimentally shown by Wrede [112]. Those molecules, which move into regions of weaker fields, are weak-field seekers. On the other hand, complex molecules and the ones in their ground state are strong-field seekers [113–116].

2.1.3. Optical Scattering

In the experiments described below, nanoparticles were imaged with an optical laser with intensity I_0 . A camera recorded the scattered photons and the resulting images were used to characterize the particles and their spatial distributions. The particles had diameters d , which were smaller than the wavelength λ of the laser, allowing applying Rayleigh scattering theory [117] to describe the observed intensity of scattered light I :

$$I \propto I_0 \cdot d^6 \tag{2.12}$$

where:

I scattered intensity in W m^{-2} ,
 I_0 incident intensity in W m^{-2} , and
 d diameter in m.

With this scaling law, the recorded intensities could be scaled to diameters, as was shown elsewhere for similar particle sizes [118].

2.2. Experimental Details

The physical basics introduced above help describe fundamental properties not only of ideal, mathematical abstractions, but also of large biological systems. But what is the scale considered here? How small is a “small” biomolecule, compared to a “large” one in the context of this work? Note that, while in physics, the unified atomic mass unit (u) is frequently used, for the description of protein masses, the Dalton (Da) is more commonly employed, with $1 \text{ Da} \equiv 1 \text{ u} \approx 1.660\,54 \cdot 10^{-27} \text{ kg}$. When describing protein masses, in this thesis, I will use the unit Da.

For example, few-atomic amino acids have lengths of $\leq 1 \text{ nm}$ and molecular masses of 100 Da, average proteins have diameters of few nm and masses of tens of kDa, like the 5 nm/64 kDa hemoglobin, and the 30 nm giant protein complex erythrocrucorin has a molecular weight of more than 3 MDa [119]. Following an experimental “top-down” approach, the sample described below spans sizes roughly from 300 nm (about the size of the largest viruses [120]) to 30 nm, pushing into the diameter range of typical proteins, which are of special interest in structural biology.

In this chapter, background on the aerosolization process and on aerosol characterization techniques is provided. Then, the electrostatic deflection setup is introduced.

2.2.1. Aerosolization Concepts

SPI aims at imaging structurally identical particles in the gas phase. With this requirement comes the need for appropriate aerosolization techniques to deliver intact nanoparticles into the x-ray focus of a free-electron laser (FEL).

Two established aerosolization methods were employed throughout this work and are here presented: gas-dynamic virtual nozzles (GDVN) and electrospray ionization (ESI). They differ in performance and scope. Both principles are depicted in Figure 2.2.

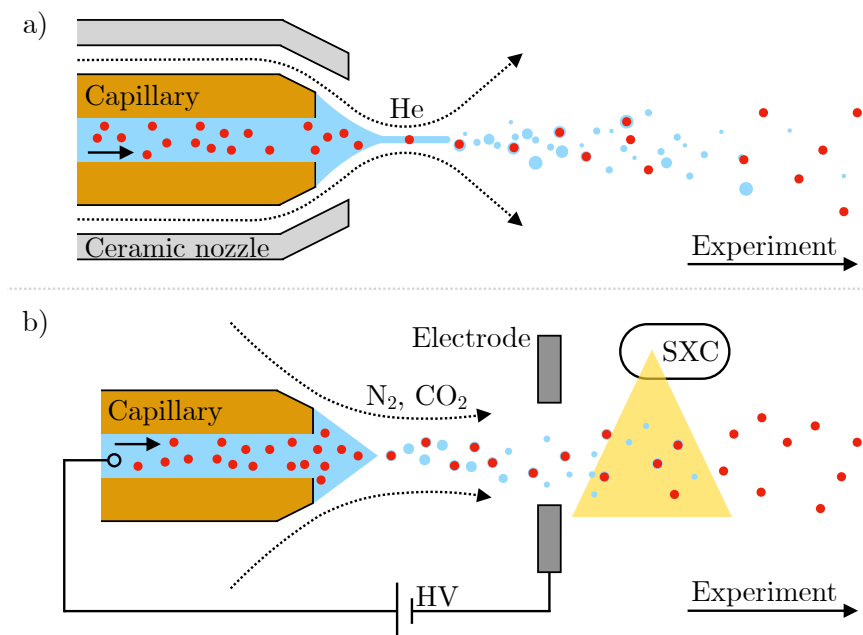


Figure 2.2.: Comparison between GDVN and ESI. a): The sample line, a borosilicate glass capillary with few tens of μm inner diameter, shown in dark orange, is fitted inside a nozzle, shown in grey. A sheath gas, e. g., helium, focuses the sample-containing water from the capillary into a thin jet, which becomes unstable and breaks into droplets of broadly dispersed sizes. These droplets contain sample molecules, shown as red dots, and within the sheath gas, they are transported toward the experimental chamber. b): For ESI, a similar glass sample line is used. Instead of pure water as in a), the aqueous suspension has a conductive additive, e. g., 20 mM acetate. Between the capillary tip and a ring electrode, depicted in dark grey, an electric field on the order of kV mm^{-1} is applied, penetrating the liquid meniscus, which forms the Taylor cone. From its tip, highly charged monodisperse droplets are ejected, carrying sample molecules. This process is stabilized by nitrogen and carbon-dioxide sheath gas, preventing electric discharge. Accelerated toward the electrode, the droplets, which pass through its orifice, are neutralized by a soft-x-ray bipolar charger, indicated by SXC and a schematic yellow triangular region of neutralization. The quickly evaporating droplets leave isolated, narrow- and low-charged particles in the gas phase, and within the sheath gas, they are transported toward the experimental chamber.

The first step toward transferring nanoparticles into the gas phase is preparation of sample

in aqueous solution. Afterwards, the particles are pneumatically pressed from their reservoir through a capillary. In a GDVN¹ [121, 122, 124], this capillary is fixed inside a second, larger nozzle. A sheath gas like helium tapers the sample-containing water from the inner capillary into a thin jet, which eventually becomes unstable and breaks up into droplets, containing the sample molecules. Carried by the sheath gas, the liquid evaporates and the aerosolized sample molecules are guided into the interaction region of the FEL.

GDVNs are proven tools for sample delivery in SPI experiments [125]. Even though smaller values were reported [126], the initially produced droplets normally have diameters of few μm [127, 128], making GDVN the method of choice for aerosolization of particles $\geq 70\text{ nm}$ [129, 130]. For much smaller particles, the probability of the droplets containing multiple particles at the same time increases, resulting in aggregation in the gas phase.

For transferring intact biomolecules from liquid into the gas phase, ESI is an established method. With it, sample in a mass range of 100 Da (like amino acids) to MDa protein complexes can be aerosolized [131–133]. Instead of pure water, which is often used for GDVN, sample is prepared in water with a non-denaturing, conductive, and ideally volatile additive, like 20 mM ammonium acetate solution [134].

For this technique, too, the sample-containing suspension is pushed through a capillary with an inner diameter of few tens of micrometers. In positive-ion mode, a negative voltage between the capillary tip and an electrode is applied and the corresponding electric field causes ion separation in the conductive liquid. This leads to formation of the so-called Taylor cone, which rapidly breaks up into highly charged droplets with monodisperse diameters of few hundreds of nanometers [135], ideally each containing a single sample molecule. In order to suppress discharging on the liquid/gas interface and to transport the generated droplets, a mixture of nitrogen (N_2) with 5–10% carbon dioxide (CO_2) is used as sheath gas. After being ejected, the droplets evaporate and leave micro-solvated molecules in the gas phase [86, 136–139]. Stabilized in this “nano-beaker” of few layers of water molecules, in general, preservation of solution-phase structure is assumed, which is essential for SPI of biological sample [87].

In comparison, GDVN and ESI differ in the generated droplet size [140] and the sheath gas they use. Starting from much larger volume than the ones from ESI, GDVN-sprayed droplets carry higher amounts of non-volatile impurities, which upon evaporation of the liquid will remain on the sample molecules, affecting their apparent structure in SPI experiments [141, 142]. An advantage of the GDVN is possibility to use helium, which has a low scattering cross section for the x-rays which are used in SPI experiments [143]. The conventional sheath gas mixture used in ESI, especially CO_2 , on the other hand creates significant x-ray-scattering background, which is one of the current bottlenecks toward SPI of small proteins [68, 140].

For the results presented in this work, both described aerosolization methods were used, in the form of a home-built GDVN and a commercial electrospray device (TSI model 3482

¹The first gas-focused microscopic jet device of this kind consisted of different components, not including a larger outer capillary but rather a flat surface with a hole [121]. Afterwards [122], this design was optimized for serial-diffraction experiments, resembling the device which was used throughout this work. The scope of an original GDVN was precisely defined and filed as a patent [123]. We may not have used a “GDVN” but a derivative of it; however, in the following, I will define our “gas-focused liquid jet technique” and refer to it as a “GDVN”.

with built-in neutralizer).

2.2.2. Neutralizer

A neutralizer was used in tandem with the electrospray. It shapes the charge-state distributions (CSD) shown below and is thus presented here in physical and technical detail.

Just after being ejected from the Taylor cone in an electrospray setup, the charged droplets start to evaporate. Left untreated, their surface shrinks, which results in an increase in surface charge density. When a droplet approaches the critical size at the Rayleigh limit, see Equation 2.4, it gets unstable, which results in an abrupt shedding of approximately 20% of the charges and 3% of the mass [135]. With ongoing evaporation, these fission events repeat until the analyte is quasi-dry with some stabilizing residue water molecules and left with the remaining surface charges, proportional to the surface of the proteins [144]. This picture follows the charged-residue model [145, 146].

Significant amounts of charges on the droplets cause structural changes of the molecules contained within due to Coulomb repulsion [147] and could be correlated to denatured proteins in the gas phase [148]. In contrast, SPI experiments aim for imaging biomolecules in physiological states. The aerosolization of particles and the evaporation of the droplets thus need to be as gentle as possible in order to retain the in-solution structure. One important step to producing intact aerosolized nanoparticles is reduction of charges. This can be achieved with soft-x-ray neutralizers.

After breakup of the Taylor cone, the charged droplets are accelerated downstream toward the electrode. It has an opening through which the aerosol enters the neutralization chamber as shown in Figure 2.2 b). Neutralizers are part of some commercial electrospray sources, such as the model that was employed for the described experiments. For this and similar models, soft-x-ray sources are used to generate bipolar gas ions with a number density on the order of 10^{14}m^{-3} , which are designed to promptly reduce the amount of charges of the aerosol droplets. Other pathways of neutralization include direct ionization or generation of charges from the surrounding chamber walls [149]. The charges of the evaporating droplets are neutralized and typically only few remain, depending on the size of the particles. Detailed descriptions and theory of the expected CSD after neutralization was described elsewhere [150–153].

For the used neutralizer model (TSI model 3088) and electrospray generator design, an approximation of the CSD for different particle sizes can be calculated². For 220 nm, 88 nm, and 30 nm particles, the expected CSDs are shown in Figure 2.3. With increase in size, the distribution broadens. For all sizes, a subtle asymmetry in the CSD is observed, with higher probability of negative charges in the aerosol.

2.2.3. Scanning Mobility Particle Sizer

In combination with charged particles, tools to externally characterize the electrospray-aerosolized species are electrostatic classifiers with differential mobility analyzers (DMA)

²The set of parameters, which describes the performance of the neutralizer, is shown in [150], Table B1. After careful consideration, parameter $a_4/N=0$ was assumed a typing error and changed for the shown calculations from 0.19770 to 0.10770, resulting in plausible distributions.

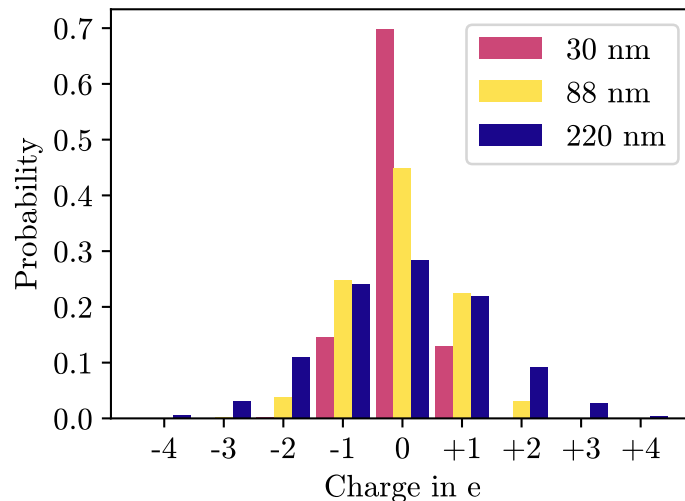


Figure 2.3.: Charge state distribution for selected particle diameters, based on charging theory and models by Wiedensohler and Fuchs, see text. For all sizes, the most probable charge is 0. With increase in particle diameter, the CSD broadens.

(TSI, classifier model 3080, DMA models 3081 “long” and 3085 “nano”) and condensation particle counters (CPC) (TSI, model 3786). The models used throughout this dissertation are in parenthesis. Used in tandem in this constellation, they are referred to as a scanning mobility particle sizer (SMPS) (TSI, model 3936).

A DMA samples electric mobilities of the particles within an aerosol, which was charged by a neutralizer. In positive-ion mode, only non-zero positively charged particles are transmitted, and vice versa for negative-ion mode. By scanning a deflection voltage and transmitting only species of a narrow electric mobility at a time, a broad size range from few nm to μm can be sampled with the classifier. For detection, the transmitted particles travel through atmosphere of saturated humidity in the CPC. Water molecules condense around the particle nuclei and eventually become big enough to be detected with a low-power optical detection setup. The number of counted particles at each time can now be correlated to the scanning voltage, and thus, with known internal parameters, to the particle mobility diameter [154].

This method allows quick characterization of the size distribution within the produced aerosol at a glance. When investigating particles with the experimental setup, presented in subsection 2.2.4, a SMPS serves as a benchmark and also provides limited insight into the charge-state distribution of the aerosol. Two exemplary SMPS plots of electrospray-aerosolized sample, measured with a “long” DMA in positive-ion mode, are shown in Figure 2.4. Here, a small bioparticle, bovine serum albumin (BSA) (Sigma Aldrich), and a large artificial nanoparticle, 220 nm polystyrene (PS) spheres (Alfa Aesar), were analyzed. The BSA plot shows a size distribution with a prominent peak at 8.3 nm, which can be expected to represent the BSA monomer [155–157]. On its right, additional peaks can be observed which quickly merge into a broad “shoulder”, trailing off to larger diameters. They indicate singly charged clusters of two or more particles, which have a reduced electric mobility, compared to the singly charged monomers. The relative peak heights change with the

prepared sample concentration: reducing the number density in solution results in a higher fraction of electrosprayed droplets containing single particles, but also in lower absolute numbers of aerosolized particles. Multiple peaks are also observed in the SMPS spectrum of 220 nm PS spheres. They appear toward smaller sizes in the distribution and correspond to higher order charges of individual spheres. Each peak successively indicates one additional charge, starting from +1 at 250 nm. For ejecting such large particles from the Taylor cone, the ESI parameters had to be tuned to atypically high flow rates, partially destabilizing the electrospraying process and causing larger initial droplets. The shift of measured particle diameters toward larger than the nominal values can be explained by excessive layers of liquid or non-volatile residues sticking to the particles. Droplet-size dependence on liquid

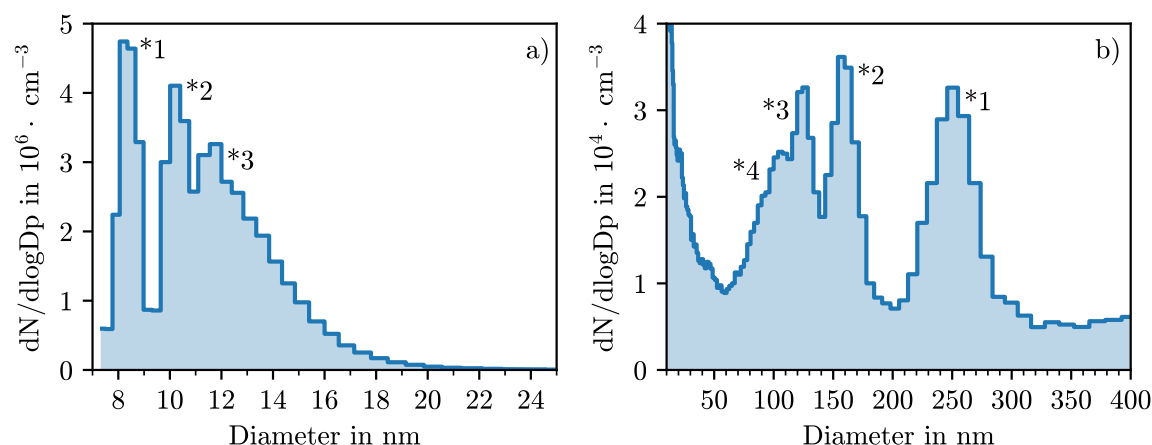


Figure 2.4.: Two SMPS measurements of electrosprayed particles. a): Aerosolized BSA. At 8.3 nm, a distinct peak of monomers (*1) could be observed, which was well-separated from dimers (*2) with two and trimers (*3) with three BSA molecules at 10.3 nm and 11.8 nm, respectively. Peaks of even larger clusters merge into a shoulder toward larger sizes ≤ 20 nm. b): Aerosolized 220 nm polystyrene spheres. Large particles like these have an increased chance of acquiring multiple charges, see Figure 2.3. Compared to singly charged aggregates as shown in a), the multiply charged single particles have a higher electrostatic mobility: *1 indicates singly charged, *2, *3, and *4 doubly, triply, and quadruply charged single spheres.

flow is shown in Figure 2.5. Here, water with 20 mM ammonium acetate and 2% sucrose (by volume) was aerosolized and characterized with an SMPS. While water and ammonium acetate evaporated, they left solid sucrose balls in the gas phase. By increase of the flow rate, the volumes of the produced droplets and the remaining sucrose particle sizes d_{suc} varied significantly, describing a change in initial droplet size d_{init} by a factor of ≥ 2 . This analysis helps to characterize the electrospray setup and the correlation between liquid flow and droplet size, which is especially useful for SPI of small biomolecules: for them, excessive evaporative impurity deposition should be avoided, as this cloaks the molecular structure.

As shown, an SMPS is a useful tool for initial characterization of sample concentration and presence of oligomeric species. Also, relative abundance of charge states of same sign can be evaluated, as was recently explored in detail elsewhere [158]. Furthermore, it can be

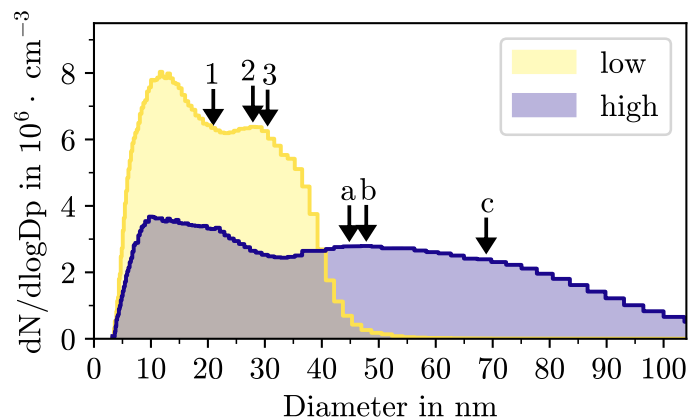


Figure 2.5.: Aerosol size distribution of electrosprayed 2% sucrose as measured with the “nano” DMA. Two different spraying conditions were used, which resulted in a low flow, shown in yellow, and a high flow, shown in blue. The median sizes (1 and a) were 21 nm and 44 nm, the most probable sizes of the larger-sized peak (2 and b) 28 nm and 48 nm, and the third quartile sizes (3 and c) 30 nm and 67 nm. The corresponding initial droplet sizes are calculated by correlation of initial diameter d_{init} , sucrose ball size d_{suc} , and sucrose volume concentration C_{suc} (in percent/100): $d_{\text{init}} = d_{\text{suc}} \cdot C_{\text{suc}}^{-\frac{1}{3}}$.

used to measure the initial size of droplets ejected from the Taylor cone.

2.2.4. Particle-Beam Characterization and the Electric Deflector

Above, methods to transfer nanoparticles from solution into the gas phase were presented, as well as means to characterize them. For SPI experiments, the aerosol is guided into the pulsed x-ray beam of an FEL in a narrow stream to achieve high particle number densities. This increases the probability of molecule exposure, respectively, the diffraction events per unit time, or in other words, the hit rate. These dense particle beams can be generated by hydrodynamic focusing of the particles in an aerodynamic lens stack (ALS), which uses stacked apertures to successively confine the aerosolized particles onto a central axis.

In order to reduce gas load in the interaction chamber, a differential pumping skimmer assembly is used before the ALS [159]. Upon exiting the ALS, the particles are injected into the experimental chamber as a focused or collimated beam and guided into the FEL [81, 125, 130, 160].

Performance of such an ALS injector in regard to velocities of the particles exiting it, and correspondingly, particle-beam widths and focusing behaviour, depends for example on shapes and masses of the particles, gas pressure parameters, and the used stack geometry [161]. Based on these criteria, ALS injectors can be optimized for experimental conditions [162, 163]. The geometry of an ALS describes the alternating diameters of the aforementioned apertures and drift tubes. For the experiments presented in chapter 3, a geometry as described elsewhere [163] was used. The geometry used in chapter 4 and chapter 5 was (in the same nomenclature as in the referenced publication): $R_0 = 10$ mm, $r_0 = 3.75$ mm, $R_1 = 10$ mm, $r_1 = 3.5$ mm, $R_2 = 10$ mm, $r_2 = 3.5$ mm, $R_3 = 5$ mm, $r_3 = 5$ mm, $R_4 = 5$ mm, $r_4 = 1.25$ mm.

For efficient SPI experiments, the particle beams should be characterized beforehand and experimental conditions optimized, since a narrow and dense beam at large distances from the injector surface promises high hit rates and low x-ray scattering background from metallic surfaces and gas. Having installed a setup in the laboratory, similar to the ones used at FELs, experimental conditions at beamtimes could be mimicked and particle beams characterized with optical imaging methods. This laboratory-based characterization setup is laid out in the following. The data collected in that setup yielded the results presented in the chapters below.

After ejection from an ALS injector, the particles were focused into an experimental chamber. Here, they were detected with a visible-light laser, which was pointed underneath the last orifice of the ALS to cross the particle beam. In a beamtime, this detection laser is replaced by the FEL x-ray beam. The ALS was mounted on a three-dimensionally (3D) motorized linear translation stage and by moving it along the injection axis, the particle beam could be illuminated at different heights. Scattering of photons from individual nanoparticles was recorded with an optical microscope setup (objective: Edmund Optics, model 59-876) in combination with a complementary metal-oxide-semiconductor active-pixel-sensor type (CMOS) camera (Teledyne Photometrics, model Prime 95B). The individual scattering events, called hits, were used for determining particle positions and scattering intensities.

We used two principal imaging configurations: a light-sheet- [164] and a side-view imaging setup, see Figure 2.6. In the former, the incident laser (Coherent, model Verdi V, average power: 5 W, $\lambda = 532$ nm) was focused along the y axis, yielding a light sheet. The camera was mounted underneath the laser and pointed upwards along y and into the particle beam. When particles passed through the continuous-wave (cw) illumination of the light sheet, the camera recorded scattering events.

In contrast, the laser for the side-view imaging setup (Innolas, model SpitLight 600, $\lambda = 532$ nm, pulse width: 10 ns, repetition rate: 20 Hz, nominal pulse energy: 239 mJ) was focused in two dimensions (2D) along the y and z axes. The camera was oriented perpendicular to both the intersecting laser and particle-beam axes and recorded the same observables as in light-sheet imaging, but along the z axis.

While data analysis was treated similarly, the main technical difference was the substantially higher peak intensity achieved with the pulsed compared to the cw laser, allowing for detection of smaller particles. In the side-view imaging setup, particles with diameters ≥ 27 nm could be identified.

In both setups, when the incident photons from the imaging laser scattered on a nanoparticle and into the camera, exceeding a detection threshold, hits could be detected. For the wavelength of $\lambda = 532$ nm, 1 photon was on average converted into 0.78 grey values at a quantum efficiency of approximately 95% [165].

With the particles being much smaller than the wavelength of the optical laser, structural details could not be resolved [17]. Instead, point spread functions of magnitude scaled to the sizes of the particles were recorded. As such, each particle hit corresponded to a 2D Gaussian distribution, a “blob”. A blob-finding routine based on Hessian curvature identification was implemented, as was shown for different applications with good resolution of even closely neighbored and partially overlapping blobs [166]. When two particles were detected too closely together, artifacts were produced in analyzing the recorded intensities, but these

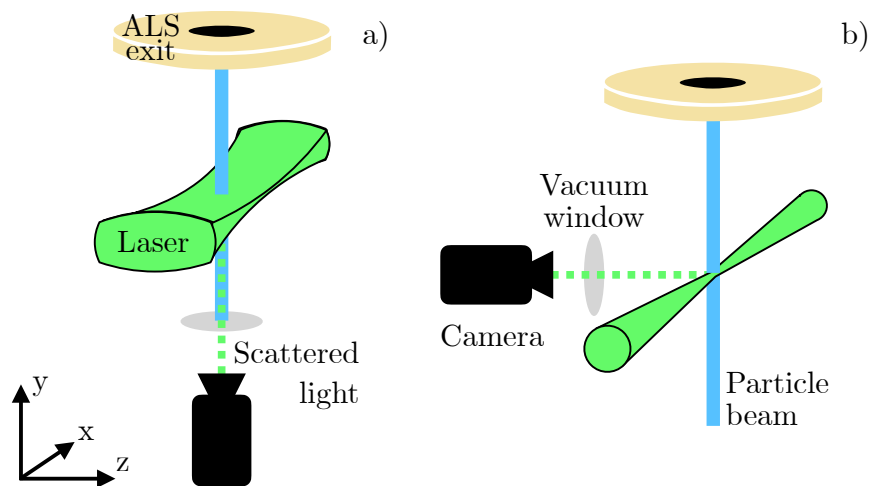


Figure 2.6.: The two particle-beam characterization setups. a): Side-view imaging. The optical laser entered the experimental chamber through a laser window along the x axis. It was focused with a cylindrical lens in y direction. The ALS was oriented along the y axis and injected the particle beam through the light sheet. The portions of scattering events in the xz plane were recorded by the camera. b): In side-view imaging mode, the camera was oriented along z . The pulsed laser, again propagating along x , was focused in 2D. The particle beam was illuminated and scattering along the z axis was recorded.

could be quantified and accounted for, see section B.1.

After having determined the spatial positions of detected particles, they could be converted into 2D histograms. Scattering intensities were integrated in a region-of-interest around the determined blob centers.

By taking the laser profile into account, the measured intensities could be normalized to the incident laser intensity, which allowed for comparison of scattering signal throughout the entire field-of-view of the camera, see section B.3.

One aspect of particle-beam characterization was studying their behavior in electric fields. These fields were created by electrodes and a voltage supply (Aim-TTi, model PLH250-P, maximum output 250 V). In the experiments presented below, two different arrangements as shown in Figure 2.7 were used. Both sets of electrodes were oriented along the z axis and at least two orders of magnitude longer than the expected particle-beam width. The electrostatic field generated between the electrodes could thus be considered constant along the z axis. The rod-electrode design, Figure 2.7 a), featured a large gap of 6 mm between the electrodes, which allowed transmission of broad particle beams and prevented back pressure of carrier gas. At the same time, the maximum electric field was weaker compared to the blade electrode design, Figure 2.7 b), in which the thin razor blade electrodes were positioned at a distance of 0.55 mm. This compact setup proved particularly beneficial for beams of small particles which focused at small distances from the ALS. The particles were injected into the electric field of either setup and their positions underneath the electrodes were recorded with a detection setup as described above.

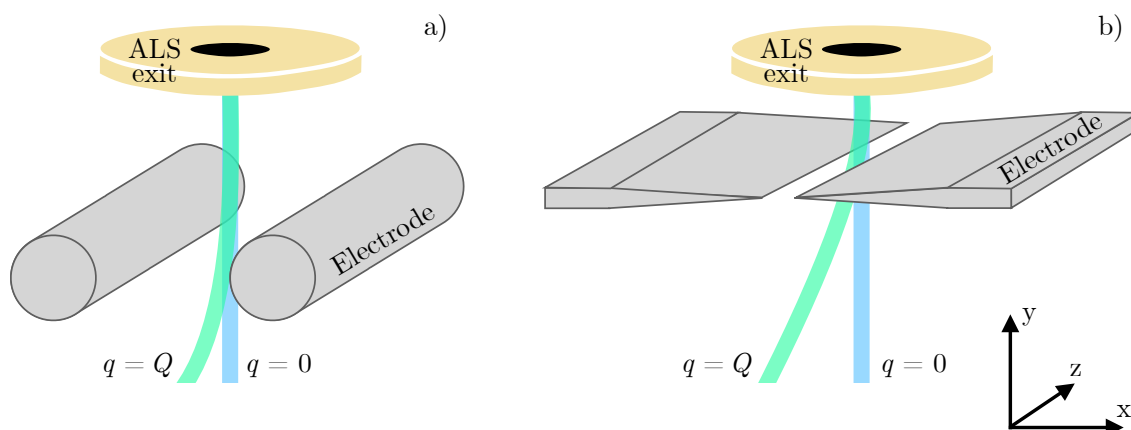


Figure 2.7.: Two electrode geometries were used for characterization of charge properties of nanoparticles, a): two rod electrodes with 4 mm diameter and a center point distance of 10 mm, mounted 14.7 mm underneath the ALS, and b): two blade electrodes, installed 1.1 mm underneath the injector. They were positioned at a distance of 0.55 mm from each other, allowing for stronger fields than the rod geometry. In both cases, charge-neutral particle beams ($q = 0$, blue line) were unaffected by the applied field, in contrast to charged particles ($q = Q$, green line).

2.3. Samples

After having given a summary of the used tools and techniques, this section will introduce the star of SPI: the sample. Of major scientific interest in structural biology are proteins [167], which have a form-/ function correlation: if we want to understand their function, we need to learn about their structure [168]. What are their structural features, and what happens when transferring proteins into the gas phase?

2.3.1. Proteins in Solution and in the Gas Phase

Proteins are one type of the four major biological molecules, among nucleic acids, lipids, and carbohydrates [169]. Dictated by their structure and the chemical properties of their exposed amino acids, proteins fulfill specific tasks in nature. They can for example mediate perfusion of molecules through cell membranes by forming transmembrane channels, initiate chemical reactions, convert energy, or help recognize pathogens [170]. Their structure is typically assessed on four hierarchical levels. The primary structure describes the amino-acid sequence of proteins. The secondary structure describes the repetitive, hydrogen-bonded folding pattern of amino acids, e. g., α -helices and β -strands. The tertiary structure is the 3D arrangement of the secondary-structure patterns, and some functional proteins consist of individual subunits, which together make up the quaternary structure [171].

Although many more variations of amino acids exist, proteins in humans consist of about 20 of them. With their average mass of 118.8 Da and a mean sequence length of 486 amino acids in animal proteins [172, 173], the average protein has a mass of approximately 58 kDa,

or $9.6 \cdot 10^{-23}$ kg. The individual amino acids consist of a backbone, which is an amino (NH_2) and a carboxylic acid group (COOH) attached to a central carbon atom, to which in most cases also a unique side chain is bonded, giving the amino acids individual chemical properties and structures [174]. These three groups can be ionized, depending on the pH of their environment and their dissociation properties. The amino acids, as well as the protein they make up, have a resulting net charge [175, 176]. This net charge can be zero, which is the case at a pH value corresponding to the isoelectric point (pI) of the protein [177], it is positive at $\text{pH} < \text{pI}$, and negative at $\text{pH} > \text{pI}$ [178]. If a side chain tends to bind a positive charge, it is basic. If it tends to lose protons, it is acidic. For proteins in solution, the net charge is the sum over all these charges and additional ions, which are in tight association with the protein [179].

What happens with proteins in the gas phase? When being aerosolized, for example *via* ESI in positive-ion mode, the droplets carry sample molecules in their center and protons on their surface, keeping the volume of the droplet essentially field-free [180, 181]. Upon evaporation, the protons tend to distribute among the most basic residues, and the resulting charge scales with their number, respectively, the surface of the molecules [87, 182, 183]. Highly charging a protein change its structure due to Coulomb stretching [184], and because the function of a protein is defined by their form, high charges should be avoided in structure-preserving ESI [185]. For SPI experiments, which are aiming at imaging the structure of protein and other biological sample in their “native state” in order to learn about their function, decharging of the molecules is achieved with a neutralizer as described above.

2.3.2. Artificial Nanoparticles

Instead of proteins and biosample, which can be difficult to produce, control, or acquire, an artificial model was used for some of the results presented in this work. Furthermore, the optical setup used for particle imaging had vanishing detection efficiency for particles ≤ 27 nm, which on the other hand is the size range for most protein samples. Instead, commercially available PS spheres with defined sizes as presented in Table 2.1 were used. Due to surface modification, coagulation for PS particles is largely avoided and isolated particles thus relatively easily produced.

Size in nm	Manufacturer	used in chapter
27.4 ± 6.0 ^b	TFS	5
42.9 ± 7.2 ^a	PE	5
52.0 ± 7.3 ^a	AA	4, 5
69.3 ± 10.2 ^a	PE	5
88.0 ± 7.0 ^a	AA	4, 5
220.0 ± 17.6 ^a	AA	3

Table 2.1.: PS sample which was used throughout this work. Sizes and distributions either correspond to manufacturer specifications^a or were measured with an SMPS device^b. Manufacturer acronyms: TFS (ThermoFisher Scientific, U.S.A.), PSI (Polysciences Europe GmbH, Germany), AA (Alfa Aesar, part of ThermoFisher Scientific).

2.4. Simulation Details

For simulating the deflection of charged particles in electrostatic fields, SIMION v8 [186], a commercial particle trajectory simulation platform, was used. The setup boundaries, like electrodes and other metal surfaces, were modeled in the respective interface and the resulting electric field from assumed applied voltages was calculated, see Figure 2.8. Sets of sample

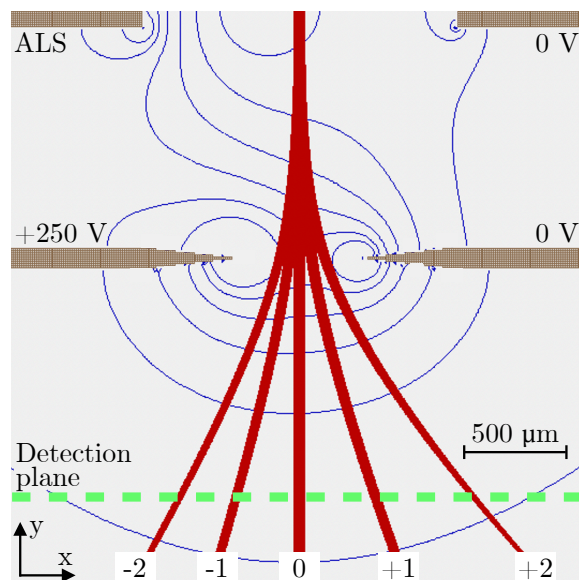


Figure 2.8.: Particle trajectory simulations, modeled with SIMION. The setup boundaries, i.e., electrode surfaces, were defined as geometric shapes (brown, hatched). Shown here is the blade deflector geometry as described above. +250 V were applied to one of the electrodes and the field between it, the second electrode, and the metal surface of the ALS was calculated. As guide to the eye, isolines of the electric field are plotted in blue. Particles with integer charges $[-2, +2]$ were initialized in the injector orifice (top of the figure) and propagated in $-y$ direction. Based on their charge, velocity, and mass, they deflected. At a defined y distance, the detection plane, their x positions were recorded and evaluated for further analysis.

species were defined in SIMION with mass-, spatial-, charge-, and velocity distributions, which were estimated either based on manufacturer specifications (their size), simulations, or experiments (their velocities and focusing behavior) [164, 187]. The particles were sequentially initialized and propagated in the calculated field. The resulting trajectories were evaluated numerically and could be used for analysis and calibration of experimental data, for example as is shown in chapter 3. Their positions at a detection distance from the modeled ALS outlet, corresponding to the distance of the detection laser in the experimental setup, were recorded. The simulated distribution of species in response to an electrostatic field was used as reference for the experimental observations, could confirm assignment of the observed peaks in the deflection profile, and give insight into the charge state distribution of an otherwise well-characterized sample.

Additionally, the potential array generated from electrodes was calculated with SIMION

and then exported. In Python [188], particle trajectories of neutral particles were calculated outside the SIMION framework, see chapter 6. Potentially, particle trajectories could be simulated in specialized frameworks like CMInject [187], but have not in the context of this work. However, indirectly, results from the referenced platform played a part in the successful execution of the presented experiments, as previous injector-geometry optimizations were performed with this code [189] and understanding the focusing behavior of nanoparticles improved with it.

3. Charge-State Distribution of Aerosolized Nanoparticles¹

After having established the fundamentals characterizing aerosolized particles for SPI experiments, in this chapter, the charge-state distribution of polystyrene nanoparticles is analyzed.

In single particle imaging experiments, beams of individual nanoparticles are exposed to intense pulses of x-rays from free-electron lasers to record diffraction patterns of single, isolated molecules. The reconstruction for structure determination relies on signal from many identical particles. Therefore, well-defined-sample delivery conditions are desired in order to achieve sample uniformity, including avoidance of charge polydispersity. We have observed charging of 220 nm polystyrene particles in an aerosol beam created by a gas-dynamic virtual nozzle focusing technique, without intentional charging of the nanoparticles. Here, we present a deflection method for detecting and characterizing the charge states of a beam of aerosolized nanoparticles. Our analysis of the observed charge-state distribution using optical light-sheet localization microscopy and quantitative particle trajectory simulations is consistent with previous descriptions of skewed charging probabilities of triboelectrically charged nanoparticles.

3.1. Introduction

Single particle imaging (SPI) experiments utilize x-ray diffractive imaging of individual nano-objects to determine their structure [67, 190, 191]. On a shot-by-shot basis, a stream of aerosolized sample molecules e. g., artificial nanoparticles [81] or biological macromolecules [83], is delivered into the focus of an FEL x-ray beam. The resulting diffraction patterns of the randomly oriented particles are collected and can subsequently be reconstructed into an average 3D volume with nanometer resolution [72]. Careful and controlled sample delivery are key to successful SPI experiments [192]: High-resolution structure reconstruction relies on a very large number of diffraction patterns of isolated, virtually identical particles [193].

Biological macromolecules, like proteins, are intrinsically flexible [194] and their structural integrity can be decreased by Coulomb repulsion between charges [195]. Therefore, excessive charging of injected biomolecules during SPI experiments must be avoided to maintain their native structure. Neutralizing soft-x-ray sources [149] and careful aerosolization schemes [196, 197] help reduce charges on aerosols created with electrospray-ionization generators. For another popular atomization method using gas-dynamic virtual nozzles

¹This chapter is based on the publication “Charge-State Distribution of Aerosolized Nanoparticles”, *J. Phys. Chem. C* **125**, 25794 (2021) by J. Lübke, N. Roth, L. Worbs, D. A. Horke, A. D. Estillore, A. K. Samanta, and J. Küpper. I contributed to designing the deflection setup, performed the experiments together with N. Roth, collected and analyzed the data, created the figures, and wrote the manuscript in discussion with all co-authors.

(GDVN) [124], the gas-focused liquid jets are assumed to not actively charge the sample and buffer solution [122].

Triboelectric charging of particles in the gas phase, i. e., after aerosolization, was characterized elsewhere [198]. Although the possibility of triboelectric charging of nanoparticles in GDVNs was pointed out by some of us before [199], for these setups no detailed understanding of the process nor the extent of charging on individual nanoparticles is available. Here, we demonstrate a direct method for detecting and characterizing the charge-state distribution of a beam of aerosolized nanoparticles.

3.2. Methods

In our experiment, prototypical polystyrene-sphere particles (Alfa Aesar, USA, $d = 220.0 \text{ nm} \pm 17.6 \text{ nm}$) were transferred from aqueous suspension with a concentration of $7.5 \cdot 10^6$ particles/ml into the gas phase using a GDVN which consisted of a borosilicate glass capillary (inner diameter $30 \text{ }\mu\text{m}$) fitted within a ceramic micro-injection-molded ejector tip [124]. Liquid-sample-line flow rate of approximately $1 \text{ }\mu\text{l}/\text{min}$ with helium as sheath gas yielded a hit rate of six to seven particles per camera frame at 20 Hz frame rate, which allowed single-particle counting; acquisition of one data set took 500 s .

In the gas phase, excess helium was pumped away in a nozzle-skimmer stage [162] and the particle beam was focused into the interaction region using an optimized [163] aerodynamic-lens stack (ALS)[159, 200]. We used an electrostatic deflector between the ALS exit and the detection position to disperse the initially cylindrically symmetric nanoparticle beam according to the particles' charges. The electric field was applied by two 70 mm long rod-shaped stainless-steel electrodes with a diameter of 4 mm and a center-point distance of 10 mm that were mounted $d_{\text{defl}} = 14.7 \text{ mm}$ below the ALS exit using PEEK holders, see Figure 3.1. The "+" electrode was connected to positive voltage of a power supply (Aim-TTi PLH250-P), whereas the "-" was connected to floating zero of the voltage supply. This created an inhomogeneous distorted two-wire field between the two electrodes and the grounded ALS. The steepest potential gradient between the rod electrodes was $333.3 \text{ V}/\text{cm}$.

Individual particles were counted in a size- and position-sensitive light-scattering microscopy setup [164, 201]. The visible-light sheet for detection of the particles passed through the experimental chamber perpendicular to the injected particle beam $d_{\text{det}} = 20 \text{ mm}$ below the last orifice of the ALS. We recorded the scattered light from intersecting particles using a microscope objective ($5\times$, apochromatic long-working-distance infinity-corrected objective, Edmund Optics 59-876) and a sensitive camera (Teledyne Photometrics Prime 95b). The positions of the individual nanoparticles were accumulated into a two-dimensional (2D) position histogram, yielding a cross section through the particle beam at a given distance from the injector.

3.3. Results and Discussion

Application of the light-sheet imaging method on the beam of polystyrene nanoparticles yielded the particle-beam cross sections shown in Figure 3.2. Without applying an electric

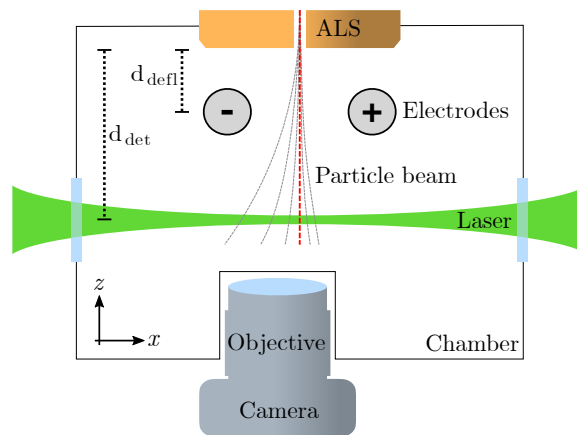


Figure 3.1.: **Experimental setup.** A focused beam (red dashed line) of nanoparticles aerosolized from a GDVN was produced using an aerodynamic lens stack (ALS). Details of the aerosolization and the differential pumping scheme were given previously [164]. In the extended setup presented here, the particles were deflected (grey dashed lines) by the inhomogeneous electric field between two rod-shaped electrodes (diameter: 4 mm, distance: 10 mm, length (out of plane): 70 mm) centered in a plane at $d_{\text{defl}} = 14.7$ mm below the ALS. The nanoparticles were detected at $d_{\text{det}} = 20$ mm below the ALS using a position-sensitive light-sheet microscope [164]. The figure is not to scale, see text for details.

field, a round particle-beam profile was observed with the highest density of particles in the center of the beam, Figure 3.2 a). When applying the electric field the beam profile became highly asymmetric along the horizontal field direction, see Figure 3.2 b). The majority of the particles were deflected to the left, i. e., away from the positive potential, directly implying a charge distribution of significant width and strongly skewed toward positive charges. These density profiles were integrated along the Y direction to yield the experimental beam profiles shown in Figure 3.3(blue lines).

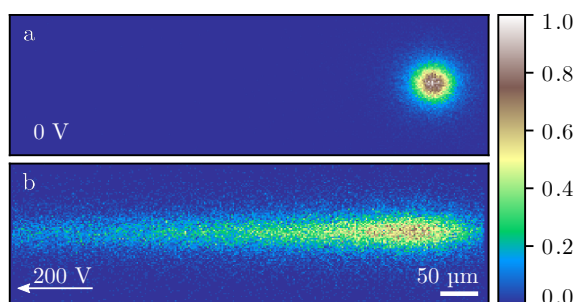


Figure 3.2.: **Particle-beam densities.** Particle-beam histograms at $d_{\text{detect}} = 20$ mm (a) without and (b) with an electric deflection field of 200 V applied. The white arrow indicates the electric-field direction. The colorbar is normalized to the highest counts in the 2D histograms.

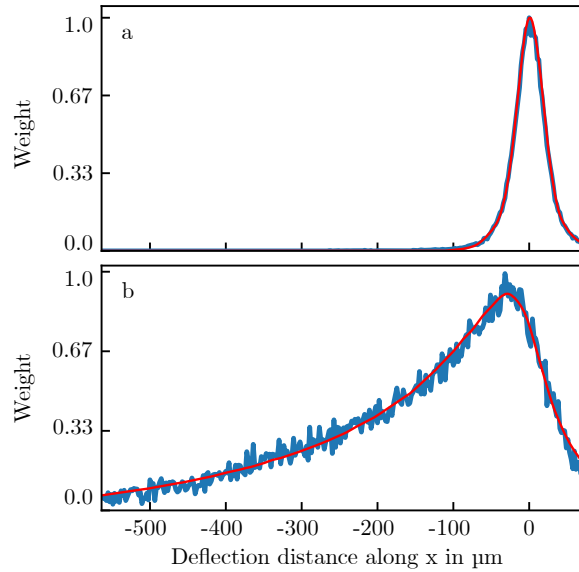


Figure 3.3.: **Measured and simulated particle-beam profiles.** One-dimensional particle-beam profiles for (a) 0 V and (b) 200 V, i. e., projections of the data in Figure 3.2 onto the field axis (blue lines). Corresponding simulated particle-beam profiles (red lines) with all profiles normalized to the maximum number of events.

In order to model the observed profiles, we modeled this setup in SIMION [186] in 2D, approximating the experimental geometry using two circles for the electrodes and a rectangle for the injector tip, with the potentials fixed at a given voltage on the “+” electrode and 0 V on the “-” electrode and the ALS. The 2D approximation of the experimental setup in SIMION was appropriate, even though the particle beam was cylindrically symmetric compared to translational symmetry of the electrostatic field: along Y , the field can be described as constant, because the rod electrodes are very long (70 mm) compared to the particle-beam dimensions (31.3 μm at $d_{\text{det}} = 20$ mm). So, for evaluating the particle deflection only the Z and X coordinates of the particles need to be considered. For a correct description of the electric far field the experimental chamber would also needed to be modeled as another ground electrode, but this would only result in extensive simulation times and can be safely ignored based on our extensive experience [106].

Using the resulting electric field, we simulated the trajectories of sets of 32000 particles using a size distribution corresponding to the manufacturer’s specifications ($d = (220 \pm 17.6)$ nm). Based on particle-beam-characterization methods we described elsewhere [164], we could assume an initial particle-beam full-width-at-half-maximum (FWHM) of 56.2 μm at the ALS outlet and a width of 29.5 μm in the focus 18 mm below the ALS as well as nanoparticle speeds of $v = (130 \pm 15)$ m/s.

Elementary charges in the range $[-500, 500]$ were assigned to each set of particles and the respective 1001 individual-charge nanoparticle-density profiles were simulated. The simulated particle positions were sampled at $d_{\text{det}} = 20$ mm and collected into a histogram along X , yielding simulated line profile of the particle beams. We used a bin width of

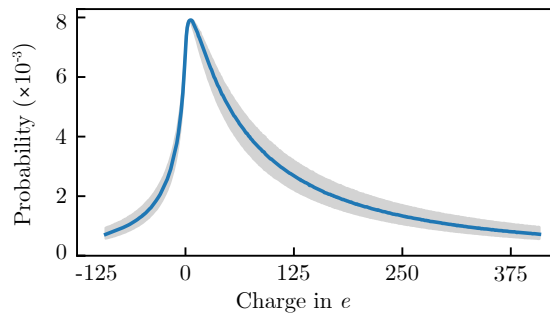


Figure 3.4.: **Charge-state distribution.** Histogram of the fitted charge-state distribution in the nanoparticle beam, normalized to the sum of observed charges in the shown interval. The 1σ standard deviation in the probability is shown by the light gray area; see text for details.

1.85 μm , corresponding to the camera pixel edge length in the experimental microscopy setup.

We combined these individual-charge profiles into an overall nanoparticle-density profile as a weighted average to extract the charge-probability distribution of the nanoparticles. The weights, i. e., the contributions of the charge states to the sample, were determined from a fit to the experimental data. We used `scipy.optimize.differential_evolution` [202] with a maximum number of generations of 1000, a population size of 15, and a relative tolerance of convergence of 0.01 to minimize the mean squared error between the simulated and the measured profiles.

Models for describing the corresponding charge-state distribution included uniform, normal, and heavy-tailed – i. e., lognormal, loglogistic, scaled inverse Chi-squared, F, and normal-lognormal (NLN) [203] – distributions. NLN-distributed charge states were described elsewhere for triboelectrically charged microparticles [204]. In our case simulated particle-deflection beam profiles with NLN-distributed charges yielded highest agreement with experimental profiles. An NLN distribution can be described by the product of two sets of random variables, one being normally, the other lognormally distributed, which are referred to by three independent parameters. We fitted these parameters for the retrieval of an NLN distribution function that reproduced the experimental charge-state distribution very well.

We fitted the charge distribution of the particles in the beam to minimize the χ^2 deviation of experimental and simulated profiles of the particle beam along X . Optimization yielded the simulated profiles in Figure 3.3 (red lines). We performed the corresponding χ^2 goodness-of-fit test [205] with a pre-determined level of significance $\alpha = 0.05$. Based on the number of counted particles $n \approx 60000$, we chose $M = 160 \approx 2 \cdot n^{2/5}$ degrees of freedom [205, 206]. We calculated p -values of $p > 0.99$. As $p > \alpha$ there is no significant difference between the measured data and simulations with the NLN-distributed charge states. Thus the underlying charge-state distribution of the measured particles can be adequately described by the obtained NLN distribution. The resulting nanoparticle-charge distribution is shown in Figure 3.4. The most likely charge observed in our experiment is +5. The distribution shows a steep decrease toward smaller, i. e., negative, and a long tail of positive charges up

to $>375 e$ on the 220 nm polystyrene latex spheres, corresponding to surface charge densities of up to $+39.5 \text{ nC cm}^{-2}$, which is reasonable (i. e., smaller) compared to published literature values [207] for positively charged polystyrene nanoparticles.

Positioning uncertainties of the experimental setup and possible deviation of the velocities of the particles were propagated through the simulations. Here, we assumed uncertainties for the positioning of the particle beam and the detection light-sheet in respect to the electrodes of $\pm 500 \text{ }\mu\text{m}$. Furthermore, the mean initial particle-beam velocities were in the range $[120, 140] \text{ m/s}$ to incorporate the velocity spread of the particles. These effects result in the uncertainties of the charge probability distribution in Figure 3.4

These charges might originate from triboelectric charging in the GDVN [199], from collisions between nanoparticles, or in the aerosol transport tubes due to collisions with the surrounding walls. Even though classical triboelectric charging models would suggest mainly negative charging of polystyrene on metal surfaces, deviations from the triboelectric series have been observed [208–211]. Another source for particle charging might be the aerosolization process: During gas focusing of the liquid jet the collision rates between gas molecules and sample droplets are high and charge transfer during this process can not be excluded. It is beyond the scope of the current work to fully determine these physical principles. Instead, we provide a working tool for future studies when exploring these details of particle charging, possibly through systematic experiments on the effects of sample material, varying the jetting conditions of the GDVN, or using different aerosolization mechanisms, e. g., electrospray ionization or atomizers. The current results demonstrate the possibility for controlling and separating charged particles in SPI-type experiments and to investigate the effect of defined charges on overall sample structure and integrity.

3.4. Conclusion

In conclusion, we demonstrated a method to characterize the charge-state distribution of a stream of aerosolized nanoparticles. An ALS injector was used to form a nanoparticle beam. When the beam was exposed to an electric field, we observed large deflection of the nanoparticles, indicating large charges.

We used charged-particle trajectory simulations to quantitatively describe our experimental setup. Iteratively fitting the simulated deflection profile with the experimental one, we extracted the underlying charge-probability distribution, which revealed significant positive charges ($>375 e$). Finding charges on GDVN-aerosolized particles is not necessarily intuitive. For example, during SPI experiments these particles are presumed to be overall neutral in charge [122]. Excessive charging can be a source of structural variance of individual particles, and thus effectively a bottleneck for overall resolution in structure retrieval. If deemed necessary, neutralizing soft-x-ray devices may be employed to reduce the overall charges on the aerosolized nanoparticles.

For future SPI experiments it would be highly beneficial to control or select the charge states of the aerosolized particles, e. g., using the electrostatic deflection technique we presented here, similar to control over small molecules [106].

4. Characterization and Control of the Charge-State Distribution of Neutralized Nanoparticles¹

After having observed charges on gas-phase particles from a non-ionizing aerosolization device, in this chapter, the discrete charge-state distributions (CSD) of nanoparticles are shown, which were first electrospray-ionized and then neutralized. Purification of beams of artificial nanoparticles into distinct charge states and control of their CSD by variation of the initial droplet size is described. These findings allow for a high degree of species control for single-particle imaging (SPI) experiments, where strictly identical particles need to be delivered into the x-ray of free-electron lasers for structural imaging.

4.1. Introduction

SPI is a molecule imaging technique, with which x-ray diffraction snapshots of nanoscopic gas-phase objects, like biological macromolecules, are acquired. In order to minimize structural ambiguity and improve SPI resolution, the investigated particles should be virtually identical, which means, that the sample needs to consist of pure oligomeric, charge, and conformational species. With the goal of improving SPI experiments, sample delivery is optimized offline by thorough sample pre-characterization in laboratory-based experimental setups. As shown in chapter 3, one property of aerosolized nanoparticles is their CSD. There, artificial nanoparticles were aerosolized with a non-ionizing liquid-jet technique (GDVN) and quantitatively analyzed. Deflection experiments revealed significant and broadly dispersed charging, which, being produced from a GDVN, may be unexpected. On softer biological sample, charges can lead to unspecified structural bending and deformation due to intramolecular Coulomb repulsion [213]. Thus, reduction of charges should be pursued for SPI experiments, promising higher uniformity of biological sample like protein.

For this chapter, instead of using a GDVN, electrospray ionization [214] (ESI) was adapted as an established aerosolization method from structure-biological science. Regularly applied in mass spectrometry, with it, intact macromolecules can be transferred into the gas phase [215]. A benefit of this technique is generation of relatively small and monodisperse droplets, because evaporative deposition of non-volatile residues onto the sample in the process of aerosolization scales with the initial droplet size and should be kept to a minimum for SPI [140]. Since excess charging, potentially unfolding the biological analyte, occurs also in ESI [148], a soft-x-ray neutralizer [149] is employed for SPI experiments. These neutralizers reduce the charges on the ESI-generated aerosol by direct ionization and collisions in a

¹This chapter is foreseen for publication. It is based on joint work with J. L. Carneiro in the context of her Bachelor's thesis [212], which I supervised. I designed the experiment, performed the experiment, analyzed the data, and created the figures shown in this chapter. J. L. Carneiro helped with sample preparation and data collection.

bipolar gas-ion environment, yielding narrow CSDs, which are centered around zero. The widths of these distributions depend especially on the particle size [151–153].

In this chapter, it is shown that the center of the CSD, i. e., the observed median charge, is not necessarily at zero, but instead dependent on aerosolization parameters. Aerosolized polystyrene spheres were spatially purified by dispersing them into beams of defined charge states. Afterwards, an approach is presented for CSD control on gas-phase particles by means of liquid-flow rate variation. While correlation between flow rate, charge states, and possible denaturing of biological sample was observed in mass-spectrometry ESI [216], here, a fundamentally different charging mechanism was imposed on the particles by the neutralizer employed in the shown experiment.

4.2. Methods

As a first step toward charge-controlled delivery of proteins in SPI experiments, polystyrene (PS) spheres were selected as model sample (Alfa Aesar, nominal diameter: 88 nm, coefficient of variance: 8%, concentration: 2.6 wt.% solids). A suspension was prepared with a number concentration of $C_{\text{sample}} = 2.7 \cdot 10^{11} \text{ ml}^{-1}$, to which 10 mM ammonium acetate was added as a conductive agent for ESI. In the electrospray (TSI, model 3482 with soft-x-ray neutralizer), from its reservoir, the suspension was pushed pneumatically through a 35 cm long borosilicate glass capillary with an inner diameter of 40 μm . By application of a pressure p_{sample} , the sample-flow rate was controlled. With the ESI parameters shown in Table 4.1, p_{sample} was set to 2.0 bar, 1.5 bar, 1.25 bar, and 1.0 bar, with 1 bar = $1 \cdot 10^5$ Pa. Another data set at 1.0 bar was recorded, but with increased sheath gas flow, and thus, reduced differential pressure. We could thus assume a lower flow rate than for the “1.0 bar” setting. Beyond the highest set pressure, i. e., liquid flow at 2.0 bar, the Taylor cone of the electrospray destabilized.

After transfer into the gas phase, excess carrier gas, a mixture of CO_2 and N_2 , was removed in a differential pumping stage and the aerosolized nanoparticles were focused into particle beams with an aerodynamic-lens stack (ALS) [163]. Injected into an experimental chamber along y , they passed through an electrostatic field (voltage supply Aim-TTi, model PLH250-P, maximum output: 250 V), produced by two blade electrodes with a gap width of $\Delta x_{\text{gap}} = 0.55 \text{ mm}$ as shown in Figure 4.1. 250 V were applied to one of the electrodes, resulting in a maximum field strength of 4.5 kV cm^{-1} between the blades. The electrodes were mounted $\Delta y_{\text{ALS,elec}} = 1.1 \text{ mm}$ downstream from the injector exit. Another $\Delta y_{\text{elec,det}} = 2.1 \text{ mm}$ downstream, 3.2 mm underneath the outlet of the ALS injector, a laser (Innolas SpitLight 600, $\lambda = 532 \text{ nm}$, pulse width: 10 ns, repetition rate: 20 Hz, nominal pulse energy: 239 mJ) intersected the particle beam along x . A camera-microscopy setup, oriented along z , recorded scattering events when particles were illuminated by the laser. The two-dimensional (2D) positions of the particles in the xy plane along with the scattering intensities were retrieved.

4.3. Results and Discussion

After aerosolization and aerodynamic focusing of 88 nm PS spheres, they were detected in a side-view camera-microscopy imaging setup as described in subsection 2.2.4. Without

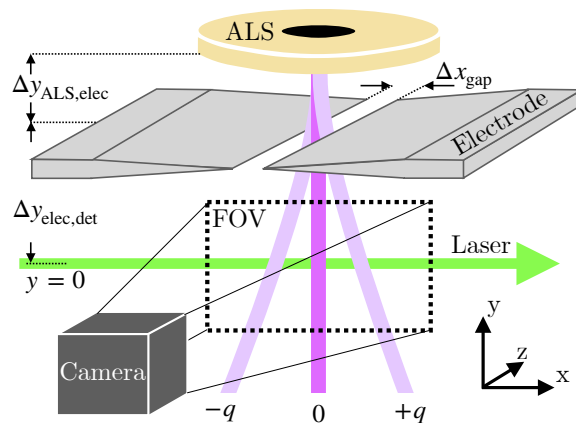


Figure 4.1.: Sketch of the used deflection-and-detection setup. A particle beam (purple) was focused into the experimental chamber from an aerodynamic-lens-stack injector (ALS). At a distance of $\Delta y_{\text{ALS,elec}} = 1.1$ mm below the last injector orifice, it passed through an electric field between two electrodes, which were positioned with a gap of $\Delta x_{\text{gap}} = 0.55$ mm. Dispersed beams of charged (light purple) and net-neutral (dark purple) particles could be detected with an optical-microscopy camera setup, which recorded scattering along z of particles, which were illuminated by a laser at a distance from the ALS of $\Delta y_{\text{ALS,elec}} + \Delta y_{\text{elec,det}} = 3.2$ mm.

application of an electrostatic field, a beam of particles with a full width at half maximum of $60 \mu\text{m}$ could be observed 3.2 mm underneath the ALS. A 2D histogram of the positions of the particles in the xy plane is shown in Figure 4.2 a). Exposed to an electric field, see Figure 4.2 b), the beam split up into distinct accumulations, spatially separated from the position of the undeflected beam and each other. Corresponding to the sign of the applied voltage, positively charged particles deflected to the right, and negatively charged ones to the left. The undeflected particles could be assumed to be neutral. With distribution minima dividing them, the distribution maxima could be assigned integer charges, increasing in absolute value with their distance from $x = 0$. Within the spatial bins, which are indicated by grey dashed lines in Figure 4.2 b), the number of detected particles translated into a CSD, see Figure 4.2 c). A slightly left-skewed distribution, with a most probable charge of +1, was observed.

With this method of CSD quantification, the effect of ESI sample-flow rate variation on the charges of the detected particles was investigated. Different pressures p_{sample} were applied, which led to different ESI-flow rates, and the corresponding CSDs were determined. They are shown in Figure 4.3. For all flow rate settings, the respective base line of zero probability is shown as a dotted line. The median charge (second quartile, Q2) is depicted as a solid black line, along with a range (light gray) between the first (Q1) and third quartile (Q3).

The lowest flow setting “<1.0 bar” produced a CSD with a median charge of $1.14e$ and an interquartile range ($\text{IQR} = \text{Q3} - \text{Q1}$) of $1.49e$. When successively increasing p_{sample} , and with it, the sample-flow rate, the distribution shifted toward lower charges. For the highest pressure-/liquid-flow setting “2.0 bar”, the CSD was in close agreement with the values that can be

	Parameter	Value
	C_{sample}	$2.7 \cdot 10^{11} \text{ ml}^{-1}$
	$C_{\text{amm.ac.}}$	10 mM
ESI	U in V	1870
	I in nA	395
	\dot{V}_{N_2} in l/min	1.82*
	\dot{V}_{CO_2} in l/min	0.135
	p_{injector} in mbar	0.2
	p_{sample}	<i>scanning</i>
Distance in mm	Δx_{gap}	0.55
	$\Delta y_{\text{ALS,elec}}$	1.1
	$\Delta y_{\text{elec,det}}$	2.1

Table 4.1.: Average values of experimental parameters as described in the text. The concentrations refer to the amount of nanoparticles in solution (“sample”) and additive molarity (“amm.ac.”). The ESI rows correspond to the electrospray operation parameters, i. e., the voltage, current, nitrogen flow, and carbon-dioxide flow. The pressures p refer to the pressure above the ALS, which determines the particle-beam formation, and the pressure onto the sample, causing the liquid sample flow. p_{sample} was set to 2.0 bar, 1.5 bar, 1.25 bar, 1.0 bar, and <1.0 bar. *For setting “<1.0”, a nitrogen flow of 2.31 min^{-1} was set. The distances in the last row correspond to the ones in the setup Figure 4.1.

expected for neutralized 88 nm particles. Based on the charging theory of Wiedensohler et al. [150–153], see also subsection 2.2.2, the expected CSD of particles with this size has the metrics $Q_1 = -0.58 e$, $Q_2 = -0.03 e$, and $Q_3 = 0.47 e$, compared to the here determined values $Q_{1,2,0} = -0.52 e$, $Q_{2,2,0} = -0.03 e$, and $Q_{3,2,0} = 0.40 e$.

In regard to producing predominantly charge-neutral aerosolized particles, which have minimal structural heterogeneity due to Coulomb stretching, using high liquid flow seems beneficial. This can be attributed to neutralizer efficiency: much larger initial droplets from the electrospray, a result from high flow rates like in setting “2.0 bar”, have a higher effective cross section and, as proposed in Appendix section A.1, spend longer times in the neutralizer device. Thus, they are neutralized more efficiently.

In general, fewer charges were observed, compared to previous results on GDVN-aerosolized nanoparticles [217]. There, a similar experimental setup was used, but significantly higher charges were detected, allowing the conclusion that no charging occurs after the aerosolization process, respectively, in this case, after charge reduction from the neutralizer.

The correlation between flow rate and CSD was inferred for 88 nm polystyrene particles. Extrapolating from the 88 nm polystyrene spheres, smaller sample also has positive-charge-centered but more narrowly distributed CSDs, which can be shifted toward neutral values the same way – by increasing the liquid-flow rate. However, generating large droplets around small molecules with high liquid flow will lead to significant deposition of non-volatile residue onto the analyte, itself introducing structural heterogeneity and cloaking molecular structure.

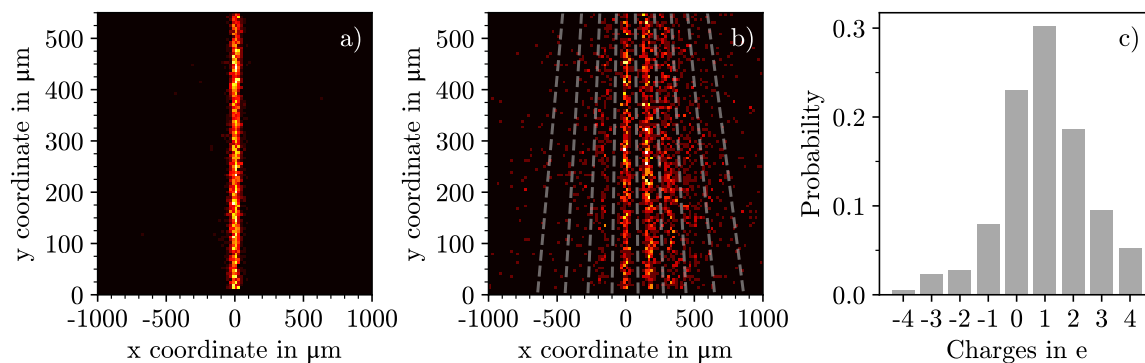


Figure 4.2.: a): The 2D spatial distribution histogram of 88 nm polystyrene particle beams at $p_{\text{sample}} = 1.0$ bar, no electric field applied. The particles propagated from the top to the bottom along y . The detection laser was positioned along x at $y = 250 \mu\text{m}$. b): After exposure to an electric field, separated beams could be observed. The particles detected at the same x position as in a) were considered charge-neutral. With the positive electrode on the left, the particles toward positive x axis values had positive charge. The gray dashed lines indicate distribution minima, separating beams of pure integer charges. c): Counting the events within the individual bins indicated in b) resulted in a CSD as shown here. The most probable charge was +1.

In general, aerosolization conditions, which lead to low charging combined with minimal residue adducting, should be chosen.

4.4. Conclusions

88 nm PS spheres were aerosolized with an electrospray device, which had a built-in neutralizer. The produced gas-phase particles deflected in an electrostatic field and well-resolved beams of pure charge were observed.

The CSD was retrieved from the recorded optical images. It could be shown how the CSD as a result of the system transfer function from the electrospraying and neutralization process can be modulated by changing the sample-flow rate. The liquid flow was controlled indirectly by changing the sample pressure, i. e., the differential pressure between the sample and the electrospray capillary tip. With increasing liquid flow, a narrowing of the CSD was observed, as well as a shift of the median charge toward net-neutral. This is the inverse trend observed for ESI without using a neutralizer [216]. For the highest used liquid flows, the largest fraction of neutral particles could be observed. This can be ascribed to higher neutralizer efficiency for droplets with large cross sections.

In future experiments, correlation of applied flow rate and observed CSD should be investigated systematically to determine aerosolization conditions, which lead to low charging combined with minimal residue adducting. As an additional parameter, the combined effect of flow-rate variation and different solution additives on CSDs should be investigated: charge reduction in non-neutralized electrospray due to presence of additives was shown elsewhere [185]. In order to maximize the amount of charge-neutral particles, also, different

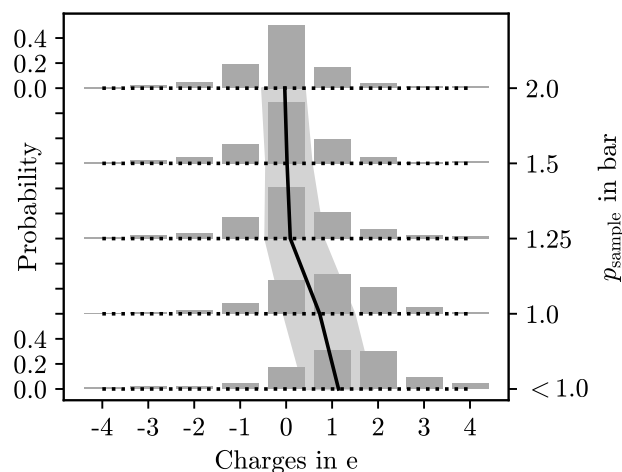


Figure 4.3.: Correlation between charge-state distribution and sample-flow rate. Shown are observed CSDs for the applied sample pressures, corresponding to liquid-flow rates (right y axis). The CSDs are shown as dark gray bar plots. For all settings, as a guide to the eye, the interpolated median charge (Q2) is shown (black solid line) along with a range between the first (Q1) and third quartile (Q3) as a measure of spread. The distribution shifts with the flow rate from positive charges to net-neutral: while the low-flow setting exhibits an interpolated median charge of 1.14 e, for the high-flow setting it is reduced to -0.03 e. The interquartile range $IQR=Q3-Q1$ narrows from 1.49 e to 0.92 e.

neutralizer arrangements should be tested, for example, by adding a second device or extending the neutralization chamber, which should increase neutralization performance even for smaller particles. This could potentially increase sample purity and especially the amount of neutral aerosolized nanoparticles, which is highly beneficial for SPI experiments, where high molecular charging should be avoided due to possible Coulomb-induced repulsive stretching.

5. Size and Charge-State Purified Dense Beams of Macromolecules for Single-Particle Imaging Experiments¹

After having investigated, characterized, and even controlled charge-state distributions on electrospray-ionized artificial nanoparticles, in this chapter, a biological macromolecule is chosen as sample. The results from above were applied and beams consisting of monomeric protein complexes could be observed. In-depth analysis of scattering signal was used for identification of regions with high oligomeric purity within the particle beam. In single-particle imaging (SPI) experiments, beams of aerosolized biological nanoparticles are guided into free-electron lasers for diffractive imaging on isolated molecules in the gas phase. These particles typically have a charge-state distribution, which may affect their structure due to intramolecular Coulomb repulsion. In order to characterize the charge states and produce particle beams of pure charges, we employed an electrostatic deflection setup and recorded optical scattering from isolated biological macromolecules. We demonstrate the separation of different charge states of erythrocrucorin protein complexes in a beam, ideal for single-particle imaging experiments.

5.1. Introduction

In SPI experiments at x-ray free-electron lasers (FELs), individual nanoparticles are imaged successively in a diffraction-before-destruction approach [67, 190, 191]. The sample is aerosolized, for example, using electrospray ionization and the aerosol then guided into the focus of the FEL for diffractive imaging of individual sample molecules [81, 83]. The serially recorded snapshots of particles are grouped according to their arbitrary spatial orientation. The diffraction patterns of identically-oriented particles are averaged, increasing the inherently low signal-to-noise ratio, and then combined for calculating the three-dimensional structure of the sample molecules [72].

Ideally, the sample molecules in SPI experiments are perfect structural clones of each other. But this is not the case in real-life sample: heterogeneity due to conformation, thermal effects, or varying amounts of residue water layers on the molecules should be expected [86, 218]. While for sufficiently strong-scattering or scattering-enhanced molecules, advanced data processing methods allow for disentangling morphological differences [83, 193], structural variability of weak scatterers like small protein adds noise in the diffraction patterns, ultimately limiting achievable resolution [219].

¹This chapter is foreseen for publication as “Size and Charge-State Purified Dense Beams of Macromolecules for Single-Particle Imaging Experiments.” Planned submission to *J. Phys. Chem. Lett.* (2022) by J. Lübke, L. P. Xavier, L. Worbs, A. K. Samanta, H. N. Chapman, and J. Küpper. I contributed to designing the deflection setup, collected the data, analyzed it, created the figures, and drafted the manuscript in discussion with the co-authors.

Another source of interparticle structural differences is induced by the process of aerosolization. As we showed recently, significant charging of nanoparticles occurs in gas-focused liquid-jet aerosolization [217]: hundreds of elementary charges were observed on 220 nm polystyrene spheres in the gas phase.

Electrospray-ionization sources can be operated to produce charge-reduced, monodisperse droplets, each containing ideally one target molecule [140, 220, 221]. These droplets carry a net charge, typically on the order of a few to tens of elementary charges [196, 197]. When the carrier liquid evaporates, the charges remain on the molecule within. Employment of a soft-x-ray neutralizer reduces the absolute initial charge to a few charges distributed around zero [149]. Still, the experimental particle beam is heterogeneous: it consists of single molecules and clusters of two or more particles, and each will statistically be negatively or positively charged or net neutral. High charging distorts or even fragments aerosolized molecules [147, 222–224]. For imaging methods aiming at atomic resolution such as SPI, any structural ambiguity should be avoided and the particle beam purified accordingly.

Here, we propose and demonstrate a method for generating charge-purified high-density nanoparticle beams using electrostatic deflection. We report results on the 3.6 MDa macromolecule erythrocrucorin [225]. We also demonstrate an imaging method based on optical scattering and describe our analysis of the recorded images for quantitative characterization of the spatially separated species. The produced particle beams of high charge-state purity make an ideal target for SPI experiments and are highly amenable to further control, e. g., electrostatic focusing [226, 227], bunching [228], or even acoustic manipulation [229] to improve experimental efficiency.

5.2. Methods

Isolated nanoparticles were created by aerosolizing aqueous suspensions, using an electrospray source with integrated neutralizer (TSI, model 3482) with a liquid-flow rate of 150–250 nl/min. Erythrocrucorin sample was produced following a purification protocol [230], yielding an approximate number concentration of $2 \cdot 10^{13} \text{ ml}^{-1}$. Scattering reference sample consisted of spherical polystyrene (PS) particles with sizes $27.4 \pm 6.0 \text{ nm}$ (Thermo Fisher Scientific), $42.9 \pm 7.2 \text{ nm}$ (Polysciences Inc.), $52 \pm 7.3 \text{ nm}$ (Alfa Aesar), $69.3 \pm 10.2 \text{ nm}$ (Polysciences Inc.), and $88 \pm 7.0 \text{ nm}$ (Alfa Aesar) with a concentration of approximately $1 \cdot 10^{10} \text{ ml}^{-1}$ for each preparation.

The nanoparticle-size distribution in the generated aerosol was monitored offline with a differential-mobility analyzer (DMA) (TSI, model 3786) and a condensation particle counter (CPC) (TSI, model 3081) and is shown for aerosolized erythrocrucorin in Figure 5.1. The distribution peaks of erythrocrucorin at mobility diameters of 28.8 nm, 35.9 nm, and 43.0 nm corresponded to monomers, dimers, and trimers, accordingly. Throughout the rest of this chapter, aggregates larger than dimers are referred to as “large clusters”. When increasing the sample concentration, the observed particle sizes shift to larger values. This is a result from the simultaneously-increased amount of non-volatile residues in the generated droplets, which deposit on the analyte molecules upon evaporation. The same effect can be observed when producing larger initial droplet sizes [140, 231].

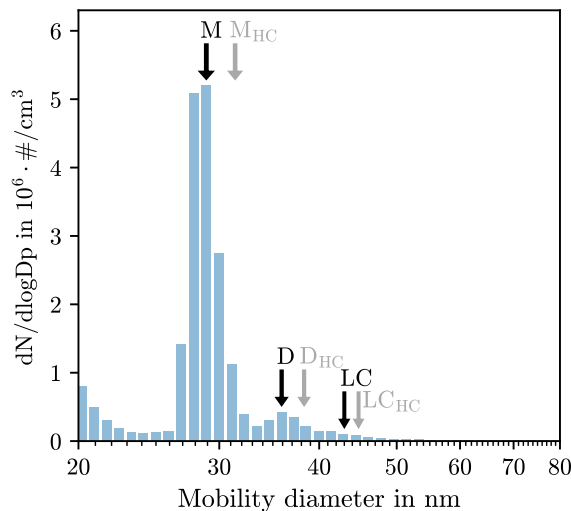


Figure 5.1.: The size distribution of electrosprayed erythrocrucorin, measured with a DMA. The monomer, dimer and large cluster positions are indicated by “M”, “D”, and “LC”, respectively. For a $10\times$ sample concentration increase, the peak positions of the monomers, dimers, and larger clusters shifted toward $\sim 2\text{--}3$ nm larger values, indicated by grey labels and the index “HC”. Ratios between the species and peak breadth changed as well, toward broader distributions and higher abundance of clusters, but this is not shown here.

For the deflection experiment, we used an experimental setup with an aerodynamic-lens stack (ALS) injector [162] as presented before [163], but with an added deflector, as shown in Figure 5.2. Ejected from the ALS, the particles were aerodynamically focused into a beam and into the chamber, propagating along the y axis. An Nd:YAG laser (Innolas, model SpitLight 600, $\lambda = 532$ nm, pulse width: 10 ns, repetition rate: 20 Hz, nominal pulse energy: 239 mJ) was positioned along x to cross the particle beam at $y = 0$, i. e., $\Delta y_{\text{ALS,elec}} + \Delta y_{\text{elec,det}} = 2.3$ mm downstream from the ALS. The undeflected beam of erythrocrucorin complexes had here a mean full width at half maximum (FWHM) of 110 μm . At the intersection position, at $x = 0$, the laser had a FWHM along y and z of 70 μm .

Scattering in the $-z$ direction from individual particles was observed with a camera-based microscope system, consisting of an objective (Edmund Optics, model 59-876) and a high-efficiency CMOS camera (Teledyne Photometrics, model Prime 95B). From the recorded images, scattering events were identified. Their two-dimensional (2D) positions in the xy plane were determined along with their scattering signal. The scattering intensity was measured by integrating the recorded gray values around the respective centers of the events in a circular region with a fixed radius of 4 pixels. Scattering from particularly large droplets or particles, e. g., resulting from momentary instabilities of the electrospray, exceeded the dynamic range of our camera. Images containing these saturated blobs ($< 2\%$ of all events) were excluded from further analysis.

At $\Delta y_{\text{elec,det}} = 1.1$ mm above the laser, an electrode setup produced an electrostatic field (voltage supply Aim-TTi, model PLH250-P, $V_{\text{max}} = 250$ V). The distance between the blades

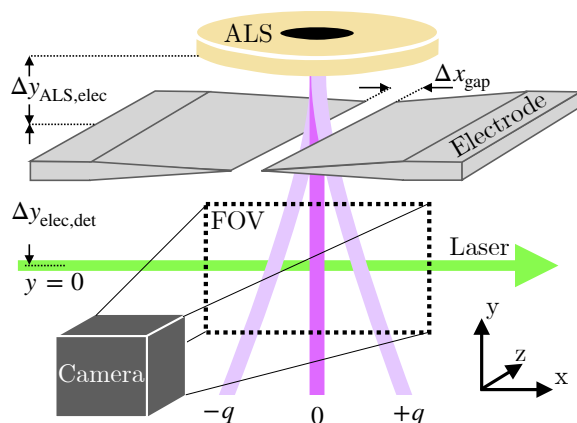


Figure 5.2.: The aerosolized sample was extracted into vacuum through an ALS, producing a focused particle beam (central purple line). The particles propagated along y direction and passed between two blade electrodes, which were positioned underneath the ALS. Further downstream, at $y = 0$, a laser illuminated the particle beam along x . Scattered light along the z axis was detected with a camera-based microscope. Charged particles (outer purple lines) dispersed in the electrostatic field according to the polarity of the electrodes.

was $\Delta x_{\text{gap}} = 0.55$ mm. We applied $+250$ V to one electrode, creating a field strength of ~ 4500 V cm $^{-1}$ between the blades.

5.3. Results and Discussion

Without an electric field, we observed the 2D position histogram for the erythrocrurin beam as shown in Figure 5.3 a). When passing through such a non-zero electric field, the previously narrowly-distributed particles dispersed, see Figure 5.3 b). In accordance with the polarity of the electrodes, positively charged particles were deflected to the right (36% of the 14774 events shown in Figure 5.3 b)), and negatively charged particles to the left (11%). Another significant portion of the beam (the remaining 53%) was unaffected by the field, indicating zero charge.

In order to identify the sizes of the biomolecules in the optically detected beam and to correlate them to the oligomeric species identified with the DMA-CPC setup, we compared the intensities of recorded scattering from erythrocrurin molecules with the scattering from known particle sizes. We chose PS as a model sample, as it is employed as performance reference for other light-based sample characterization methods, like dynamic light scattering [232]. Using the range of PS nanosphere sizes described above, we calibrated our imaging setup, which showed a linear trend between scattering signal and the diameter to the sixth power, in line with optical scattering theory from particles smaller than the incident wave length [117]. The PS data and the retrieved regression model are shown in Figure 5.4 a).

For applying this model to the scattering from erythrocrurin particles, next, we normalized the recorded signal in 1D along the y axis, using a Gaussian-distribution model of the spatial profile of our laser. The normalized intensities, scaled to scatterer sizes in nm with the

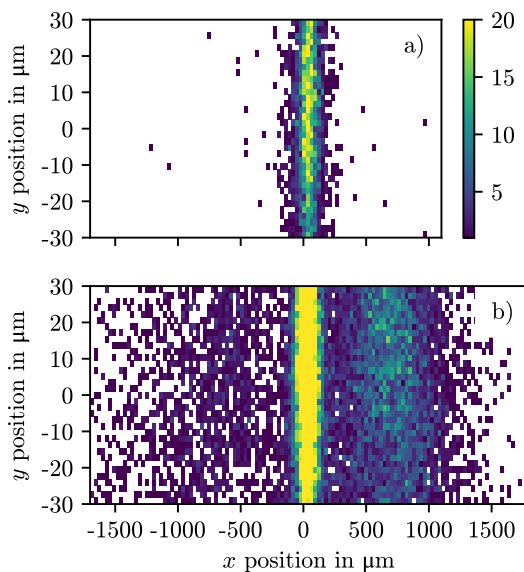


Figure 5.3.: 2D position histogram of erythrocrucorin. Particle-beam propagation along y . a): The cylindrically symmetric beam without application of a field. b): After applying an electrostatic field along the x axis, the beam dispersed. Positively charged particles deflected to the right, negatively charged to the left. The undeflected particles, which were detected at the same position as all particles in setting a), were neutral. The color scale corresponds to the number of recorded hits per pixel.

polystyrene-derived regression model, are shown as a histogram in Figure 5.4 b). The most probable size in this distribution is 31.5 nm, quickly falling toward larger diameters.

Next, we accounted for the laser z profile. Along the z axis, the positions of the particles were not measured, and so, an ambiguity was introduced: for example, a small particle on the laser axis yielded the same signal as a larger particle off-axis. For large distances from the focal distance of the objective, optical aberration may help reducing this uncertainty, see section B.2, but here, the particle beam had a narrow spread around the laser.

Instead, we assigned a range of possible size/ z position pairings to each hit, which would result in the same recorded signal.

Having an approximately cylindrically-symmetric particle beam, the assumed size/ z position distribution could be weighted according to the x axis profile of the particle beam, extracted from Figure 5.3 a), resulting in a description of each hit not as one definite size, but rather as a probabilistic size distribution (PSD).

The individual PSDs could now be compared to the expected sizes of the oligomers, yielding three derived probability values for each hit to belong to either a monomer, dimer, or larger cluster of erythrocrucorin. We calculated these values by multiplying the PSDs with Gaussian fits to the peaks observed in the DMA-CPC data.

Based on these results, the position histogram in Figure 5.3 could be complemented with species information. Figure 5.5 shows a visual representation of the oligomeric composition

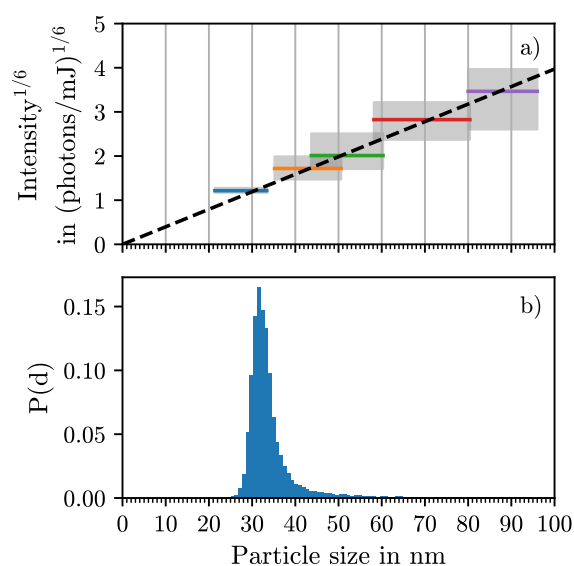


Figure 5.4.: a): Scattering signal from polystyrene reference sample, scaled to a laser pulse with an energy of 1 mJ. The colored horizontal lines indicate the median intensity of the respective batches, the gray boxes show the interquartile range of intensities. Their widths along the size axis is determined by the particle size distribution as provided from the manufacturers. A linear regression through the medians provides the calibration function for the biomolecules. 27.4 nm data is shown, but due to expected detection bias toward larger sizes, it is not included in the fitting. b): The scattered intensities from erythrocrucorin sample, corrected for the laser profile, and scaled into sizes in nm with the regression model from a). The most probable size is 31.5 nm.

within the same 2D bins, i. e., the pixels. Here, a blue color encodes a majority of monomers, red: dimers, and yellow: larger clusters. Overlapping distributions result in a composite color. While Figure 5.5 a) and Figure 5.5 b) provide a qualitative overview over the composition of undispersed and deflected beams, Figure 5.5 c) shows a line plot through the oligomeric representation of the deflected beam and allows a quantitative description. This representation helps disentangling the observed profile and identifying regions of high oligomeric purity. For example, at $x = 250 \mu\text{m}$, mainly singly charged larger clusters are found, contributing approximately 50% of all hits detected here. In contrast, at $x = 0$, in the center of the neutral portion of the beam, the fraction of large clusters is only 15%. Similarly, +1 charged monomers dominate the other singly charged species at $x > 600 \mu\text{m}$ with a fraction of approximately 65%. In comparison, there are 12% fewer neutral monomers in the center of the undeflected beam.

Beams of larger particles from our ALS were generally narrower than of smaller particles. The modulation of the purity plots at $x = 0$ reveals this size-specific particle focusing performance of the injector: while in the very center, narrow beams of larger clusters and dimers could be detected, toward $\pm 100 \mu\text{m}$ off axis, the fraction of broad-beam monomers increases.

Based on polystyrene sphere reference measurements, sizes could be assigned to scattering

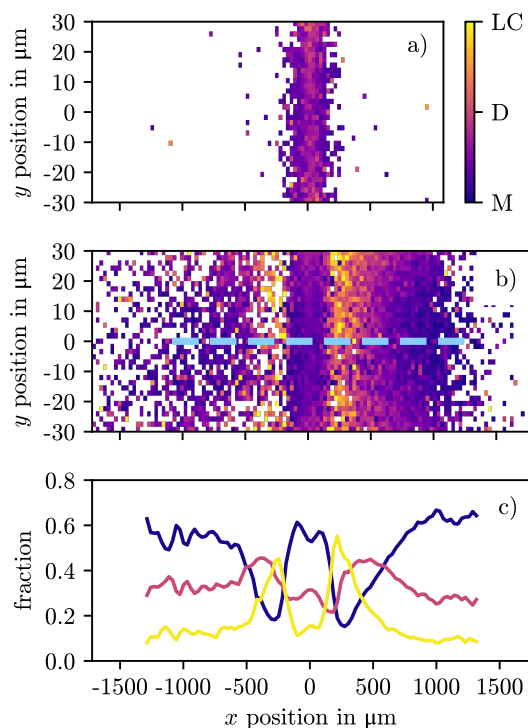


Figure 5.5.: For each recorded hit, three probabilities could be calculated for it to be a monomer, dimer, or larger cluster. The derived average oligomeric composition within each 2D bin is color encoded according to the scale shown next to a). a): In the cylindrically-symmetric undeflected particle beam, a mix of monomers, dimers, and larger clusters can be found along the central axis, represented by an average purple color, indicating a majority of monomers and dimers. b): When applying an electric field, the charged species separate from the neutral portion of the beam. Within the beams of charged particles, the monomers (blue) deflected furthest, overlapping with the less-deflected dimers (red), and the larger clusters (yellow). c): Along the blue dashed line in b), the fractions of oligomeric species are plotted in the corresponding colors. In the center, the ratios between species compare to the field-free experiment. At further distances, the deflected species overlap but regions with high individual purity can be identified. For example at $x = 200\text{--}250\ \mu\text{m}$, singly-charged large clusters can be found with a probability of $\sim 50\%$.

events from biological macromolecules. The corresponding size distribution, see Figure 5.4 b), showed a most probable particle diameter of 31.5 nm. Compared to the monomer diameter as measured with the DMA-CPC, it is shifted by 2.7 nm, which we ascribe to a limited detection efficiency of our imaging setup and detection bias toward larger particles. The same effect can be observed for the 27.4 nm polystyrene sample, see Figure 5.4 a): here, the median observed intensity corresponds to a particle of size of 30.5 nm, which can be retrieved from the intersection of the median intensity with the calibration curve, see Figure 5.4 a).

Furthermore, variations in effective particle size on the order of 2–3 nanometer can be

explained by deposition of non-volatile residue in the droplets upon evaporation [140]. The probability to observe these statistical differences increases with experimental time due to changes of electrospray conditions. Uncertainty in produced droplet size distribution due to for example partial clogging of the electrospray capillary can be reduced by careful filtering of buffer and sample beforehand, as well as employing a flow-rate controller, ensuring constant liquid flow and, correspondingly, constant produced droplet size throughout the entire experiment. Then, the shift of particle sizes with varying microconditions can be reduced. We plan to employ such a measure for future experiments.

The presented particle-beam characterization method provides means of characterizing the size and charge state distribution of aerosolized macromolecules and works reliable in a large size range for particles smaller than the wave length of the employed laser and allows identification of regions of pure particle species in respect to their charge and size. But with the scope of SPI to image proteins with even smaller diameters than erythrocrucorin, the laboratory-based particle-beam characterization tools should match this size range. With our best efforts, our ability to optically detect bio-macromolecules seems to be size-limited: 99% of the assigned sizes in the presented data had diameters ≥ 27.7 nm. In future setup iterations, different nanoparticle detection techniques could be applied, for example time-of-flight velocity map imaging methods, suited for identification of nanoparticles or their fragments.

5.4. Conclusion

We demonstrated the generation of high-density particle beams of erythrocrucorin macromolecules and independently analyzed the beams of PS spheres as reference samples, which we used as calibration of our optical detection setup. This allowed us to scale scattering from individual biomolecules in the gas phase to retrieve their diameter. The scaled scattering signal was interpreted as oligomeric species, the size ranges of which were determined with a DMA-CPC setup. Dispersion of monomers, dimers, and large clusters was observed and regions with high oligomeric purity could be identified.

Such beams of pure charge states promise high uniformity between particles. This is prerequisite for high-resolution imaging like SPI. Cherry-picking of sample species, e. g., in respect to their mass or charge state, will greatly improve SPI experiments, which rely on identical sample molecules for unambiguous structure assignment, especially when signal-to-noise ratios for single molecule diffraction images are small [63, 67, 68, 80]. With this compact setup, dense and pure particle beams can be generated, well-suited for SPI-type experiments, and with little change to existing setups.

Also, further means of particle control could be applied, like electrostatic focusing [226, 227]. Lastly, local purity could be improved with application of a knife-edge aperture [233]. Already, this is a promising step toward generating particle beams for SPI experiments of truly identical sample molecules.

6. Toward Deflection of Neutral Molecules for Single-Particle Imaging Experiments¹

In the previous chapters, electrostatic deflection of charged particles into beams of pure charge states was described. It was found that the amount and distribution of charges largely depends on particle sizes and the mode of aerosolization. In general, excess charging of gas-phase proteins should be avoided in single-particle diffractive-imaging (SPI) experiments, because charges induce Coulomb-repulsive bending and stretching of the investigated biomolecules [223, 224]. Note that this applies to external charges: a protein in ion-containing solution is charged, but simultaneously, few solvent layers around a protein in the gas phase act as a “nanobeaker” that is overall charge-neutral. Any additional charges, or even broad charge-state distributions, loaded onto these nano-environments apply force to the solvated biomolecules and deform them, i. e., introduce structural heterogeneity. Consequently, this chapter focuses on charge-neutral particles and how to purify them according to interparticle structural differences. More specifically, a electrostatic-deflector setup is proposed, which helps separating neutral particles based on yet another source of structural ambiguity: their conformational state.

6.1. Introduction

In SPI experiments, aerosolized single particles are successively exposed to the coherent x-ray photons of free-electron lasers (FEL). The resulting diffraction snapshots of the arbitrarily oriented molecules are classified and combined to overcome the inherently low signal-to-noise ratio of scattering from small biological sample like monomeric proteins. One goal of SPI is atomic-resolution structure determination of biological sample in a quasi-native state. A major requirement is structural homogeneity of the imaged molecules, because incoherent averaging of structurally diverse copies of the particles ultimately reduces achievable resolution [219]: structural heterogeneity of the sample is thus considered a bottleneck for high-resolution SPI experiments [218].

Proteins exhibit multiple conformations. These different conformers have the same mass-to-charge ratio and thus deflect identically in the charge-purification deflection setups described above. Probing mass-to-charge-purified particle beams in SPI experiments would yield diffraction snapshots from all conformational states that exist in the ensemble simultaneously. In principle, individual large particles with comfortably high signal-to-noise ratio in each recorded image can be classified according to their structure. It was proposed that this computational technique allows grouping the structurally heterogeneous ensemble and sample the conformational landscape [83, 193]. But applicability of this approach may be limited for weak scatterers. Instead, in this chapter, an experimental method for delivery of specific protein folding states into the interaction volume of an FEL is explored.

¹This chapter is foreseen for publication. I selected the model protein, simulated the fields, coded and performed the trajectory simulations, analyzed the data, and created the figures shown in this chapter.

Conformational-species selectivity for charged particles is achieved for example with ion-mobility mass spectrometry [234]. Here, differences between collisional cross sections of conformers co-existing in aerosol are employed to separate them. Due to the differences in drag, these conformers will exhibit shifts in passage time through a gas-buffered cell in an accelerating electric field. Feasibility of this conformer purification approach for SPI experiments is currently investigated [235]. However, this method applies to charged particles and not to the neutral ones, which are the focus of this chapter. Furthermore, ion-mobility separation is typically used in tandem with highly sensitive mass spectrometry detectors [236], which poses lower requirements on particle-number densities in generated particle beams. A way of overcoming low ion densities may be a trapping the charged particles and releasing them, synchronized to the pulse structure of the FELs [237].

Other methods to investigate gas-phase conformers were shown [238–240], which rely on matter-wave interference, hydrogen/deuterium-exchange mass spectrometry under partially non-physiological conditions, and impact kinetics on solid bodies, respectively, and may not be directly transferable to investigate these massive proteins at FELs.

Here, I follow a different approach: purification of charge-neutral conformational states by differences in their electronic properties, specifically, their dipole moments, which proved to be most feasible to be accessed experimentally. Compared to the charge-purification setups described in the previous chapters, manipulation of neutral particles in space due to their dipole moments requires higher field strengths and gradients, as was shown for members from the phenol family [106, 241, 242], microsolvated aromatic compounds [243], and even a 309 Da dipeptide [94]. *A priori*, it is not clear if this principle can also be applied to tens-of-kDa biological molecules like typical proteins.

In this chapter, an electric-deflector setup is proposed based on numerical calculations for spatially separating conformers of large, neutral, aerosolized biomolecules according to their structural and electronic properties, i. e., enabling the spatial separation of conformers. As a model system, the extracellular 75 kDa domain of the epidermal growth factor (EGF) receptor [244] was chosen, a molecule with large structural differences between its distinct folding states [245].

6.2. Methods

While inhomogeneous fields that are needed for electrostatic deflection of neutral molecules can be created in virtually infinite ways, basic design principles for deflectors of neutral molecules exist [246]. A technically straightforward example is a two-wire field, produced by two cylindrical electrodes [116, 247]. In SPI experiments, dense beams of macromolecules are produced *via* hydrodynamic confinement onto a central axis in aerodynamic-lens stacks (ALS), and here, the deflector was positioned parallel to the propagation axis of the particles, see Figure 6.1 a). The electrostatic potential in space around these electrodes was calculated by solving the Laplace equation with defined electrode boundaries for which I used a field-simulation framework (SIMION v8.1 [186]). Two electrodes with diameters of 1 mm and a center-point distance of 2 mm, i. e., with a 1 mm gap, were simulated as shown in Figure 6.2. The resulting potential array in the xz plane for symmetrically applied voltages $+U$ and

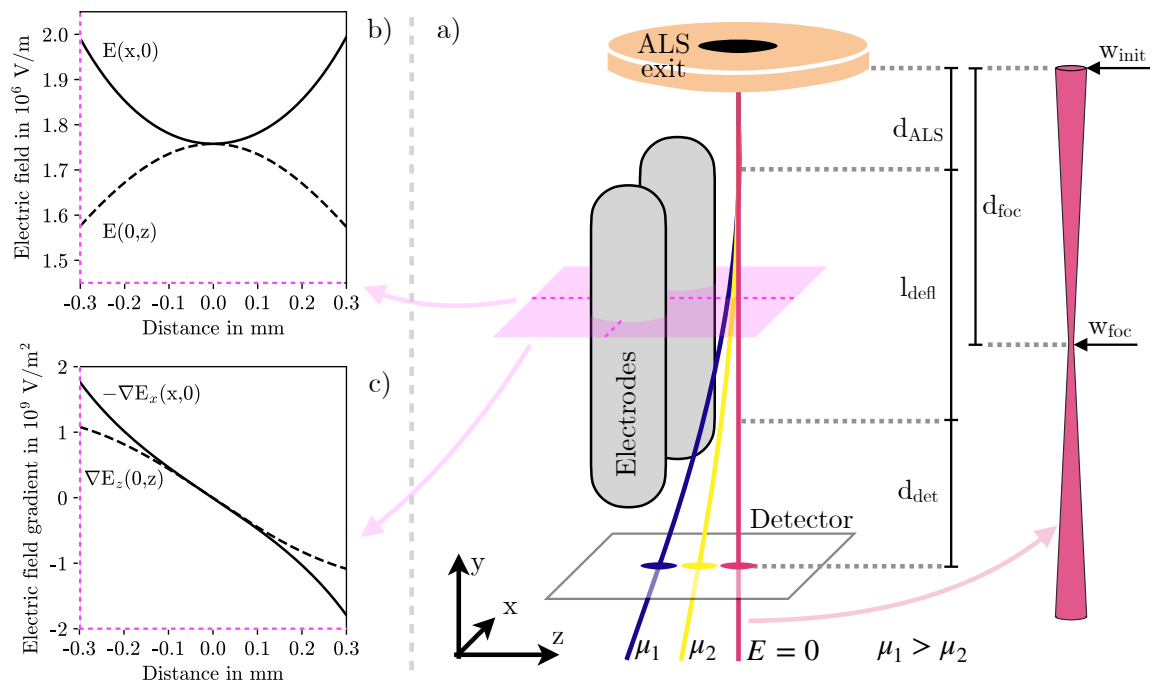


Figure 6.1.: a): A beam of ground-state molecules is prepared with an ALS. On the right-hand side in magenta, its focusing is shown qualitatively: from an initial spatial distribution of width w_{init} , the particles have a velocity along y together with smaller x and z velocity components, which lead to focusing of the particle beam to a width w_{foc} at a distance of d_{foc} below the exit of the ALS. Underneath the ALS, an magenta line represents the central axis of the beam. The corresponding particles are exposed to an electric between $y=d_{\text{ALS}}$ and $y=d_{\text{ALS}} + l_{\text{defl}}$ as shown in Figure 6.2. The electric field and gradient between the electrodes are shown in b) and c) along x and z . Qualitatively, they correspond to the results presented elsewhere [116]. The x gradient is shown with a minus sign for direct comparison of these two effects. Strong-field seeking particles deflect in z : the beam axes of two conformers with different dipole moments $\mu_1 > \mu_2$ are shown in yellow and dark blue. Along d_{det} , the particles linearly propagate until they are recorded at the detector.

$-U$ was exported as a mesh grid into Python [188] and scaled to $\pm 1000 \text{ V}$. From the two-dimensional (2D) potential, the corresponding electric field and electric-field gradient as first and second derivative of the potential were calculated. The field between the electrodes had a magnitude of 17.5 kV cm^{-1} and was assumed constant along y over the entire length of the deflector.

Electrostatic deflection of charge-neutral particles uses their space-fixed effective dipole moment μ_{eff} as molecular lever for spatial deflection. μ_{eff} has a permanent and a field-induced component. While polar molecules carry permanently separated partial charges, which make up the permanent dipole moment μ_{p} , charge separation due to an external electric field causes a induced dipole moment μ_{ind} even in non-polar molecules. Both μ_{p} and μ_{ind} interact

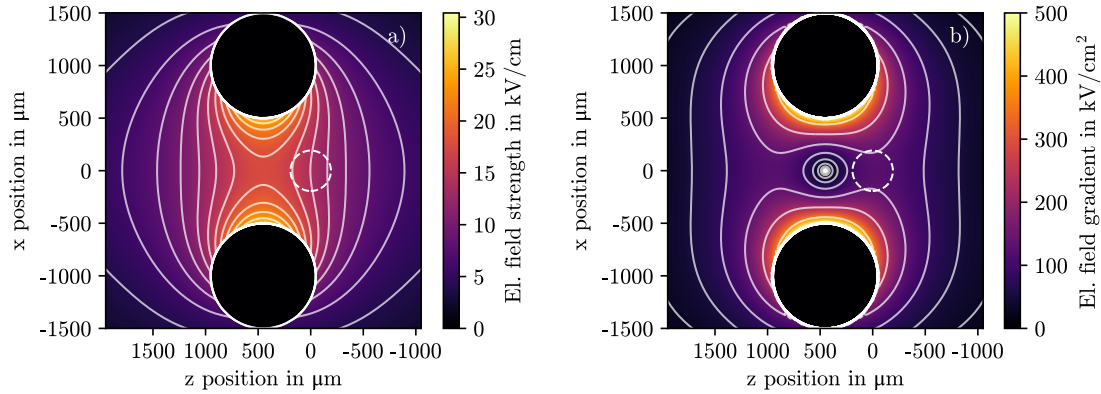


Figure 6.2.: a): The electric field of the described two-wire deflector setup. The two rod-shaped electrodes were modeled in the xz plane (solid black circles) with a diameter of 1 mm and a center-point distance of 2 mm. Application of ± 1000 V resulted in a field strength between the electrodes of 17.5 kV cm^{-1} , isolines of the field are indicated in white. The particle beam was initialized at the position marked with a white dashed circle, propagating perpendicularly into the image plane. b): The electric field gradient as derivative of the field. Isolines are shown in white.

with electric fields and the corresponding interaction energies can be expressed as

$$W_p = -\mu_p \cdot E \langle \cos \theta \rangle \quad (6.1)$$

$$W_{\text{ind}} = -\mu_{\text{ind}} \cdot E \langle \cos^2 \theta \rangle = \frac{1}{2} \alpha E^2 \langle \cos^2 \theta \rangle, \quad (6.2)$$

where the separability of partial charges of a molecule in an external field is described by the polarizability tensor α . Together, these energies yield μ_{eff} as their derivative with respect to the electric field:

$$\mu_{\text{eff}} = -\frac{\partial(W_p + W_{\text{ind}})}{\partial E} = \mu_p \langle \cos \theta \rangle + \alpha E \langle \cos^2 \theta \rangle. \quad (6.3)$$

The magnitude of interaction is determined by the degree of alignment, expressed by the angle θ between the dipole and the field [109]. With this, the force F acting on an object with an effective dipole moment μ_{eff} in an electric field with non-zero field gradient ∇E is defined as [106]:

$$F = \mu_{\text{eff}} \nabla E. \quad (6.4)$$

For simplicity, an ensemble of cold molecules in their ground state but with distinct folding states was assumed, all perfectly aligning in an electric field so that $\langle \cos \theta \rangle = \langle \cos^2 \theta \rangle = 1$.

As a model system, domains of the EGF receptor were chosen, which undergo significant structural changes between conformational states. The corresponding protein data bank identifiers (PDB-IDs) are 1NQL [248] for the closed, and 3NJP [249] for the open conformation, shown in insets in Figure 6.3 d). The permanent dipole moment of the protein sample

shown here was determined with a freely available online tool [100]. The polarizability tensor as integral part of μ_{ind} was first approximated for perfect conductors with same shape as the considered molecules using a computational framework (ZENO [103]) and then scaled to values reflecting properties of physiological proteins [104]. The corresponding values are presented in Table 6.1. The induced dipole moment scales proportionally to the

Species	μ_{p} in D	α in $\text{C m}^2 \text{V}^{-1}$	μ_{ind} in D
1NQL	719	$1.43 \cdot 10^{-36}$	0.76
3NJP	1359	$1.59 \cdot 10^{-36}$	0.82

Table 6.1.: The calculated permanent dipole moment (μ_{p}), mean polarizability (α), and field-induced dipole moment (μ_{ind}) of two folding states of EGF receptor domains, PDB-IDs 1NQL and 3NJP. Polarizabilities were determined for perfect conductors and scaled to values reflecting protein properties. The shown value of μ_{ind} corresponds to an electric field of 17.5 kV cm^{-1} .

electric field strength. With the determined polarizability values, the magnitude of the induced dipole moment in a field of 17.5 kV cm^{-1} is approximately 0.1% of the magnitude of the permanent dipole moment. Negligible contribution of μ_{ind} to the effective dipole moment in experimentally feasible electrostatic fields was also found elsewhere [108–110, 250]. Thus, together with the assumed perfect degree of alignment, in very good approximation, $\mu_{\text{eff}} \approx \mu_{\text{p}}$.

Further relevant molecular properties, i. e., spatial distributions of the particle beams and particle velocities, were estimated based on simulations and extensive experimental experience [161–164, 187]. The particles were time-step propagated along y starting from the ALS exit in steps of 500 ns. The $l_{\text{defl}} = 7.0 \text{ mm}$ long deflector was positioned to leave a gap of $d_{\text{ALS}} = 1.5 \text{ mm}$ toward the ALS, so as to avoiding short circuits. This gap was approximated as field-free space and so was the space below the detector, along d_{det} . By neglecting the fringe field above and below the deflector, a systematic error was introduced, but the field there could be assumed weaker than along the electrodes, where the majority of spatial deflection took place. For extensive (three-dimensional) simulations, the fringe field should be taken into consideration.

Two sets of 5000 particles for each conformer were initialized in a beam with a full width at half maximum (FWHM) of $w_{\text{init}} = 350 \mu\text{m}$ at the ALS exit, focused to $w_{\text{foc}} = 125 \mu\text{m}$ at $d_{\text{foc}} = 5 \text{ mm}$ below the injector. The particles were assumed to have a velocity of 50 m s^{-1} . After d_{ALS} , at each time step the local field gradient within the inhomogeneous field of the two-wire deflector was evaluated and the particles accelerated according to their dipole-to-mass ratios. They were drawn into regions of higher field strength, because these complex molecules in their ground state could be assumed to be strong-field seeking molecules [113–116].

After the particles passed the length of deflector, they linearly propagated for another distance of d_{det} before their xz positions were recorded, $d_{\text{ALS}} + l_{\text{defl}} + d_{\text{det}} = 10 \text{ mm}$ below the ALS.

6.3. Results and Discussion

From an initially mixed particle beam of equal content of either conformer, the conformers with different dipole moments deflected and separated into partially overlapping beams. The detected spatial distributions of 3NJP and 1NQL are shown in Figure 6.3 a) as two-dimensional scatter plots. Both beams of distinct conformers were shifted from the position of the undeflected beam, also shown there. Due to the field gradient components in the xz plane, see Figure 6.1 c), the particles focused along the z axis and defocused along the x axis, which is partially visible in the 2D distributions. Figure 6.3 b) shows projection of the 2D positions in a) onto the z axis as a histogram. The most probable z positions are indicated with red markers, a cross for the open conformer 3NJP and a circle for the closed conformer 1NQL. They were separated by 260 μm and had respective FWHMs of 310 μm (3NJP) and 360 μm (1NQL). Relative abundance of the conformers in each z bin is shown as local purity of the two species in Figure 6.3 d), solid lines. Purities of approximately 80% were achieved at the marked positions of highest z -axis particle number density. At distal z positions, the respective purities increased, at cost of a decrease in number density.

The effect of narrower particle beams on z -axis resolution between the beams of pure conformers, i. e., the ratio of inter-peak distance over the average particle-beam widths [251], was included as an additional result in Figure 6.3 c). In the simulations, narrower beams were achieved by shifting the particle-beam focus into the detector plane, i. e., to $d_{\text{foc}} = d_{\text{ALS}} + l_{\text{defl}} + d_{\text{det}}$. All other simulation parameters were kept constant. In this scenario, the beams could be better separated: while having the same inter-peak distance of 260 μm , the beams both only had widths of approximately 160 μm . This is reflected also in the purity plot, Figure 6.3 d): at the position of highest particle number densities, which were the same as in the first described results and are also marked with a cross (3NJP) and a circle (1NQL), the relative species purities increased for both conformers to almost 100% (dashed lines).

The shown results describe well-separated beams of pure conformational states. Even with a short deflector and experimentally feasible electric field strengths, significant deflection of the proteins could be observed. For the particle beams that focused at the detector, number density and resolution between the peaks was higher than for the beams that had their focus closer to the ALS exit, which diverged toward the detector. However, experimentally, a 125 μm beam focus of 10 nm proteins at $d_{\text{foc}} = 10$ mm may be challenging to achieve and a particle beam focus at $d_{\text{foc}} = 5$ mm more realistic at this point.

In both cases, when realizing this experiment, the observed particle beams would likely broaden and separability between deflected species decrease, majorly affected by non-zero distribution of thermal energies within the molecular ensemble. In comparison, the dipole-field-interaction energy of the considered proteins, see Equation 6.1, has approximately the same order of magnitude as the thermal energy $k_{\text{B}}T$ at room temperature. Warm proteins would not perfectly align, as was assumed above, and mean deflection decrease with $\langle \cos \theta \rangle$. Furthermore, with populating a broad range of energy levels, the conformer beams would disperse. As an effective way to produce cold beams of macromolecules, cryogenic buffer-gas cells could be employed, shock-freezing the particles to 4 K [252]. The cold particles emitted from such a device could then be focused into a particle beam using an ALS [253]. Cooling the particles would have the additional benefit of minimizing Brownian motion, which causes

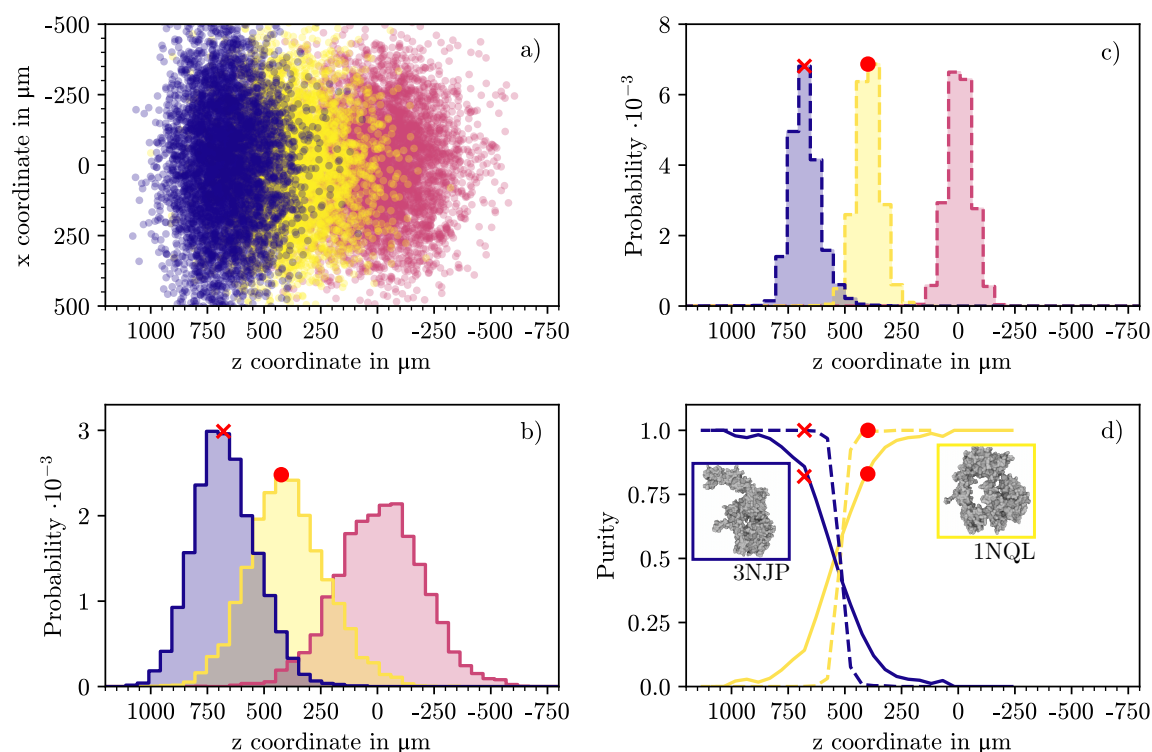


Figure 6.3.: a): Scatter plot of the recorded xz positions of the undeflected particle beam (magenta), conformer 1NQL (yellow), and 3NJP (dark blue). The open conformer 3NJP has the larger dipole moment and deflects further. Asymmetric focusing along z and defocusing along x can be observed. b): Projection of the recorded positions in a) onto the z axis. The distributions are shaded translucently in the same color scale, revealing overlapping parts of the particle beams. Positions with highest number densities for the two conformers are indicated with red markers, a cross for 3NJP and a dot for 1NQL. c): The same parameters as in b) were used, but with moving the particle-beam focus into the detection plane. Narrower particle beams lead to smaller regions of overlap. The same positions of highest number density as in b) are indicated. d): Along z , the relative purities of conditions b) (solid lines) and c) (dashed lines) are shown. At the positions of highest particle number density, the purity increases from approximately 80% (broader particle beam, condition in b)) to almost 100% (narrow particle beam, condition in c)). In the insets, the structures of the two conformers are shown.

broadening of the particle beam [161]: narrow beams of 10 nm proteins as defined above are more likely achievable using cold particles.

Spatial deflection of the conformer beams could be enhanced with the magnitude of the field gradient. In this example, a low electric field was applied compared to experimentally achievable field strengths [108]. Along these lines, the deflector geometry could be tailored to produce optimized gradients compared to the ones from a generic two-wire setup [246], leading to improved spatial deflection. Experimentally, designing these fields is at some point limited by electric breakdown and should be done cautiously.

The magnitude of deflection can also be controlled with particle speed: higher y velocities with otherwise unchanged parameters lead to a proportional reduction of deflector passage time and dipole-induced gradient acceleration, and thus, to quadratically reduced z deflection. This means, that slow particles are preferred for achieving strong spatial deflection and separability.

In any case, an additional tool for improving the local purity of species, which was applied in molecular-deflection experiments, is a knife edge skimmer, with which particle beams are skimmed appropriately and relative purities increase [233].

Having produced beams of macromolecules with pure conformational states deflected along z , they could be sampled in SPI experiments with the FEL pointed along x . With the particle beams focusing along z , this setup would have the additional benefit of increased particle number densities and higher encounter rates between x-rays and particles. While in this proposed experiment, a molecule with structurally distinct folding states was selected for showing general feasibility of the method, the technique could be potentially optimized to resolve more subtle differences between conformers. This would not only apply to folding states already co-existing in solution, but could at some point assist in dispersing beams of reaction-triggered proteins to sample their structure along reaction pathways. Spatial separation between these states would enable investigation of the different structural motifs in much more detail and with higher accuracy than with purely computational methods, and also help unravel more of the energy landscape of these complex molecules.

6.4. Conclusion

In a simplified model, numerical calculations showed general feasibility of spatial separation of two charge-neutral kDa protein conformers. A two-wire electrode setup was used with low field strengths, causing deflection of particles in its inhomogeneous field proportional to the dipole-to-mass ratio of the molecules. Trajectory simulations of slow, ground-state molecules with significantly different dipole moments were performed. Analysis of the spatial distributions of the conformer-purified particle beams revealed high local species purity, depending on the assumed initial particle-beam widths, with simultaneous high number densities.

The compact deflector described here could well be used for creating particle beams with high conformer purity and particle number densities of massive neutral biomolecules. This is an important step towards delivery of identical particles into the focus of an FEL and a prerequisite for atomic-resolution SPI experiments on proteins.

7. Conclusion and Outlook

Single-particle diffractive imaging (SPI) at free-electron lasers (FEL) is a method for imaging biological macromolecules, like proteins. Coherent x-rays scatter off arbitrarily oriented and isolated molecules in the gas phase and the snapshots are classified. Each class of particles with same structure and orientation is averaged, which helps overcoming the low signal-to-noise ratio of the individual diffraction patterns. Potentially, atomic resolution can be achieved. A bottleneck in achieving this level of detail is structural heterogeneity of the sample.

In the presented work, steps were taken toward producing structurally homogeneous gas-phase sample. First, it was shown how charges on aerosolized nanoparticles can be characterized. Significant charging of artificial nanoparticles was detected, which may be an unexpected result coming from a non-ionizing aerosolization technique. But the charge-state distribution (CSD) can be controlled: gas-phase particles from an electrospray-ionization device, coupled to a neutralizer, showed only few and low charges, which could be reduced even more by modulating the liquid-flow rate of the sample. Only when increasing the flow rate to higher values than needed for initial transfer of the molecules into the gas phase, the expected CSD [151–153] was matched. For all settings, clear separation of particle beams with pure charge states was observed. Next, charge-state separation was applied to biological macromolecules, i. e., the protein complex erythrocrucorin. Based on calibrated optical scattering signal, spatial regions of pure particle size and charge could be identified. Finally, the research focus was shifted from overall-charged to net-neutral particles. In a simplifying approach, deflection and separation of neutral conformers of a biological model system was simulated.

A few take-home messages can be deduced from these results. Firstly, aerosolized particles are heterogeneous. They have distributed charges, are either isolated monomers or aggregated into oligomers, are in different folding states, and spraying conditions affect their hydration layers and residue adduction, i. e., their effective size. Quantitative characterization in regard to these and potentially more properties is crucial for delivering homogeneous sample in SPI experiments. For example, compact electrostatic-deflector setups and appropriate detection techniques like the ones shown in this work help in online analysis and maintaining constant conditions.

Secondly, charges and oligomeric species of both artificial and biological nanoparticles, as well as conformational species of massive proteins can be spatially separated with the here shown approaches, producing purified and dense particle beams that are well-suited for application in SPI experiments.

Next, charging is a result from the aerosolization process, and not from the transport into the detection chamber. This is evident from the significantly different CSDs from different aerosolization methods, which used the same differential-pumping and injection setup.

Furthermore, the condition of gas-phase nanoparticles and macromolecules depends on the aerosolization mode. There is a delicate balance between flow rate, charging of the sample, and apparent particle size, which needs to be explored carefully. High flow rates

in electrospray-neutralizer setups seem to reduce charges, while they produce larger initial droplets, which in return cause deposition of non-volatile residues onto the sample. This should be kept to a minimum, as it potentially cloaks the structure of the molecule. Instead of using high liquid flow, an optimized, higher-performing neutralizer could be employed that reduces charges (more) effectively.

Finally, simulation of deflection of neutral molecules based on their dipole moment stressed the importance of generating cold beams of macromolecules for SPI experiments. From higher degrees of alignment in electric fields, to less-dispersed deflected beams, to narrower particle beams in general due to minimizing the broadening effect of Brownian motion, to potentially flash-freezing and capturing protein structures: the cooling of particles promises a range of significant experimental benefits.

When working on laboratory-based particle-beam characterization, especially for smaller particles than the ones presented in this work, the detection method would likely need to be adapted. The optical-microscope setup that was employed for generating the shown results was very useful for characterizing particle beams and particle-size distributions. It seems, however, to be limited in regard to detecting even smaller sample, for which detection efficiency dropped. In terms of organic compounds, like the macromolecules presented in chapter 5, the smallest reliably detected particle size was approximately 27 nm. Typical proteins are smaller, and incident laser intensity would need to be increased by more than 350 times to achieve similar detection efficiency for 10 nm sample. While for example much tighter focusing of the laser may be feasible, it would reduce the detection volume and thus complicate the characterization process.

Overall, this work presented mechanisms that can be used for characterization and control of aerosolized nanoscopic particles, like macromolecules, using electrostatic fields. When implementing these, and potentially many more, technical, scientific, and conceptual results, a new level of species selectivity in sample delivery could be achieved in SPI experiments, paving the way toward atomic-resolution structural imaging, and, in the next step, to capturing the ultrafast dynamics of individual biological macromolecules.

Compact electric deflectors like the blade geometry for charged particles or the two-wire setup for neutral molecules could be straightforwardly implemented in existing FEL endstations. Experimentally comfortably manageable voltages and fields would allow for high levels of control of charged and conformationally diverse sample. Cold beams of macromolecules would then further improve experimental outcome, as indicated above. Efforts toward producing those cold beams are ongoing and previous results have shown that cooling macromolecules down to 4 K with buffer-gas cells for SPI experiments is within reach. Especially when producing beams of < 25 nm particles, Brownian motion of the molecules could be reduced, allowing for narrow particle beam foci, for example like the ones assumed in chapter 6. Narrow beams in principle yield high particle number densities, and thus, high hit rates, i. e., number of x-ray scattering events per time, a metric of experimental efficiency. Also in neutrals-deflection experiments, particles with low thermal energy are preferred, as stronger directional confinement can be achieved. Spatial deflection of molecules scales with the degree of alignment, and so, lower electric fields are necessary to separate beams of pure conformers. Furthermore, with thermal energies within the molecular ensemble reduced to a narrow and low range, dispersion in the field would be minimized.

Means of control could for example be applied in SPI experiments as follows: first, a biological macromolecule, like a protein, is prepared in solution. Using an appropriate aerosolization technique like electrospray-ionization, the sample is transferred into the gas phase. In an effective neutralizer, the majority of droplets is then stripped of excess external charges, minimizing the effect of Coulomb-repulsive bending and stretching. The small and monodisperse droplets evaporate during transport into the interaction region, leaving few, stabilizing water layers that maintain quasi-physiological environment while exposing as much of the protein structure to the FEL x-rays as possible. Passing through a cryogenic buffer-gas cell, the molecules are shock-frozen and aerodynamically confined into narrow particle beams. Underneath an aerodynamic-lens-stack injector, an inhomogeneous-field deflector then removes all net-charged particles from the particle beam. Also, it deflects and disperses the beam according to the effective dipole moments of the particles within. Since structural changes are often correlated with changes in the dipole moment, ideally, the initially structurally diverse beam is now dispersed and regions of molecules with virtually the same structure have emerged. Scanning these structural species across the FEL allows sampling conformational pathways, for example following a reaction that was triggered before freezing the particles. Employing yet another control mechanism, the molecules can also be spatially oriented before diffractive imaging, allowing for more unambiguous data assignment in structure reconstruction, and thus, potentially higher imaging resolution [73]. Spatial orientation of particles can be induced with lasers, as was shown for smaller molecules [254–257] and already implemented at FEL facilities [258]. Efforts toward translating these results to large biomolecules are ongoing.

Albeit not atomically resolved, motion of artificial nanoparticles and even massive biological complexes could already be observed [82, 83]: when combining and further improving particle-control mechanisms, the SPI-produced, atomically resolved molecular movie of small proteins does not seem impossible.

A. Evaporation of Nanodroplets

A.1. Evaporation of Nanoscopic Droplets in the Gas Phase

After vaporization, the sample molecules are immersed in few hundreds of nanometers sized aqueous droplets. Depending on their environmental conditions such as local vapor pressure, the solvent starts to evaporate immediately, causing a drop in droplet temperature. This cooling has the effect of reducing the vapor pressure, slowing down evaporation and with it, the rate of temperature change. While injecting liquid jets into vacuum, this effect was observed to the point of self-limitation, where the evaporation rate slowed down quickly due to fast cooling to supercooled temperatures [259]. But this is not what we expect in the electrospray ionization process to happen: we do not observe supercooled water, which eventually should turn into ice, in our optical imaging setup, nor in SPI experiments. Instead, when injecting water with ammonium acetate but without sample, virtually all droplets seem to evaporate and we don't observe hits from optical scattering.

Complete evaporation can be explained by taking into account heating by gas molecule collisions, which are non-negligible during injection and aerosolization into room-temperature-, atmospheric conditions. A graphical representation of the process is shown in Figure A.1.

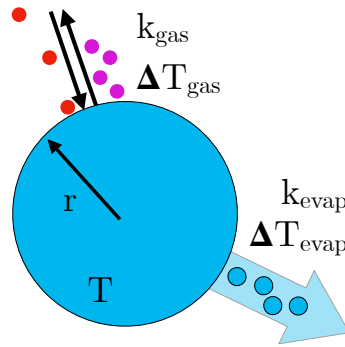


Figure A.1.: Droplet evaporation scheme. A droplet of radius r and with uniform temperature T shrinks in size due to evaporation at a rate of k_{evap} . With each evaporation event, temperature is reduced by ΔT_{evap} . Simultaneously, room-temperature gas molecules collide at a rate k_{gas} , each time raising the temperature of the droplet by ΔT_{gas} .

The following assumptions and simplifications are made in an attempt to describe a simple model for droplet evaporation from aerosol sources:

- the perfectly spherical droplet consists of pure water with temperature-independent density,
- atmosphere consists of pure N_2 at $1.013 \cdot 10^5$ Pa and 273.15 K.
- Temperature change throughout the droplet is instantaneous,
- only droplet cooling due to evaporation and
- only droplet heating due to gas molecule collisions are considered, where

- gas molecules are purely classical “solids”, which completely and perfectly thermalize upon contact with the droplet and do not re-collide with the droplet until they are thermalized to environmental temperature.
- The gas molecules have uniform velocity and temperature, which are the averages of Boltzmann-type distributions.
- All phenomena are purely classical.

We assume a water droplet of radius r_d at temperature T_d in gas of temperature $T_g = 298.15$ K and pressure $p_g = 1.013 \cdot 10^5$ Pa in a time interval of dt . A rate equation can be applied:

$$\frac{dT_d}{dt} = -k_{\text{evap}} \cdot \Delta T_{\text{evap}} + k_g \cdot \Delta T_g, \quad (\text{A.1})$$

where:

dT_d/dt	rate of temperature change of the droplet in K s^{-1} ,
k_{evap}	rate of molecular evaporation in s^{-1} ,
ΔT_{evap}	temperature change induced by single evaporation event in K,
k_g	rate of gas molecule collision with the droplet in s^{-1} , and
ΔT_g	temperature change induced by single collision event in K.

The evaporation-induced temperature change has a negative sign because it reduces the droplet’s temperature. The evaporation rate of water¹ from the droplet and induced temperature change were described [264] as

$$k_{\text{evap}} = \alpha \frac{p_{\text{vap,w}}}{\sqrt{2\pi m_w k_B T_d}} A_d, \quad (\text{A.2})$$

where:

α	dimensionless evaporation efficiency [0,1] (which is assumed perfect, i. e., $\alpha = 1$),
$p_{\text{vap,w}}$	vapor pressure of water in $\text{kg m}^{-1} \text{s}^{-2}$,
m_w	mass of a water molecule in kg,
k_B	Boltzmann’s constant = $1.380\,649 \cdot 10^{-23} \text{ kg m}^2 \text{ K}^{-1} \text{ s}^{-2}$,
T_d	droplet temperature in K, and
A_d	droplet surface area in m^2 ,

and

$$\Delta T_{\text{evap}} = \frac{\Delta H_{\text{vap}}}{V_d \rho_w c_w}, \quad (\text{A.3})$$

where:

ΔH_{vap}	latent heat of evaporation in J M^{-1} ,
V_d	volume of the droplet in m^3 ,
ρ_w	density of water in kg m^{-3} , and
c_w	heat capacity of water in $\text{J kg}^{-1} \text{ K}^{-1}$.

¹for droplets with $r < 10$ nm, the vapor pressure should be surface-tension corrected [260–263]

Equation A.2 describes the amount of molecules leaving the droplet per second, which in turn implies an evaporated volume, given the number density of water molecules, and a correlated effective droplet radius decrease, which changes $k_{\text{evap}} \propto A_d(r)$.

Gas molecules collide with surfaces at an average rate [265] of

$$k_g = n_g \frac{\langle v \rangle}{4} \cdot A_d, \quad (\text{A.4})$$

where:

n_g number density of gas molecules in m^{-3}
from $pV = \frac{n_g}{N_A} RT$ [266], and

$\langle v \rangle$ expectation value of the speed of gas molecules in m s^{-1}
from the three-dimensional speed distribution of Maxwellian gas molecules:

$$f(v) = 4\pi v^2 \left(\frac{m}{2\pi k_B T} \right)^{\frac{3}{2}} \exp \frac{-mv^2}{2k_B T} \text{ and the one-dimensional velocity components:}$$

$$j=x, y, z: f(v_j) = \left(\frac{m}{2\pi k_B T} \right)^{\frac{1}{2}} \exp \frac{-mv_j^2}{2k_B T}.$$

With a finite speed of the water droplets v_d , and defining propagation along x , the expectation value of v becomes

$$\langle v \rangle = \left\langle \sqrt{(v_x - v_d)^2 + v_y^2 + v_z^2} \right\rangle \quad (\text{A.5})$$

as a shift of the 1D Gaussian velocity distribution of the gas molecules, which here is defined only along x . The gas collision rate changes and increases accordingly. In a first approximation we can now assume a hard sphere model and simplify the interaction between water droplet and a gas molecule as two solid bodies getting in contact, both thermalizing toward a shared temperature T_f , and separating again instantaneously. The gas molecules are then assumed to thermalize in bulk to reservoir temperature before re-colliding with the droplet. Furthermore, the droplet as a whole is assumed to have a perfect internal thermal conductance.

Two bodies in thermal contact will thermalize to an equilibrium temperature as

$$Q = c_{w,N_2} \cdot m_{d,N_2} \cdot \left(T_{(d,N_2),i} - T_{(d,N_2),f} \right), \quad (\text{A.6})$$

where:

Q exchanged heat during thermalization in J,
 m_{d,N_2} mass of droplet and gas molecules in time increment in kg, and
 $T_{i,f}$ initial and final temperature in K.

This leads to a change, which in our case typically is an increase, of the temperature of the droplet:

$$\Delta T = T_{i,d} - T_f = T_{i,d} - \left(\frac{c_{N_2} \cdot m_{N_2} \cdot T_{i,N_2} + c_w \cdot m_d \cdot T_{i,d}}{c_{N_2} \cdot m_{N_2} + c_w \cdot m_d} \right). \quad (\text{A.7})$$

Since supercooled temperatures were not reached, a model for the temperature range [262.15 K, 298.15 K] was used [267] for the heat capacity of water:

$$c_w \approx A + BT + DT^2, \quad (\text{A.8})$$

where:

$$\begin{aligned} A & 134.4 \text{ J M}^{-1} \text{ K}^{-1}, \\ B & -0.385 856 \text{ J M}^{-1} \text{ K}^{-2}, \text{ and} \\ D & 6.294 22 \cdot 10^{-4} \text{ J M}^{-1} \text{ K}^{-3}. \end{aligned}$$

The heat capacity of nitrogen, c_{N_2} , was modeled [268] in the temperature range [100 K, 500 K] as:

$$c_{\text{N}_2} \approx A + B\tau + D\tau^2 + E\tau^3 + \frac{F}{\tau^2}, \quad (\text{A.9})$$

where:

$$\begin{aligned} A & 28.986 41 \text{ J M}^{-1} \text{ K}^{-1}, \\ B & 1.853 978 \text{ J M}^{-1} \text{ K}^{-2}, \\ D & -9.647 459 \text{ J M}^{-1} \text{ K}^{-3}, \\ E & 16.635 37 \text{ J M}^{-1} \text{ K}^{-4}, \\ F & 1.17 \cdot 10^{-4} \text{ J K M}^{-1}, \text{ and} \\ \tau & \text{temperature } T/1000 \text{ in K.} \end{aligned}$$

After having found expressions for the involved collision and evaporation rates and corresponding changes in temperature, these can be described for a time increment dt . Then, the radius of the droplet decreases and with it its temperature and the magnitude of many of the aforementioned parameters, which are temperature and/or radius dependent themselves.

Putting all of this together, the droplet starts evaporation at room temperature. Evaporative cooling reduces its temperature at a rate proportional to its surface. In vacuum, shrinking slows down due to quickly reaching supercooled temperatures which also was shown elsewhere [269, 270]. In our case, however, interaction with gas molecules prevents reaching the supercooled regime. Heat transfer here is also proportional to the surface of the droplet but collision-induced heating increases with sinking droplet temperature: in the assumed conductive-thermalization model of solid bodies, the expected absolute temperature change of the droplet is proportional to the temperature difference between droplet and gas. The two counteracting heating and cooling rates for the considered case find an equilibrium and stabilize the temperature of the droplet at a value > 273.15 K, which is what would be expected from everyday observations: sprayed droplets in a room do not typically freeze but evaporate completely.

Taking this model, we get an idea about the evaporation of droplets after being transferred into the gas phase. In a highly entangled process, the droplet evaporates and exchanges heat with its environment. As shown above, see subsection 2.2.3, spraying under varying conditions leads to different initial droplet size and charge, which results in differently sized liquid droplets entering the neutralizer and passing through it.

Taking two examples: first, the electrospray-flow rate is chosen to achieve stable spraying in Taylor cone mode and the resulting initial droplet radius is approximately 75 nm, a typical value for low sample-flow rates. For the second setting, higher flow even beyond

the cone mode causes larger initial droplets, i. e., 250 nm radius. In both cases, an $r_p = 44$ nm particle is embedded in the center of the droplets, without changing anything for this model, but only the minimum achievable droplet size. Evaporation stops when the droplet has the size of the particle. Shown in Figure A.2 is how very different flow rates and initial spraying conditions prepare different environments for the electro sprayed particles and cause a significantly different history for them.

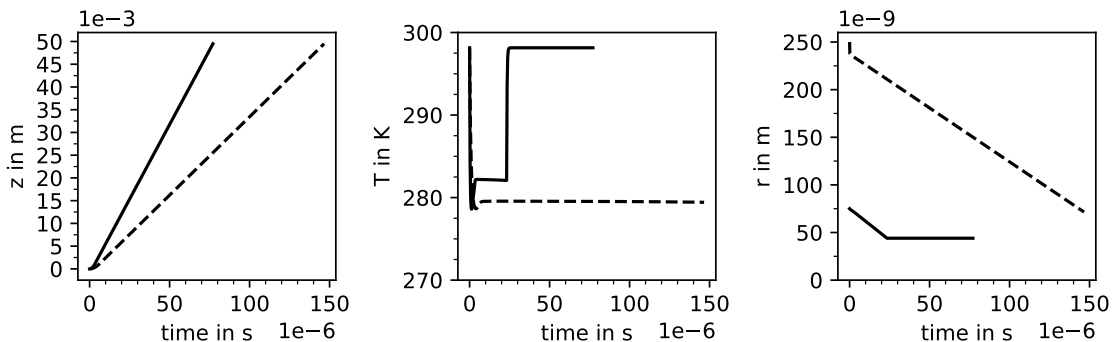


Figure A.2.: Histories of $r = 75$ nm (solid line) and $r = 250$ nm (dashed line) droplets. They propagate at linear velocity after a short acceleration time and passing the electrode. Having an approximately 50 mm long neutralization chamber, the droplets have passed it at $t_{75} = 80 \mu\text{s}$ and $t_{250} = 150 \mu\text{s}$. The temperature of the droplets decreases from room temperature due to evaporative cooling. With initially low velocity, the gas collisions are less frequent at first, but they increase with the accelerating particles. This explains the undershooting temperature at short time scales. But then, with constant speed after passing the electrode, it stabilizes due to constant velocity, and at a higher level for the faster 75 μm droplet. The radius of the droplets decreases linearly after initial phase, and when they reach the size of embedded particle ($r = 44$ nm), evaporation stops, and the dry particle has constant diameter. Also, evaporative cooling stops and the temperature increases to the room temperature of the gas molecules.

Both model droplets are initialized with a charge corresponding to the Rayleigh limit, see Equation 2.4. They accelerate due to an applied electro spray voltage of 2 kV from an electrode which is 1 mm away from the origin of the particles. The initially smaller droplet accelerates faster, compare Equation 2.5. After having passed the electrode, the droplets propagate with constant speed, see Figure A.2, left panel. In the middle panel, the temperature evolution is shown. When the droplets are slow, the temperature drops quickly due to evaporative cooling. But with accelerating droplets, the gas molecule collision rate increases and so does the temperature of the droplets. A plateau is reached where the collisional heating balances evaporative cooling. This level is higher for the smaller and faster 75 μm droplet than for the larger 250 μm droplet. This introduces a slight difference in evaporation rate, which is too low to be seen in the shown data. In the right panel, the shrinking of the droplets is shown. Over most of the observed time, it progresses linearly. When the droplet reaches a radius of 44 nm, corresponding to the encapsulated particle, shrinking stops and the dry particle heats up to room temperature. With the neutralization

chamber being entered at short time scales $< 10 \mu\text{s}$, it can be seen that the initially larger droplet has a larger size throughout passage. also, it spends longer time inside it. Putting this together, higher neutralization efficiency can be expected for larger droplets.

An alternative picture is the Maxwell model droplet evaporation, or “r-square law” [271]. Historically, droplets of diameter 1 mm were described. While the r-square law holds for large droplets, deviation from r-square-law for droplets $\leq 1 \mu\text{m}$ was described elsewhere [272] and behavior toward a linear r-law was observed [273]: even smaller droplets are described above.

One limitation which has not been considered yet is accounting for water molecule resorption in humid air: in principle, the water molecules existing in the gas phase collide with the droplet comparable to the gas molecules, thus effectively decreasing evaporative shrinking.

B. Further Details on Light-Scattering Imaging

B.1. Analysis of the Scattering Signal of cw-Illuminated Particles

For the charge-state characterization of 220 nm polystyrene spheres as shown in chapter 3, we deflected the aerosolized sample and modeled it with a particle trajectory simulation software framework (SIMION). One input for these simulations is the particle mass, which was defined corresponding to the nominal size distribution of monomeric particles. Close investigation of the scattered signal, however, revealed modulation of intensities. Here, their origin is discussed.

Detection of nanoparticles in the gas phase is key for characterization of nanoparticle beams, as we have used for instance during single-particle diffractive imaging (SPI) experiments. With the light-sheet imaging setup, see subsection 2.2.4, we produced a quasi-homogeneous narrow detection volume for these particles and could visualize cross sections through the particle beams at a defined distance from the injection device, i. e., the aerodynamic-lens stack (ALS). Variation of this distance allowed slicing through the particle beam and sampling of its three-dimensional volume [164]. By analyzing the recorded intensities, the species within the beam could be characterized.

The shown data set for the characterization of particle sizes is the same as described in chapter 3. The experimental methods can be found there in greater detail. As additional parameter, the continuous-wave (cw) laser was operated at average power of 3.5 W.

Taking the spatial distributions of the recorded 220 nm PS, compare Figure 3.2, in Figure B.1, the correlation between the position of the particles along the electric field and their scattering signal is shown as two-dimensional (2D) histograms.

The intensities in the undeflected particle beam, seen on the left, are modulated. The normalized histogram of intensities, seen on the left hand side of the figure in logarithmic scaling, has a prominent peak at 133 GV. At higher intensity values, peaks appear at multiples of 133 GV. Low statistics at even higher values don't allow clear identification of high order peaks. While deflecting the particles, which is shown on the right hand side, the fraction of blobs with $n \cdot 133$ GV ($n > 1$) decreases.

Intuitively, larger clusters of two or more particles are responsible for the brighter intensities. Investigating further, we modeled data to benchmark our blob finding software. The spatial distribution of the undeflected beam can in first approximation be considered 2D Gaussian, with a symmetric standard deviation of 16.5 μm . The amount of blobs per frame found in the experimental data is normally distributed: in each frame, 6.8 ± 2.0 blobs were detected. The noise of the image background was ± 2.3 GV. A "typical" blob was described by a point spread function with 1 pixel standard deviation. With these boundaries, and normalizing the artificial blobs' integrated signal to $133 \text{ GV} \pm 13 \text{ GV}$ to account for size variability, I created 10'000 artificial frames, mimicking the recorded data, including simulated hits. This

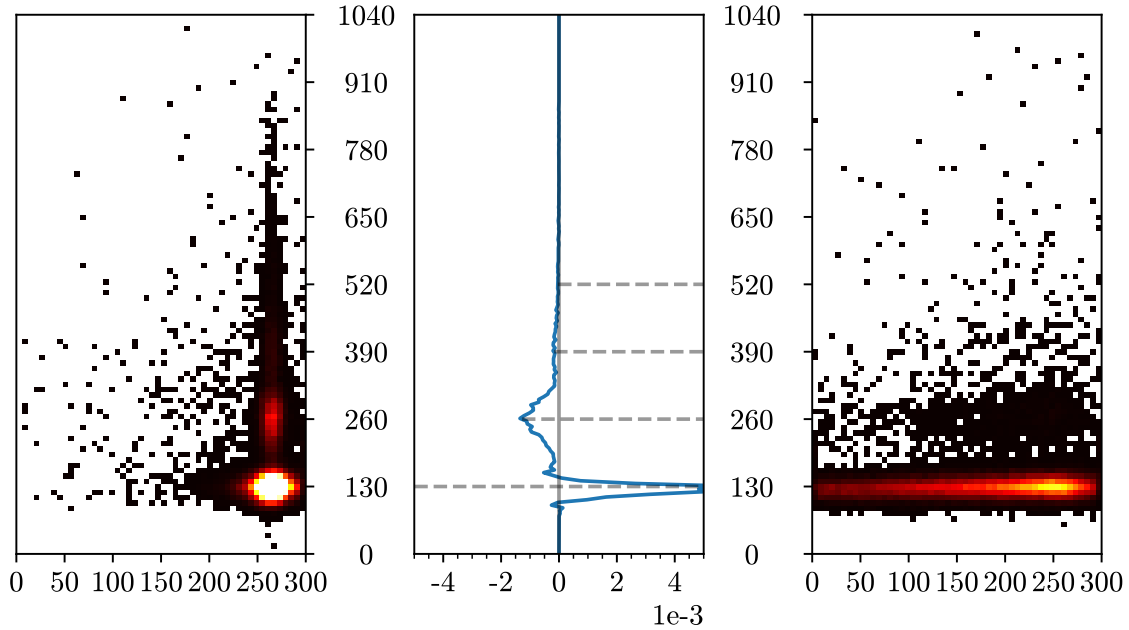


Figure B.1.: Recorded intensities in the light-sheet imaging setup. On the left, intensities are shown as a function of the undeflected beam. Periodic modulations of the intensity, at multiples of 130 gray values, can be observed. The same phenomenon can be observed in the deflected beam, but with fewer bright hits. In the middle panel, the difference between the two normalized histograms is shown: the deflected beam has more 130 gray value events, and the undeflected beam in relation more brighter ones.

simulated data was used as input for the blob finding script.

Using the same blob finding parameters for both the experimental and the simulated data, the analyzed blob intensity distributions for both data sets are compared in Figure B.2.

They show similarity in relative peak heights and their positions. After a closer investigation, the peaks at $n \cdot 133$ GV ($n > 1$) can be attributed to blobs being closer than their resolution limit, $d \leq 2\sigma_{\text{PSF}}$. With the camera shutter being open for 1 ms, this was the case when the particles had a close lateral distance, but different positions along the particle-beam axis. The camera integrated the signal during this time which led to a linear increase in signal strength. Considering the shown results, we could assume to produce mostly isolated 220 nm PS with our GDVN setup, and most of the blobs with brighter integrated scattering intensity came from particles being too close to resolve, as shown in fig. B.2. Comparing the areas between the first peak up to 190 GV and the rest, approximately 85% of the particles were resolved individually and 15% were assigned higher signal due to strongly overlapping point spread functions. The experimentally observed fraction of multiplets decreased when deflecting the particle beam, because the interparticle distance increased and with it the resolving ability of our imaging setup.

So, while a uniform light field allowed for direct scaling of intensities of detected particles of potentially different sizes, virtual large blobs introduced artifacts even for relatively low

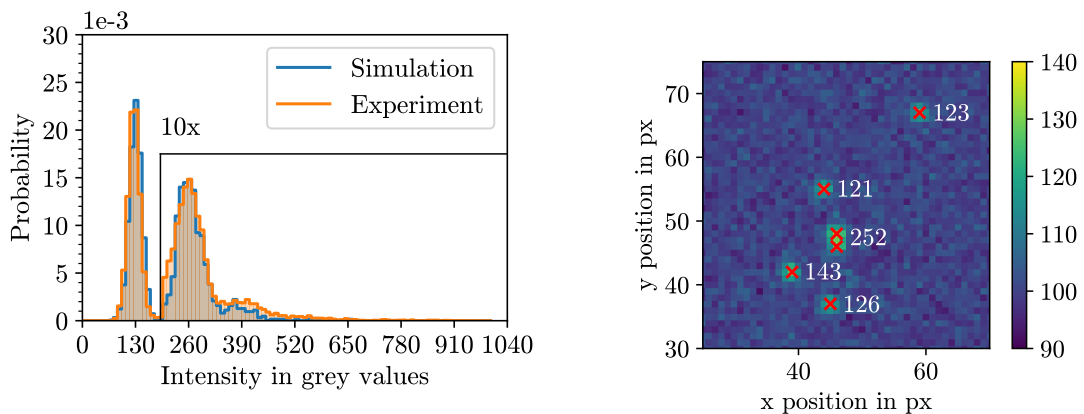


Figure B.2.: Intensities in light sheet setup

sample number concentrations of $< 8 \cdot 10^6$ compared to typical SPI experimental target values of $\approx 1 \cdot 10^{15}$. This phenomenon of double illumination was mitigated by using a pulsed laser, which stroboscopically illuminated the particle beam and virtually exclusively showed individual sample units. This allowed more rigorous and unambiguous analysis of individual particles and preparation of denser particle beams on the order of concentrations used during SPI experiments.

In conclusion, detection of particles with a light sheet yielded cross sections through the particle beams. Illuminating the particles with a cw light source resulted in scattering of an approximately constant signal from one particle size into our camera. In return, scattering signal could be easily put into relation, and relative intensity differences could be correlated to different particle species. Number density of particles for this setup has proven to produce “virtual” particles due to crossing the light sheet in close spatial proximity. Actual dimers, being two spheres stuck together, would on average have a square root of 2 increased effective diameter, and with this, approximately 1.4^6 times more scattering than their monomeric counterparts. With the probability of intensities dropping toward ≈ 950 GV, we can say we did not observe significant amounts of dimer in this sample.

B.2. Optical Aberration

Detecting nanoparticles in the above described side view imaging setup allows precise determination of their positions in the detector plane, but normally, not along the camera axis. This position ambiguity makes scattering signal evaluation problematic due to position ambiguity of the particles along the camera axis, i. e., across the laser.

A scan of the particle beam through the laser from $-150 \mu\text{m}$ before until $+150 \mu\text{m}$ behind the focal distance of the microscope, with the camera position being kept constant, revealed modulation of the observed blobs. Sets of visually “typical” blobs were selected from each position and data set, and then averaged to reduce noise. Then, these mean blobs were stacked with the open-source image processing software ImageJ, resulting in the hourglass

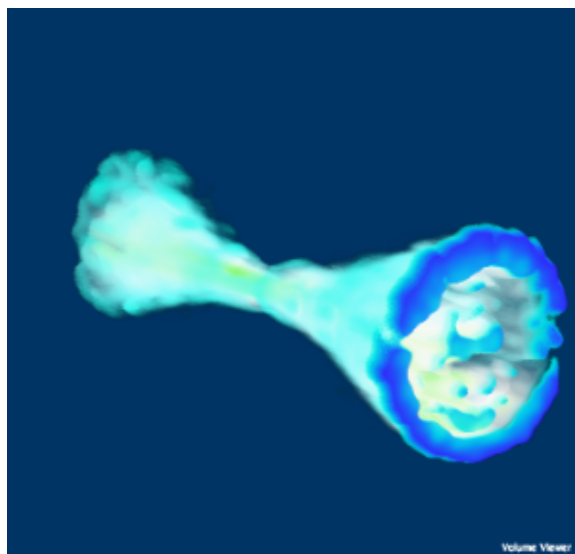


Figure B.3.: Optical aberration in the side-view imaging setup.

shape seen in Figure B.3. Between the focal point and the camera, the blobs had a cross section as shown, with a high-intensity ring and an intensity peak in the center, while for blob positions further than the focal point, the distribution was a “uniform” broad quasi-Gaussian blob. This effect comes from the optical aberration of the objective and may be, when better quantified, used for determining even the camera-axis position of the particles [274], potentially improving particle scattering and corresponding particle size analysis.

B.3. Particle Size Determination in the Side-View Imaging Setup

The spatially well-resolved deflected particle beams, for example shown in chapter 4 promise pure species present within them. But if two different sample molecules happened to have the same electric mobility, they would deflect similarly. With the above presented mass-to-charge deflection sample characterization we would not be able to resolve these species. As an example, we aerosolized two samples of polystyrene spheres with diameters 52 nm and 88 nm and characterized their scattering intensities. For 88 nm (a) and 52 nm(b), Figure B.4 shows the 2D histogram of the correlation of scattering intensities and the positions of the particles across the laser, which was pointed at the particle beam at 190 μm . Therefore, this was the region where the highest intensities were recorded. The particles propagated from larger x axis values to the left. toward the injector, i. e., at higher y values, a decrease in intensity in a wavy pattern can be explained by multiple reflections of the laser within the two in- and outlet windows, which acted in this case as weaker superpositions to the original laser field. The two single species, 50 nm PS and 88 nm PS, show similar relative distribution of intensities across the laser, but scaled due to their significantly different sizes. Especially the

88 nm sample had a clear band of signal, corresponding to its rather narrow size distribution.

Then, we injected a mixture of the two species, 52 nm and 88 nm PS, and analyzed the intensities against the hits' positions across the laser, which is shown in Figure B.4 c). As expected, the same intensity bands could be observed as in the individually investigated species before. Having identified signal bands of quasi-unambiguous size attribution, I deflected the mixed sample as described for example in chapter 4. Initially, a broadly dispersed particle beam could be observed, but with spatial correlation, the recorded intensities could now be used to disentangle the overlapping intensity histograms and assign regions where pure particle species could be found. The result is shown in Figure B.5: even with overlapping spatial distributions of the molecules, for example at 350 μm along the field, an 80% pure beam of neutral 88 nm PS can be identified, or a 80-95% pure region of 52 nm PS in the deflected beam between field coordinates 200 μm –300 μm .

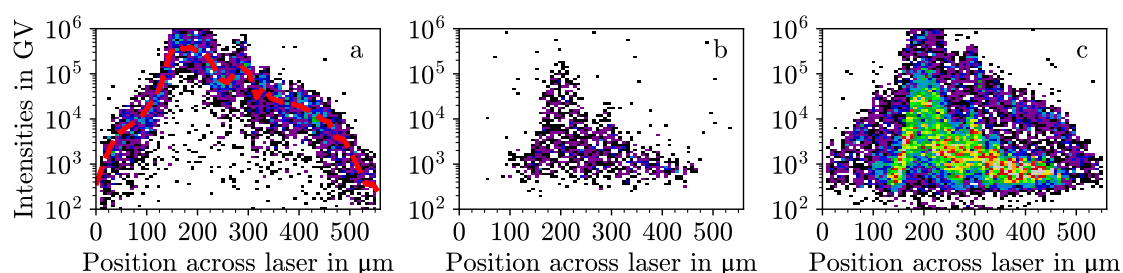


Figure B.4.: The measured intensities of 52 nm and 88 nm PS as a function of their position across the detection laser are shown as 2D histograms. (a): The intensities distribution of 88 nm PS across the detection laser shows a distinct band in the logarithmic representation. The band width can be attributed to variation in particle size, while the modulation across the laser is correlated the mean local laser intensity. As a red dashed line, the median intensity as a function of x is shown, which qualitatively represents the laser profile. (b): The intensity distribution of 52 nm PS sample. In comparison with (a), the intensities as a function of position are lower all across the laser. (c): The intensity distribution of mixed sample. Both individual modulations from (a) and (b) can be found.

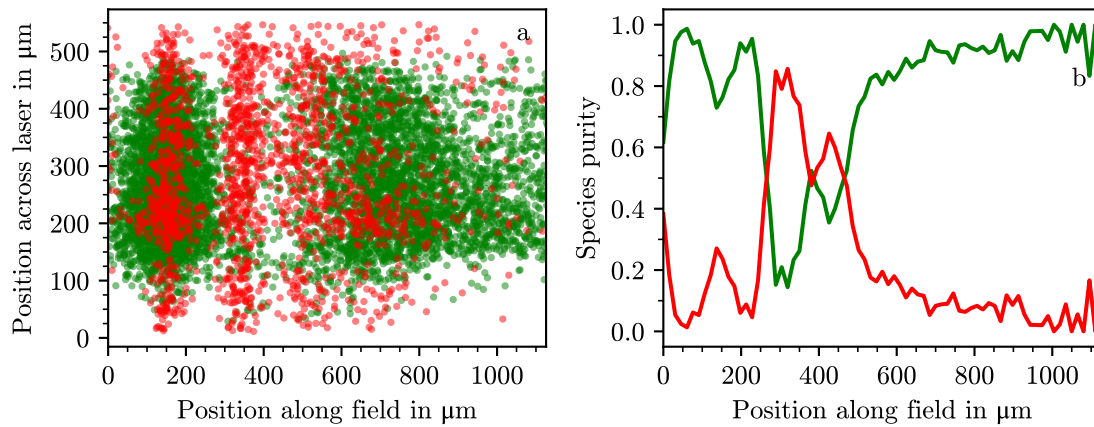


Figure B.5.: (a): Deflection of a particle beam of mixed PS sample was imaged in a side view imaging setup. The singly charged 52 nm and doubly charged 88 nm particles had similar mobilities in the applied field, which resulted in partly overlapping beams. Taking the laser profile, shown in Figure B.4 (a): red dashed line, the measured intensities could be normalized and disentangled. The clearly revealed the 88 nm (red) and 52 nm (green) PS, even in regions of spatial overlap. (b): Projection onto the x axis reveals the species purity at different x positions. For example, at $x = 325 \mu\text{m}$, singly charged 88 nm particles can be found at purity $>80\%$. At $x = 225 \mu\text{m}$, neutral 52 nm particles can be found with $>90\%$ probability. In the center of the beam of neutral particles, at $x = 150 \mu\text{m}$, 52 nm and 88 nm particles can be found with a ratio of approximately 7:3.

Publications

- [217] **J. Lübke**, N. Roth, L. Worbs, D. A. Horke, A. D. Estillore, A. K. Samanta, and J. Küpper. *J. Phys. Chem. C* **125**, 25794 (2021).
- [275] **J. Lübke**, P. L. Xavier, L. Worbs, H. N. Chapman, A. K. Samanta, and J. Küpper. *In preparation*.
- [161] L. Worbs, **J. Lübke**, A. D. Estillore, A. K. Samanta, and J. Küpper. *In preparation*.
- [164] L. Worbs, **J. Lübke**, N. Roth, A. K. Samanta, D. A. Horke, and J. Küpper. *Opt. Exp.* **25**, 36580 (2019).
- [159] N. Roth, D. Horke, **J. Lübke**, A. K. Samanta, A. D. Estillore, L. Worbs, N. Pohlman, K. Ayyer, A. Morgan, H. Fleckenstein, M. Domaracky, B. Erk, C. Passow, J. Correa, O. Yefanov, A. Barty, M. Prasciolu, S. Bajt, R. Kirian, H. N. Chapman, and J. Küpper. arXiv: 2012.11237. *In preparation*.
- [163] L. Worbs, N. Roth, **J. Lübke**, A. D. Estillore, P. L. Xavier, A. K. Samanta, and J. Küpper. *J. Appl. Cryst.* **54**, 1730 (2021).
- [76] Y. Zhuang, S. Awel, A. Barty, R. Bean, J. Bielecki, M. Bergemann, B. J. Daurer, T. Ekeberg, A. D. Estillore, H. Fangohr, K. Giewekemeyer, M. S. Hunter, M. Karnevskiy, R. A. Kirian, H. Kirkwood, Y. Kim, J. Koliyadu, H. Lange, R. Letrun, **J. Lübke**, A. Mall, T. Michelat, A. J. Morgan, N. Roth, A. K. Samanta, T. Sato, Z. Shen, M. Sikorski, F. Schulz, J. C. H. Spence, P. Vagovic, T. Wollweber, L. Worbs, P. L. Xavier, O. Yefanov, F. R. N. C. Maia, D. A. Horke, J. Küpper, N. D. Loh, A. P. Mancuso, H. N. Chapman, and K. Ayyer. *IUCrJ* **9**, 204 (2022).
- [80] T. Ekeberg, D. Assalauova, J. Bielecki, R. Boll, B. J. Daurer, L. A. Eichacker, L. E. Franken, D. E. Galli, L. Gelisio, L. Gumprecht, L. H. and Gunn, J. Hajdu, R. Hartmann, D. Hasse, A. Ignatenko, J. Koliyadu, O. Kulyk, R. Kurta, M. Kuster, W. Lugmayr, **J. Lübke**, A. P. Mancuso, T. Mazza, C. Nettelblad, Y. Ovcharenko, D. E. Rivas, M. Rose, A. K. Samanta, P. Schmidt, E. Sobolev, N. Timneanu, S. Usenko, D. Westphal, T. Wollweber, L. Worbs, L. P. Xavier, H. Yousef, K. Ayyer, H. N. Chapman, J. A. Sellberg, C. Seuring, I. A. Vartanyants, J. Küpper, M. Meyer, and F. R. N. C. Maia. *Submitted* (2022).
- [81] K. Ayyer, P. L. Xavier, J. Bielecki, Z. Shen, B. J. Daurer, A. K. Samanta, S. Awel, R. Bean, A. Barty, M. Bergemann, T. Ekeberg, A. D. Estillore, H. Fangohr, K. Giewekemeyer, M. S. Hunter, M. Karnevskiy, R. A. Kirian, H. Kirkwood, Y. Kim, J. Koliyadu, H. Lange, R. Letrun, **J. Lübke**, T. Michelat, A. J. Morgan, N. Roth, T. Sato, M. Sikorski, F. Schulz, J. C. H. Spence, P. Vagovic, T. Wollweber, L. Worbs, O. Yefanov, Y. Zhuang, F. R. N. C. Maia, D. A. Horke, J. Küpper, N. D. Loh, A. P. Manusco, H. N. Chapman. *Optica* **8**, 15 (2021).

- [82] D. Höing, R. Salzwedel, L. Worbs, Y. Zhuang, A. K. Samanta, **J. Lübke**, A. D. Estillore, K. Dlugolecki, C. Passow, B. Erk, N. Ekanayake, D. Ramm, J. Correa, C. C. Papadopoulou, A. T. Noor, F. Schulz, M. Selig, A. Knorr, K. Ayyer, J. Küpper, and H. Lange. *Submitted* (2022).

Beamtimes with Active Participation

2018/04/30–2018/05/07	FLASH	Aerosol-SPI
2018/08/16–2018/08/27	FLASH	Laser desorption of dipeptide conformers
2019/05/23–2019/05/26	EuXFEL(SPB)	#2145: High-resolution Flash X-ray Imaging of Melbourne Virus at MHz Rates
2019/05/29–2019/06/03	EuXFEL(SPB)	#2160: Single-Particle Imaging: The Million-pattern Gold Standard
2019/07/24–2019/07/29	EuXFEL(SQS)	#2146: Flash X-ray Imaging of Single Proteins
2019/08/14–2019/08/19	EuXFEL(SQS)	#2370: Element-Specific Diffractive Imaging of Bimetallic Nanoparticles
2019/08/21–2019/08/25	EuXFEL(SQS)	#2322: Single-Particle Diffractive Imaging of 3D DNA-Origami
2019/10/24–2019/10/28	EuXFEL(SPB)	#2316: Nanofocus Flash-x-ray Imaging of Ribosomes
2020/08/11–2020/08/17	FLASH	Recording Structural Dynamics for the Direct Imaging of Energy Dissipation in Single Nanocrystals
2021/08/10–2021/08/15	EuXFEL(SQS)	#2601: High-repetition Rate 3D X-ray Imaging of Single Proteins
2021/11/04–2021/11/07	EuXFEL(SPB)	#2746: Perovskite Quantum Dot Lattice Dynamics
2022/03/31–2022/04/03	EuXFEL(SPB)	#2734: Holographic Single-Particle Imaging

Acknowledgments

Even though it is only my name on the first page of this work, many more have helped me to get to this point, and I want to thank them all wholeheartedly.

My doctoral journey began with Jochen Küpper granting me a place within the COMOTION team in the Controlled Molecule Imaging group. Thank you for lively discussions and valuable critique, for pushing me to (and even beyond) the limit, and for being my supervisor for this work.

Thank you, Barbora Vagovič, for effectively and friendly helping through all administrative issues. Without you, I'd probably still be stuck filling out matriculation paperwork. The somewhat turbulent admission process and the associated exams posed a challenge in themselves. Elena Kireva, thank you for easing my mind in that regard. It was very helpful having you as an optimistic and constructive contact person for these issues.

A big thank you goes out to all my present and former colleagues. Be it during group outings, scientific discussions, in the office, online, or at the Christmas market, it was fun having you around and talking to you. Nils Roth, I am glad it was you who I learned the ropes from. One of my definite highlights was playing cards with you during beam-downtimes in the middle of the night. Thank you, Amit Samanta, for your support, for always having an open ear, putting things into perspective, and for being our team leader. Lena Worbs, I am glad we shared this time. Thank you for very helpful discussions, scientific or not, for laughs, letting off steam, and helping survive looong days in the lab together. And Armando, thank you for never stopping to ask questions, appropriate or not.

From thinking outside the box, to really taking an interest in my progress, to keeping me motivated: Arwen Pearson, thank you for your ongoing mentoring efforts.

Of course, I also want to thank DESY, the University of Hamburg, and the cluster of excellence CUI: Advanced Imaging of Matter for funding throughout my work and for general support.

Finally, a big thank you goes to everybody keeping my spirits up in times of pressure. To my family, in particular Moritz and my parents, and to my friends: your understanding, distractions, and maintaining contact during hermit-like work phases were and are invaluable to me. Anna, thank you for being there, for endless support, love, and making our home a home. Having you by my side really helped, especially during this final stretch.

Bibliography

- [1] C. Kidd and B. Y. Hayden, *Neuron* **88**, 449 (2015). DOI: 10.1016/j.neuron.2015.09.010.
- [2] E. O. Wilson, *Consilience : the unity of knowledge* (Vintage Books/ Random House, New York, U.S.A., 1999), ISBN 978-0307292049.
- [3] M. Saha and A. Sarkar, *J. Xenobiot.* **11**, 197 (2021). DOI: 10.3390/jox11040013.
- [4] G. D. Wright, *BMC Biol.* **8**, 123 (2010). DOI: 10.1186/1741-7007-8-123.
- [5] R. Vivas, A. A. T. Barbosa, S. S. Dolabela, and S. Jain, *Microb. Drug Resist.* **25**, 890 (2019). DOI: 10.1089/mdr.2018.0319.
- [6] H. Nikaido, *Annu. Rev. Biochem.* **78**, 119 (2009). DOI: 10.1146/annurev.biochem.78.082907.145923.
- [7] B. G. Spratt, *Science* **264**, 388 (1994). DOI: 10.1126/science.8153626.
- [8] M. S. H. Akash, K. Rehman, M. Tariq, and S. Chen, *Turk. J. Biol.* **39**, 343 (2015). DOI: 10.3906/biy-1411-8.
- [9] B. Kuhlman and P. Bradley, *Nat. Rev. Mol. Cell Biol.* **20**, 681 (2019). DOI: 10.1038/s41580-019-0163-x.
- [10] G. Upert, A. Luther, D. Obrecht, and P. Ermert, *Med. Drug Discov.* **9**, 100078 (2021). DOI: 10.1016/j.medidd.2020.100078.
- [11] A. L. Parrill and M. R. Reddy, eds., *Rational Drug Design - Novel Methodology and Practical Applications*, ACS Symposium Series, vol 719 (Am. Chem. Soc., Washington DC, U.S.A., 1999), ISBN 9780841236035. DOI: 10.1021/bk-1999-0719.
- [12] J. Zhou, A. E. Panaitiu, and G. Grigoryan, *PNAS* **117**, 1059 (2019). DOI: 10.1073/pnas.1908723117.
- [13] M. Batool, B. Ahmad, and S. Choi, *Int. J. Mol. Sci.* **20**, 2783 (2019). DOI: 10.3390/ijms20112783.
- [14] C. D. Fjell, J. A. Hiss, R. E. W. Hancock, and G. Schneider, *Nat. Rev. Drug Discov.* **11**, 37 (2012). DOI: 10.1038/nrd3591.
- [15] S. Agnihotry, R. K. Pathak, D. B. Singh, A. Tiwari, and I. Hussain, *Protein structure prediction* (Adv. Phys., London, UK, 2022), pp. 177–188, ISBN 9780323897754, URL <https://10.1016/B978-0-323-89775-4.00023-7>.
- [16] R. P. Feynman, *Feynman and Computation: Exploring the Limits of Computers* (CRC Press, Boca Raton, U.S.A., 2002), 1st ed., ISBN 9780429500459. DOI: 10.1201/9780429500459.

- [17] E. Abbe, Arch. Mikrosk. Anat. **9**, 413 (1873). DOI: 10.1007/BF02956173.
- [18] L. Chen, J. He, S. Sazzed, and R. Walker, Molecules **23**, 610 (2018). DOI: 10.3390/molecules23030610.
- [19] Z. H. Zhou, Curr. Opin. Struct. Biol. **18**, 218 (2008). DOI: 10.1016/j.sbi.2008.03.004.
- [20] H. M. Berman, Acta Cryst. A **64**, 88 (2008). DOI: 10.1107/S0108767307035623.
- [21] W. Friedrich, P. Knipping, and M. Laue, Ann. Phys. **346**, 971 (1913).
- [22] H. A. Hauptman, Struct. Chem. **1**, 617 (1990). DOI: 10.1007/bf00674136.
- [23] A. M. Glazer, *Crystallography: A Very Short Introduction* (Oxford University Press, Oxford, UK, 2016), 1st ed., ISBN 978-0-19-871759-1. DOI: 10.1093/ac-trade/9780198717591.001.0001.
- [24] M. S. Smyth and J. H. J. Martin, Mol. Pathol. **53**, 8 (2000). DOI: 10.1136/mp.53.1.8.
- [25] F. L. Hünefeld, *Der Chemismus in der thierischen Organisation* (F. A. Brockhaus, Leipzig, Germany, 1840), ISBN 9781318558421.
- [26] M. P. Blakeley, S. S. Hasnain, and S. V. Antonyuk, IUCrJ **2**, 464 (2015). DOI: 10.1107/S2052252515011239.
- [27] R.E. Franklin, R.G. Gosling, Nature **171**, 740 (1953). DOI: 10.1038/171740a0.
- [28] H. Hope, F. Frolow, K. von Böhlen, I. Makowski, C. Kratky, Y. Halfon, H. Danz, P. Webster, K. S. Bartles, H. G. Wittmann, and A. Yonath, Acta Cryst. B **45**, 190 (1989). DOI: 10.1107/S0108768188013710.
- [29] A. R. Pearson and P. Mehrabi, Curr. Opin. Struct. Biol. **65**, 168 (2020). DOI: 10.1016/j.sbi.2020.06.019.
- [30] S. Günther, P. Y. A. Reinke, Y. Fernández-García, J. Lieske, T. J. Lane, H. M. Ginn, F. H. M. Koua, C. Ehrt, W. Ewert, D. Oberthuer, O. Yefanov, S. Meier, K. Lorenzen, B. Krichel, J.-D. Kopicki, L. Gelisio, W. Brehm, I. Dunkel, B. Seychell, H. Gieseler, B. Norton-Baker, B. Escudero-Pérez, M. Domaracky, S. Saouane, A. Tolstikova, T. A. White, A. Hänle, M. Groessler, H. Fleckenstein, F. Trost, M. Galchenkova, Y. Gevorkov, C. Li, S. Awel, A. Peck, M. Barthelmess, F. Schlünzen, P. L. Xavier, N. Werner, H. Andaleeb, N. Ullah, S. Falke, V. Srinivasan, B. A. França, M. Schwinzer, H. Brognaro, C. Rogers, D. Melo, J. J. Zaitseva-Doyle, J. Knoska, G. E. Peña-Murillo, A. R. Mashhour, V. Hennicke, P. Fischer, J. Hakanpää, J. Meyer, P. Gribbon, B. Ellinger, M. Kuzikov, M. Wolf, A. R. Beccari, G. Bourenkov, D. von Stetten, G. Pompidor, I. Bento, S. Panneerselvam, I. Karpics, T. R. Schneider, M. M. Garcia-Alai, S. Niebling, C. Günther, C. Schmidt, R. Schubert, H. Han, J. Boger, D. C. F. Monteiro, L. Zhang, X. Sun, J. Pletzer-Zelgert, J. Wollenhaupt, C. G. Feiler, M. S. Weiss, E.-C. Schulz, P. Mehrabi, K. Karničar, A. Usenik, J. Loboda, H. Tidow, A. Chari, R. Hilgenfeld,

-
- C. Uetrecht, R. Cox, A. Zaliani, T. Beck, M. Rarey, S. Günther, D. Turk, W. Hinrichs, H. N. Chapman, A. R. Pearson, C. Betzel, and A. Meents, *Science* **372**, 642 (2021). DOI: 10.1126/science.abf7945.
- [31] S. Pandey, R. Bean, T. Sato, I. Poudyal, J. Bielecki, J. C. Villarreal, O. Yefanov, V. Mariani, T. A. White, C. Kupitz, M. Hunter, M. H. Abdellatif, S. Bajt, V. Bondar, A. Echelmeier, D. Doppler, M. Emons, M. Frank, R. Fromme, Y. Gevorkov, G. Giovanetti, M. Jiang, D. Kim, Y. Kim, H. Kirkwood, A. Klimovskaia, J. Knoska, F. H. M. Koua, R. Letrun, S. Lisova, L. Maia, V. Mazalova, D. Meza, T. Michelat, A. Ourmazd, G. Palmer, M. Ramilli, R. Schubert, P. Schwander, A. Silenzi, J. Sztuk-Dambietz, A. Tolstikova, H. N. Chapman, A. Ros, A. Barty, P. Fromme, A. P. Mancuso, and M. Schmidt, *Nat. Methods* **17**, 73 (2019). DOI: 10.1038/s41592-019-0628-z.
- [32] Z. Dauter, *Acta Cryst. D* **62**, 1 (2006). DOI: 10.1107/S0907444905034050.
- [33] P. E. Konold, E. Arik, J. Weißenborn, J. C. Arents, K. J. Hellingwerf, I. H. M. van Stokkum, J. T. M. Kennis, and M. L. Groot, *Nat. Commun.* **11**, 4248 (2020). DOI: 10.1038/s41467-020-18065-9.
- [34] E. Eyal, S. Gerzon, V. Potapov, M. Edelman, and V. Sobolev, *J. Mol. Biol.* **351**, 431 (2005). DOI: 10.1016/j.jmb.2005.05.066.
- [35] C. S. Rapp and R. M. Pollack, *Proteins* **60**, 103 (2005). DOI: 10.1002/prot.20492.
- [36] E. Callaway, *Nature* **578**, 201 (2020). DOI: 10.1038/d41586-020-00341-9.
- [37] K. M. Yip, N. Fischer, E. Paknia, A. Chari, and H. Stark, *Nature* **587**, 157 (2020). DOI: 10.1038/s41586-020-2833-4.
- [38] E. G. Berg, *ACS Cent. Sci.* **1**, 283 (2015). DOI: 10.1021/acscentsci.5b00295.
- [39] Y. Cheng, N. Grigorieff, P. A. Penczek, and T. Walz, *Cell* **161**, 438 (2016). DOI: 10.1016/j.cell.2015.03.050.
- [40] Y. Cheng, *Science* **361**, 876 (2018). DOI: 10.1126/science.aat4346.
- [41] E. D’Imprima and W. Kühlbrandt, *Q. Rev. Biophys.* **54**, 1 (2021). DOI: 10.1017/S0033583521000020.
- [42] D. Adams, *The hitchhiker’s guide to the galaxy* (Harmony Books, New York, U.S.A., 1979), ISBN 978-0307292049.
- [43] D. Lyumkis, *J. Biol. Chem.* **294**, 5181 (2019). DOI: 10.1074/jbc.REV118.005602.
- [44] T. Jain, P. Sheehan, J. Crum, B. Carragher, and C. S. Potter, *J. Struct. Biol.* **179**, 68 (2007). DOI: 10.1016/j.jsb.2012.04.020.
- [45] M. Wu and G. C. Lander, *Biophys. J.* **119**, 1281 (2020). DOI: 10.1016/j.bpj.2020.08.027.

- [46] I. I. Rabi, J. R. Zacharias, S. Millman, and P. Kusch, *Phys. Rev.* **53**, 318 (1938). DOI: 10.1103/PhysRev.53.318.
- [47] H. Günther, *NMR Spectroscopy: Basic Principles, Concepts, and Applications in Chemistry* (Wiley-VCH, Weinheim, Germany, 2013), 3rd ed., ISBN 978-3-527-33004-1.
- [48] P. R. L. Markwick, T. Malliavin, and M. Nilges, *PLoS Comput. Biol.* **4**, e1000168 (2008). DOI: 10.1371/journal.pcbi.1000168.
- [49] J. C. Chatham and S. J. Blackband, *ILAR J.* **42**, 189 (2001). DOI: 10.1093/ilar.42.3.189.
- [50] K. Pervushin, R. Riek, G. Wider, and K. Wüthrich, *PNAS* **94**, 12366 (1997). DOI: 10.1073/pnas.94.23.12366.
- [51] M. A. Markus, K. T. Dayie, P. Matsudaira, and G. Wagner, *J. Magn. Reson. B* **105**, 189 (1994). DOI: 10.1006/jmrb.1994.1122.
- [52] J. Fiaux, E. B. Bertelsen, H. A. L., and K. Wüthrich, *Nature* **418**, 207 (2002). DOI: 10.1038/nature00860.
- [53] RCSB PDB, *PDB statistics: Protein-only structures released per year*, <https://www.rcsb.org/stats/growth/growth-protein> (2022), accessed: 2022-09-12.
- [54] H. M. Berman, J. Westbrook, Z. Feng, G. Gilliland, T. N. Bhat, H. Weissig, I. N. Shindyalov, and P. E. Bourne, *Nucleic Acids Research* **28**, 235 (2000). DOI: 10.1093/nar/28.1.235.
- [55] J. Jumper, R. Evans, A. Pritzel, T. Green, M. Figurnov, O. Ronneberger, K. Tunyasuvunakool, R. Bates, A. Žídek, A. Potapenko, A. Bridgland, C. Meyer, S. A. A. Kohl, A. J. Ballard, A. Cowie, B. Romera-Paredes, S. Nikolov, R. Jain, J. Adler, T. Back, S. Petersen, D. Reiman, E. Clancy, M. Zielinski, M. Steinegger, M. Pacholska, T. Berghammer, S. Bodenstein, D. Silver, O. Vinyals, A. W. Senior, K. Kavukcuoglu, P. Kohli, and D. Hassabis, *Nature* **596**, 583 (2021). DOI: 10.1038/s41586-021-03819-2.
- [56] A. B. Tong, J. D. Burch, D. McKay, C. Bustamante, M. A. Crackower, and H. Wu, *Nat. Struct. Mol. Biol.* **28**, 771 (2021). DOI: 10.1038/s41594-021-00670-x.
- [57] K. Heyne, *J. Phys. Chem. B* **126**, 581 (2022). DOI: 10.1021/acs.jpcc.1c08131.
- [58] Z. Pasternak, N. Chapnik, R. Yosef, N. M. Kopelman, E. Jurkevitch, and E. Segev, *PLoS One* **17**, e0264765 (2022). DOI: 10.1371/journal.pone.0264765.
- [59] G. P. Lisi, I. Rivalta, and V. Venditti, *Front. Mol. Biosci.* **9**, 876499 (2022). DOI: 10.3389/fmolb.2022.876499.
- [60] L. C. Xue, D. Dobbs, A. M. Bonvin, and V. Honavar, *FEBS Lett.* **589**, 3516 (2015). DOI: 10.1016/j.febslet.2015.10.003.

-
- [61] A. Cousido-Siah, T. Petrova, I. Hazemann, A. Mitschler, F. X. Ruiz, E. Howard, S. Ginell, C. Atmanene, A. van Dorsselaer, S. Sanglier-Cianf erani, A. Joachimiak, and A. Podjarny, *Proteins* **80**, 2552 (2012). DOI: 10.1002/prot.24136.
- [62] H. N. Chapman, A. Barty, M. J. Bogan, S. Boutet, S. Frank, S. P. Hau-Riege, S. Marchesini, B. W. Woods, S. Bajt, W. H. Benner, L. W. A., E. Pl onjes, M. Kuhlmann, R. Treusch, S. D usterer, T. Tschentscher, J. R. Schneider, E. Spiller, T. M oller, C. Bostedt, M. Hoener, D. A. Shapiro, K. O. Hodgson, D. van der Spoel, F. Burmeister, M. Bergh, C. Caleman, G. Huldt, M. M. Seibert, F. R. N. C. Maia, R. W. Lee, A. Sz oke, N. Timneanu, and J. Hajdu, *Nat. Phys.* **2**, 839 (2006). DOI: 10.1038/nphys461.
- [63] K. J. Gaffney and H. N. Chapman, *Science* **316**, 1444 (2007). DOI: 10.1126/science.1135923.
- [64] C. Pellegrini, A. Marinelli, and S. Reiche, *Rev. Mod. Phys.* **88**, 015006 (2016). DOI: 10.1103/RevModPhys.88.015006.
- [65] W. Decking, S. Abeghyan, P. Abramian, A. Abramsky, A. Aguirre, C. Albrecht, P. Alou, M. Altarelli, P. Altmann, K. Amyan, V. Anashin, E. Apostolov, K. Appel, D. Auguste, V. Ayvazyan, S. Baark, F. Babies, N. Baboi, P. Bak, V. Balandin, R. Baldinger, B. Baranasic, S. Barbanotti, O. Belikov, V. Belokurov, L. Belova, V. Belyakov, S. Berry, M. Bertucci, B. Beutner, A. Block, M. Bl ocher, T. B ockmann, C. Bohm, M. B ohnert, V. Bondar, E. Bondarchuk, M. Bonezzi, P. Borowiec, C. B osch, U. B osenberg, A. Bosotti, R. B ospflug, M. Bousonville, E. Boyd, Y. Bozhko, A. Brand, J. Brandler, S. Briechele, F. Brinker, S. Brinker, R. Brinkmann, S. Brockhauser, O. Brovko, H. Br uck, A. Br udgam, L. Butkowski, T. B uttner, J. Calero, E. Castro-Carballo, G. Cattalanotto, J. Charrier, J. Chen, A. Cherepenko, V. Cheskidov, M. Chiodini, A. Chong, S. Choroba, M. Chorowski, D. Churanov, W. Cichalewski, M. Clausen, W. Clement, C. Clou e, J. A. Cobos, N. Coppola, S. Cunis, K. Czuba, M. Czwalinna, B. D’Almagne, J. Dammann, H. Danared, A. de Zubiurre Wagner, A. Delfs, T. Delfs, F. Dietrich, T. Dietrich, M. Dohlus, M. Dommach, A. Donat, X. Dong, N. Doynikov, M. Dressel, M. Duda, P. Duda, H. Eckoldt, W. Ehsan, J. Eidam, F. Eints, C. Engling, U. Englisch, A. Ermakov, K. Escherich, J. Eschke, E. Saldin, M. Faesing, A. Fallou, M. Felber, M. Fenner, B. Fernandes, J. M. Fern andez, S. Feuker, K. Filippakopoulos, K. Floettmann, V. Fogel, M. Fontaine, A. Franc es, I. F. Martin, W. Freund, T. Freyermuth, M. Friedland, L. Fr ohlich, M. Fusetti, J. Fydrych, A. Gallas, O. Garc ia, L. Garcia-Tabares, G. Geloni, N. Gerasimova, C. Gerth, P. Ge feler, V. Gharibyan, M. Gloor, J. G lowinkowski, A. Goessel, Z. Go lebiewski, N. Golubeva, W. Grabowski, W. Graeff, A. Grebentsov, M. Grecki, T. Grevsmuehl, M. Gross, U. Grosse-Wortmann, J. Gr unert, S. Grunewald, P. Grzegory, G. Feng, H. Guler, G. Gusev, J. L. Gutierrez, L. Hagge, M. Hamberg, R. Hanneken, E. Harms, I. Hartl, A. Hauberg, S. Hauf, J. Hauschildt, J. Hauser, J. Havlicek, A. Hedqvist, N. Heidbrook, F. Hellberg, D. Henning, O. Hensler, T. Hermann, A. Hidv egi, M. Hierholzer, H. Hintz, F. Hoffmann, M. Hoffmann, M. Hoffmann, Y. Holler, M. H uning, A. Ignatenko, M. Ilchen, A. Iluk, J. Iversen, M. Izquierdo, L. Jachmann, N. Jardon, U. Jastrow, K. Jensch, J. Jensen,

- M. Jeżabek, M. Jidda, H. Jin, N. Johansson, R. Jonas, W. Kaabi, D. Kaefer, R. Kammering, H. Kapitza, S. Karabekyan, S. Karstensen, K. Kasprzak, V. Katalev, D. Keese, B. Keil, M. Kholopov, M. Killenberger, B. Kitaev, Y. Klimchenko, R. Klos, L. Knebel, A. Koch, M. Koepke, S. Köhler, W. Köhler, N. Kohlstrunk, Z. Konopkova, A. Konstantinov, W. Kook, W. Koprek, M. Körfer, O. Korth, A. Kosarev, K. Kosiński, D. Kostin, Y. Kot, A. Kotarba, T. Kozak, V. Kozak, R. Kramert, M. Krasilnikov, A. Krasnov, B. Krause, L. Kravchuk, O. Krebs, R. Kretschmer, J. Kreutzkamp, O. Kröplin, K. Krzysik, G. Kube, H. Kuehn, N. Kujala, V. Kulikov, V. Kuzminych, D. La Civita, M. Lacroix, T. Lamb, A. Lancetov, M. Larsson, D. Le Pinvidic, S. Lederer, T. Lensch, D. Lenz, A. Leuschner, F. Levenhagen, Y. Li, J. Liebing, L. Lilje, T. Limberg, D. Lipka, B. List, J. Liu, S. Liu, B. Lorbeer, J. Lorkiewicz, H. H. Lu, F. Ludwig, K. Machau, W. Maciocha, C. Madec, C. Magueur, C. Maiano, I. Maksimova, K. Malcher, T. Maltezopoulos, E. Mamoshkina, B. Manschwetus, F. Marcellini, G. Marinkovic, T. Martinez, H. Martirosyan, W. Maschmann, M. Maslov, A. Matheisen, U. Mavric, J. Meißner, K. Meissner, M. Messerschmidt, N. Meyners, G. Michalski, P. Michelato, N. Mildner, M. Moe, F. Moglia, C. Mohr, S. Mohr, W. Möller, M. Mommerz, L. Monaco, C. Montiel, M. Moretti, I. Morozov, P. Morozov, and D. Mross, *Nat. Photon.* **14**, 391 (2020). DOI: 10.1038/s41566-020-0607-z.
- [66] A. P. Mancuso, A. Aquila, L. Batchelor, R. J. Bean, J. Bielecki, G. Borchers, K. Doerner, K. Giewekemeyer, R. Graceffa, O. D. Kelsey, Y. Kim, H. J. Kirkwood, A. Legrand, R. Letrun, B. Manning, L. L. Morillo, M. Messerschmidt, G. Mills, S. Raabe, N. Reimers, A. Round, T. Sato, J. Schulz, C. S. Takem, M. Sikorski, S. Stern, P. Thute, P. Vagovic, B. Weinhausena, and T. Tschentschera, *J. Synchrotron Rad.* **26**, 660 (2019). DOI: 10.1107/S1600577519003308.
- [67] R. Neutze, R. Wouts, D. van der Spoel, E. Weckert, and J. Hajdu, *Nature* **406**, 752 (2000). DOI: 10.1038/35021099.
- [68] J. Bielecki, F. R. N. C. Maia, and A. P. Mancuso, *Structural Dynamics* **7**, 040901 (2020). DOI: 10.1063/4.0000024.
- [69] H. N. Chapman, C. Caleman, and N. Timneanu, *Phil. Trans. R. Soc. B* **369**, 20130313 (2014). DOI: 10.1098/rstb.2013.0313.
- [70] B. von Ardenne and H. Grubmüller, *Single Particle Imaging with FEL Using Photon Correlations* (Springer Nature, Cham, Switzerland, 2021), pp. 435–452, ISBN 978-3-030-34413-9, URL <https://doi.org/10.1007/978-3-030-34413-9>.
- [71] I. Poudyal, M. Schmidt, and P. Schwander, *Structural Dynamics* **7**, 024102 (2020). DOI: 10.1063/1.5144516.
- [72] N.-T. D. Loh and V. Elser, *Phys. Rev. E* **80**, 026705 (2009). DOI: 10.1103/PhysRevE.80.026705.
- [73] N. D. Loh, M. J. Bogan, V. Elser, A. Barty, S. Boutet, S. Bajt, J. Hajdu, T. Ekeberg, F. R. N. C. Maia, J. Schulz, M. M. Seibert, B. Iwan, N. Timneanu, S. Marchesini,

- I. Schlichting, R. L. Shoeman, L. Lomb, M. Frank, M. Liang, and H. N. Chapman, *Phys. Rev. Lett.* **104**, 225501 (2010). DOI: 10.1103/PhysRevLett.104.225501.
- [74] K. Ayyer, T.-Y. Lan, V. Elser, and N. D. Loh, *J. Appl. Cryst.* **49**, 1320 (2016). DOI: 10.1107/S1600576716008165.
- [75] K. Ayyer, A. J. Morgan, A. Aquila, H. DeMirci, B. G. Hogue, R. A. Kirian, P. L. Xavier, C. H. Yoon, H. N. Chapman, and A. Barty, *Opt. Exp.* **27**, 37816 (2019). DOI: 10.1364/oe.27.037816.
- [76] Y. Zhuang, S. Awel, A. Barty, R. Bean, J. Bielecki, M. Bergemann, B. J. Daurer, T. Ekeberg, A. D. Estillore, H. Fangohr, K. Giewekemeyer, M. S. Hunter, M. Karnevskiy, R. A. Kirian, H. Kirkwood, Y. Kim, J. Koliyadu, H. Lange, R. Letrun, J. Lübke, A. Mall, T. Michelat, A. J. Morgan, N. Roth, A. K. Samanta, T. Sato, Z. Shen, M. Sikorski, F. Schulz, J. C. H. Spence, P. Vagovic, T. Wollweber, L. Worbs, P. L. Xavier, O. Yefanov, F. R. N. C. Maia, D. A. Horke, J. Küpper, N. D. Loh, A. P. Mancuso, H. N. Chapman, and K. Ayyer, *IUCrJ* **9**, 204 (2022). DOI: 10.1107/S2052252521012707.
- [77] P. J. Ho, B. J. Daurer, M. F. Hantke, J. Bielecki, A. Al Haddad, M. Bucher, G. Doumy, K. R. Ferguson, L. Flückiger, T. Gorkhover, B. Iwan, C. Knight, S. Moeller, T. Osipov, D. Ray, S. H. Southworth, M. Svenda, N. Timneanu, A. Ulmer, P. Walter, J. Hajdu, L. Young, F. R. N. C. Maia, and C. Bostedt, *Nat. Commun.* **11**, 167 (2020). DOI: 10.1038/s41467-019-13905-9.
- [78] T. Ekeberg, M. Svenda, C. Abergel, F. R. N. C. Maia, V. Seltzer, J.-M. Claverie, M. Hantke, O. Jönsson, C. Nettelblad, G. van der Schot, M. Liang, D. P. Deponte, A. Barty, M. M. Seibert, B. Iwan, I. Andersson, N. D. Loh, A. V. Martin, H. Chapman, C. Bostedt, J. D. Bozek, K. R. Ferguson, J. Krzywinski, S. W. Epp, D. Rolles, A. Rudenko, R. Hartmann, N. Kimmel, and J. Hajdu, *Phys. Rev. Lett.* **114**, 098102 (2015). DOI: 10.1103/PhysRevLett.114.098102.
- [79] I. V. Lundholm, J. A. Sellberg, T. Ekeberg, M. F. Hantke, K. Okamoto, G. van der Schot, J. Andreasson, A. Barty, J. Bielecki, P. Bruza, M. Bucher, S. Carron, B. J. Daurer, K. Ferguson, D. Hasse, J. Krzywinski, D. S. D. Larsson, A. Morgan, K. Mühlig, M. Müller, C. Nettelblad, A. Pietrini, H. K. N. Reddy, D. Rupp, M. Sauppe, M. Seibert, M. Svenda, M. Swiggers, N. Timneanu, A. Ulmer, D. Westphal, G. Williams, A. Zani, G. Faigel, H. N. Chapman, T. Möller, C. Bostedt, J. Hajdu, T. Gorkhover, and F. R. N. C. Maia, *IUCrJ* **5**, 531 (2018). DOI: 10.1107/S2052252518010047.
- [80] T. Ekeberg, D. Assalauova, J. Bielecki, R. Boll, B. J. Daurer, L. A. Eichacker, L. E. Franken, D. E. Galli, L. Gelisio, L. Gumprecht, L. H. Gunn, J. Hajdu, R. Hartmann, D. Hasse, A. Ignatenko, J. Koliyadu, O. Kulyk, R. Kurta, M. Kuster, W. Lugmayr, J. Lübke, A. P. Mancuso, T. Mazza, C. Nettelblad, Y. Ovcharenko, D. E. Rivas, M. Rose, A. K. Samanta, P. Schmidt, E. Sobolev, N. Timneanu, S. Usenko, D. Westphal, T. Wollweber, L. Worbs, P. L. Xavier, H. Yousef, K. Ayyer, H. N. Chapman, J. A. Sellberg, C. Seuring, I. A. Vartanyants, J. Küpper, M. Meyer, and F. R. Maia, *bioRxiv* (2022). DOI: 10.1101/2022.03.09.483477.

- [81] K. Ayyer, P. L. Xavier, J. Bielecki, Z. Shen, B. J. Daurer, A. K. Samanta, S. Awel, R. Bean, A. Barty, M. Bergemann, T. Ekeberg, A. D. Estillore, H. Fangohr, K. Giewekemeyer, M. S. Hunter, M. Karneviskiy, R. A. Kirian, H. Kirkwood, Y. Kim, J. Koliyadu, H. Lange, R. Letrun, J. Lübke, T. Michelat, A. J. Morgan, N. Roth, T. Sato, M. Sikorski, F. Schulz, J. C. H. Spence, P. Vagovic, T. Wollweber, L. Worbs, O. Yefanov, Y. Zhuang, F. R. N. C. Maia, D. A. Horke, J. Küpper, N. D. Loh, A. P. Mancuso, and H. N. Chapman, *Optica* **8**, 15 (2021). DOI: 10.1364/OPTICA.410851.
- [82] D. Höing, R. Salzwedel, L. Worbs, Y. Zhuang, A. Samanta, J. Lübke, A. D. Estillore, K. Dlugolecki, C. Passow, B. Erk, N. Ekanayake, D. Ramm, J. Correa, C. C. Papadopoulou, A. T. Noor, F. Schulz, M. Selig, A. Knorr, K. Ayyer, J. Küpper, and H. Lange, *Optically induced electron density gradients drive coherent plasmonic nanoparticle oscillations* (2022), in preparation.
- [83] A. Hosseinizadeh, G. Mashayekhi, J. Copperman, P. Schwander, A. Dashti, S. Sepehr, R. Fung, M. Schmidt, C. H. Yoon, B. G. Hogue, G. J. Williams, A. Aquila, and A. Ourmazd, *Nat. Methods* **14**, 877 (2017). DOI: 10.1038/nmeth.4395.
- [84] J. C. H. Spence, *IUCrJ* **4**, 322 (2017). DOI: 10.1107/S2052252517005760.
- [85] J. C. Williamson, J. M. Cao, H. Ihee, H. Frey, and A. H. Zewail, *Nature* **386**, 159 (1997). DOI: 10.1038/386159a0.
- [86] T. Mandl, C. Östlin, I. E. Dawod, M. N. Brodmerkel, E. G. Marklund, A. V. Martin, N. Timneanu, and C. Caleman, *J. Phys. Chem. Lett.* **11**, 6077 (2020). DOI: 10.1021/acs.jpcllett.0c01144.
- [87] T. Meyer, V. Gabelica, H. Grubmüller, and M. Orozco, *Wiley Interdiscip. Rev.-Comput. Mol. Sci.* **3**, 408 (2013). DOI: 10.1002/wcms.1130.
- [88] G. Walsh, *Proteins: Biochemistry and Biotechnology* (John Wiley & Sons, 2014), 2nd ed., ISBN 978-0-470-66986-0. DOI: 10.1002/9781119117599.
- [89] A. Maisser, V. Premnath, A. Ghosh, T. A. Nguyen, M. Attoui, and C. J. Hogan Jr., *Phys. Chem. Chem. Phys.* **13**, 21630 (2011). DOI: 10.1039/c1cp22127b.
- [90] S. Tamara, M. A. den Boer, and A. J. R. Heck, *Chem. Rev.* **122**, 7269 (2022). DOI: 10.1021/acs.chemrev.1c00212.
- [91] B. Domon and R. Aebersold, *Science* **312**, 212 (2006). DOI: 10.1126/science.1124619.
- [92] H. Borsdorf and G. A. Eiceman, *Appl. Spectr. Rev.* **41**, 323 (2006). DOI: 10.1080/05704920600663469.
- [93] W. Jung, P. V. Pikhitsa, Y.-H. Jung, J. Shin, M. Han, and M. Choi, *Acc. Mater. Res.* **2**, 1117 (2021). DOI: 10.1021/accountsmr.1c00187.
- [94] N. Teschmit, D. A. Horke, and J. Küpper, *Angew. Chem. Int. Ed.* **57**, 13775 (2018). DOI: 10.1002/anie.201807646.

-
- [95] P. Atkins and J. de Paula, *Physical Chemistry* (Oxford University Press, 2006), 8th ed.
- [96] H. Stöcker, *Taschenbuch der Physik* (Verlag Harri Deutsch, Frankfurt a. M., Germany, 1994), 2nd ed., ISBN 3-8171-1358-7.
- [97] W. Demtröder, *Experimentalphysik 2*, vol. 2 (Springer, Berlin Heidelberg New York, 2013), 6th ed. DOI: 10.1007/978-3-642-29944-5.
- [98] W. Demtröder, *Experimentalphysik 3*, vol. 3 (Springer, Berlin Heidelberg New York, 2010), 4th ed. DOI: 10.1007/978-3-642-03911-9.
- [99] R. A. Millikan, *Science* **32**, 436 (1910). DOI: 10.1126/science.32.822.436.
- [100] C. E. Felder, J. Prilusky, I. Silman, and J. L. Sussman, *Nucleic Acids Res.* **35**, W512 (2007). DOI: 10.1093/nar/gkm307.
- [101] J. W. Strutt, 3rd Baron Rayleigh, *Phil. Mag.* **5**, 184 (1882). DOI: 10.1080/14786448208628425.
- [102] A. di Biasio, L. Ambrosone, and C. Cametti, *J. Phys. D* **46**, 055305 (2013). DOI: 10.1088/0022-3727/46/5/055305.
- [103] D. Juba, D. J. Audus, M. Mascagni, J. F. Douglas, and W. Keyrouz, *J. Res. Nat. Inst. Stand. Tech.* **122**, 20 (2017). DOI: 10.6028/jres.122.020.
- [104] M. Amin, H. Samy, and J. Küpper, *J. Phys. Chem. Lett.* **10**, 2938 (2019). DOI: 10.1021/acs.jpcclett.9b00963.
- [105] L. Holmegaard, J. H. Nielsen, I. Nevo, H. Stapelfeldt, F. Filsinger, J. Küpper, and G. Meijer, *Phys. Rev. Lett.* **102**, 023001 (2009). DOI: 10.1103/PhysRevLett.102.023001.
- [106] Y.-P. Chang, D. A. Horke, S. Trippel, and J. Küpper, *Int. Rev. Phys. Chem.* **34**, 557 (2015). DOI: 10.1080/0144235X.2015.1077838.
- [107] W. Gordy and R. L. Cook, *Microwave Molecular Spectra* (John Wiley & Sons, New York, NY, USA, 1984), 3rd ed.
- [108] J. S. Kienitz, K. Długołęcki, S. Trippel, and J. Küpper, *J. Chem. Phys.* **147**, 024304 (2017). DOI: 10.1063/1.4991479.
- [109] E. Gershnel and I. S. Averbukh, *J. Chem. Phys.* **134**, 054304 (2011). DOI: 10.1063/1.3535600.
- [110] B. Friedrich and D. Herschbach, *J. Phys. Chem.* **99**, 15686 (1995). DOI: 10.1021/j100042a051.
- [111] H. Kallmann and F. Reiche, *Z. Phys.* **6**, 352 (1921). DOI: 10.1007/BF01327996.
- [112] E. Wrede, *Z. Phys.* **44**, 261 (1927). DOI: 10.1007/BF01391193.

- [113] L. Ploenes, P. Straňák, H. Gao, J. Küpper, and S. Willitsch, *Mol. Phys.* **119**, e1965234 (2021). DOI: 10.1080/00268976.2021.1965234.
- [114] J. van Veldhoven, H. L. Bethlem, and G. Meijer, *Phys. Rev. Lett.* **94**, 083001 (2005). DOI: 10.1103/PhysRevLett.94.083001.
- [115] M. Lemeshko, R. V. Krems, J. M. Doyle, and S. Kais, *Mol. Phys.* **111**, 1648 (2013). DOI: 10.1080/00268976.2013.813595.
- [116] H. L. Bethlem, M. R. Tarbutt, J. Küpper, D. Carty, K. Wohlfart, E. A. Hinds, and G. Meijer, *J. Phys. B* **39**, R263 (2006). DOI: 10.1088/0953-4075/39/16/R01.
- [117] C. F. Bohren and D. R. Huffman, *Absorption and Scattering of Light by Small Particles* (John Wiley & Sons, 1998).
- [118] M. F. Hantke, J. Bielecki, O. Kulyk, D. Westphal, D. S. D. Larsson, M. Svenda, H. K. N. Reddy, R. A. Kirian, J. Andreasson, J. Hajdu, and F. R. N. C. Maia, *IUCrJ* **5**, 673 (2018). DOI: 10.1107/S2052252518010837.
- [119] R. C. Weast, *Handbook of Chemistry and Physics* (CRC Press, Boca Raton, U.S.A., 1979), 59th ed., ISBN 9780849304590.
- [120] F. Schulz, C. Abergel, and T. Woyke, *Nat. Rev. Microbiol.* **in print**, online version (2022). DOI: 10.1038/s41579-022-00754-5.
- [121] A. M. Gañán-Calvo, *Phys. Rev. Lett.* **80**, 285 (1998). DOI: 10.1103/PhysRevLett.80.285.
- [122] D. P. DePonte, U. Weierstall, K. Schmidt, J. Warner, D. Starodub, J. C. H. Spence, and R. B. Doak, *J. Phys. D* **41**, 195505 (2008). DOI: 10.1088/0022-3727/41/19/195505.
- [123] R. B. Doak, J. C. H. Spence, U. Weierstall, D. Deponte, D. Starodub, and J. S. Warner, *Gas dynamic virtual nozzle for generation of microscopic droplet streams*, World Intellectual Property Organization (2008), patent no. WO 2009/091416 A2.
- [124] K. R. Beyerlein, L. Adriano, M. Heymann, R. Kirian, J. Knoska, F. Wilde, H. N. Chapman, and S. Bajt, *Rev. Sci. Instrum.* **86**, 125104 (2015). DOI: 10.1063/1.4936843.
- [125] E. Sobolev, S. Zolotarev, K. Giewekemeyer, J. Bielecki, K. Okamoto, H. K. N. Reddy, J. Andreasson, K. Ayer, I. Barak, S. Bari, A. Barty, R. Bean, S. Bobkov, H. N. Chapman, G. Chojnowski, B. J. Daurer, K. Dörner, T. Ekeberg, L. Flückiger, O. Galzitskaya, L. Gelisio, S. Hauf, B. G. Hogue, D. A. Horke, A. Hosseinizadeh, V. Ilyin, C. Jung, C. Kim, Y. Kim, R. A. Kirian, H. Kirkwood, O. Kulyk, R. Letrun, D. Loh, M. Messerschmidt, K. Mühlig, A. Ourmazd, N. Raab, A. V. Rode, M. Rose, A. Round, T. Sato, R. Schubert, P. Schwander, J. A. Sellberg, M. Sikorski, A. Silenzi, C. Song, J. C. H. Spence, S. Stern, J. Sztuk-Dambietz, A. Teslyuk, N. Timneanu, M. Trebbin, C. Uetrecht, B. Weinhausen, G. J. Williams, P. L. Xavier, C. Xu, I. Vartanyants, V. Lamzin, A. Mancuso, and F. R. N. C. Maia, *Comm. Phys* **3**, 97 (2020). DOI: 10.1038/s42005-020-0362-y.

-
- [126] K. Mühlig, A. M. Gañán-Calvo, J. Andreasson, D. S. D. Larsson, J. Hajdu, and M. Svenda, *J. Appl. Cryst.* **52**, 800 (2019). DOI: 10.1107/S1600576719008318.
- [127] R. A. Kirian, S. Awel, N. Eckerskorn, H. Fleckenstein, M. Wiedorn, L. Adriano, S. Bajt, M. Barthelmess, R. Bean, K. R. Beyerlein, L. M. G. Chavas, M. Domaracky, M. Heymann, D. A. Horke, J. Knoska, M. Metz, A. Morgan, D. Oberthuer, N. Roth, T. Sato, P. L. Xavier, O. Yefanov, A. V. Rode, J. Küpper, and H. N. Chapman, *Struct. Dyn.* **2**, 041717 (2015). DOI: 10.1063/1.4922648.
- [128] R. Nazari, S. Zaare, R. C. Alvarez, K. Karpos, T. Engelman, C. Madsen, G. Nelson, J. C. H. Spence, U. Weierstall, R. J. Adrian, and R. A. Kirian, *Opt. Express* **28**, 21749 (2020). DOI: 10.1364/OE.390131.
- [129] R. P. Kurta, J. J. Donatelli, C. H. Yoon, P. Berntsen, J. Bielecki, B. J. Daurer, H. DeMirici, P. Fromme, M. F. Hantke, F. R. N. C. Maia, A. Munke, C. Nettelblad, K. Pande, H. K. N. Reddy, J. A. Sellberg, R. G. Sierra, M. Svenda, G. van der Schot, I. A. Vartanyants, G. J. Williams, P. L. Xavier, A. Aquila, P. H. Zwart, and A. P. Mancuso, *Phys. Rev. Lett.* **119**, 158102/1 (2017). DOI: 10.1103/PhysRevLett.119.158102.
- [130] M. F. Hantke, D. Hasse, M. R. N. C, T. Ekeberg, K. John, M. Svenda, N. D. Loh, A. V. Martin, N. Timneanu, L. S. D, van der SchotGijs, G. H. Carlsson, M. Ingelman, J. Andreasson, D. Westphal, M. Liang, F. Stellato, D. P. DePonte, R. Hartmann, N. Kimmel, R. A. Kirian, M. M. Seibert, K. Mühlig, S. Schorb, K. Ferguson, C. Bostedt, S. Carron, J. D. Bozek, D. Rolles, A. Rudenko, S. Epp, H. N. Chapman, A. Barty, J. Hajdu, and I. Andersson, *Nat. Photon.* **8**, 943 (2014). DOI: doi:10.1038/nphoton.2014.270.
- [131] K. J. Light-Wahl, B. L. Schwartz, and R. D. Smith, *J. Am. Chem. Soc.* **116**, 5271 (1994). DOI: 10.1021/ja00091a035.
- [132] T. Soga and D. N. Heiger, *Anal. Chem.* **72**, 1236 (2000). DOI: 10.1021/ac990976y.
- [133] S. Sanglier, E. Leize, A. v. Dorsselaer, and F. Zal, *J. Am. Soc. Mass Spectrom.* **14**, 419 (2003). DOI: 10.1016/s1044-0305(03)00131-4.
- [134] L. Konermann, *J. Am. Soc. Mass Spectrom.* **28**, 1827 (2017). DOI: 10.1007/s13361-017-1739-3.
- [135] P. Kebarle and U. H. Verkerk, *A Brief Overview of the Mechanisms Involved in Electrospray Mass Spectrometry* (Wiley-VCH, Weinheim, Germany, 2010), pp. 1–35, ISBN 978-3-527-32351-7, URL https://application.wiley-vch.de/books/sample/3527323511_c01.pdf.
- [136] S. I. Johnson, M. D. Baer, and S. Raugei, *J. Phys. Chem. A* **126**, 44 (2022). DOI: 10.1021/acs.jpca.1c08795.
- [137] S. Warnke, G. von Helden, and K. Pagel, *J. Am. Chem. Soc.* **135**, 1177 (2013). DOI: 10.1021/ja308528d.

- [138] E. G. Marklund, D. S. D. Larsson, D. van der Spoel, A. Patriksson, and C. Caleman, *Phys. Chem. Chem. Phys.* **11**, 8069 (2009). DOI: 10.1039/B903846A.
- [139] D. van der Spoel, E. G. Marklund, D. S. D. Larsson, and C. Caleman, *Macromol. Biosci.* **11**, 50 (2011). DOI: 10.1002/mabi.201000291.
- [140] J. Bielecki, M. F. Hantke, B. J. Daurer, H. K. N. Reddy, D. Hasse, D. S. D. Larsson, L. H. Gunn, M. Svenda, A. Munke, J. A. Sellberg, L. Flueckiger, A. Pietrini, C. Nettelblad, I. Lundholm, G. Carlsson, K. Okamoto, N. Timneanu, D. Westphal, O. Kulyk, A. Higashiura, G. van der Schot, N.-T. D. Loh, T. E. Wysong, C. Bostedt, T. Gorkhover, B. Iwan, M. M. Seibert, T. Osipov, P. Walter, P. Hart, M. Bucher, A. Ulmer, D. Ray, G. Carini, K. R. Ferguson, I. Andersson, J. Andreasson, J. Hajdu, and F. R. N. C. Maia, *Science Advances* **5**, eaav8801 (2019). DOI: 10.1126/sciadv.aav8801.
- [141] S. Kassemeyer, J. Steinbrener, L. Lomb, E. Hartmann, A. Aquila, A. Barty, A. V. Martin, C. Y. Hampton, S. Bajt, M. Barthelmess, T. R. Barends, C. Bostedt, M. Bott, J. D. Bozek, N. Coppola, M. Cryle, D. P. DePonte, R. B. Doak, S. W. Epp, B. Erk, H. Fleckenstein, L. Foucar, H. Graafsma, L. Gumprecht, A. Hartmann, R. Hartmann, G. Hauser, H. Hirsemann, A. Hömke, P. Holl, O. Jönsson, N. Kimmel, F. Krasniqi, M. Liang, F. R. Maia, S. Marchesini, K. Nass, C. Reich, D. Rolles, B. Rudek, A. Rudenko, C. Schmidt, J. Schulz, R. L. Shoeman, R. G. Sierra, H. Soltau, J. C. H. Spence, D. Starodub, F. Stellato, S. Stern, G. Stier, M. Svenda, G. Weidenspointner, U. Weierstall, T. A. White, C. Wunderer, M. Frank, H. N. Chapman, J. Ullrich, L. Strüder, M. J. Bogan, and I. Schlichting, *Opt. Exp.* **20**, 4149 (2012). DOI: 10.1364/OE.20.004149.
- [142] B. J. Daurer, K. Okamoto, J. Bielecki, F. R. N. C. Maia, K. Mühlig, M. M. Seibert, M. F. Hantke, C. Nettelblad, W. H. Benner, M. Svenda, N. Timneanu, T. Ekeberg, N. D. Loh, A. Pietrini, A. Zani, A. D. Rath, D. Westphal, R. A. Kirian, S. Awel, M. O. Wiedorn, G. van der Schot, G. H. Carlsson, D. Hasse, J. A. Sellberg, A. Barty, J. Andreasson, S. Boutet, G. Williams, J. Koglin, I. Andersson, J. Hajdu, and D. S. D. Larsson, *IUCrJ* **4**, 251 (2017). DOI: 10.1107/S2052252517003591.
- [143] J. He and D. C. Joy, *Scanning* Vol. **25**, 285 (2003). DOI: 10.1002/sca.4950250603.
- [144] I. A. Kaltashov and A. Mohimen, *Anal. Chem.* **77**, 5370 (2005). DOI: 10.1021/ac050511+.
- [145] M. Dole, L. Mack, R. Hines, R. Mobley, L. Ferguson, and M. d. Alice, *J. Chem. Phys.* **49**, 2240 (1968).
- [146] L. Konermann, E. Ahadi, A. D. Rodriguez, and S. Vahidi, *Anal. Chem.* **85**, 2 (2013), PMID: 23134552. DOI: 10.1021/ac302789c.
- [147] S. Banerjee, H. Prakash, and S. Mazumdar, *J. Am. Soc. Mass Spectrom.* **22**, 1707 (2011). DOI: 10.1007/s13361-011-0188-7.
- [148] L. Konermann, H. Metwally, Q. Duez, and I. Peters, *Analyst* **144**, 6157 (2019). DOI: 10.1039/C9AN01201J.

-
- [149] L. B. Modesto-Lopez, E. M. Kettleison, and P. Biswas, *J. Electrostat.* **69**, 357 (2011). DOI: 10.1016/j.elstat.2011.04.014.
- [150] *Advanced Electrospray Aerosol Generator Model 3482*, TSI Incorporated, manual p/n 6007732, “B” ed. (2014).
- [151] A. Wiedensohler, E. Lütkeemeier, M. Feldpausch, and C. Helsper, *J. Aerosol. Sci.* **17**, 413 (1986). DOI: 10.1016/0021-8502(86)90118-7.
- [152] A. Wiedensohler, *J. Aerosol. Sci.* **19**, 387 (1988). DOI: 10.1016/0021-8502(88)90278-9.
- [153] N. A. Fuchs, *Geofis. pura appl.* **56**, 185 (1988). DOI: 10.1007/bf01993343.
- [154] P. H. McMurry, *Aerosols - Observations and Measurements* (Adv. Phys., Cambridge, USA, 2003), pp. 20–34, ISBN 9780122270901, URL <https://doi.org/10.1016/B0-12-227090-8/00048-8>.
- [155] H. Wu, R. Zhang, W. Zhang, and J. Hong, *Chem. Sci.* **11**, 4758 (2020). DOI: 10.1039/D0SC01965H.
- [156] M. Li, J. Tan, M. J. Tarlov, and M. R. Zachariah, *Anal. Chem.* **86**, 12130 (2014). DOI: 10.1021/ac5030123.
- [157] M. U. H. Mir, J. K. Maurya, S. Ali, S. Ubaid-ullah, A. B. Khan, and R. Patel, *Process Biochem.* **49**, 623 (2014). DOI: 10.1016/j.procbio.2014.01.020.
- [158] L. Ban, F. van Swaaij, S. Fazzolari, and R. Signorell (2022), in press, URL <https://doi.org/10.1016/j.jaerosci.2022.106080>.
- [159] N. Roth, D. Horke, J. Lübke, A. K. Samanta, A. D. Estillore, L. Worbs, N. Pohlman, K. Ayyer, A. Morgan, H. Fleckenstein, M. Domaracky, B. Erk, C. Passow, J. Correa, O. Yefanov, A. Barty, M. Prasciolu, S. Bajt, R. Kirian, H. Chapman, and J. Küpper (2021), in preparation, 2012.11237.
- [160] M. M. Seibert, T. Ekeberg, F. R. N. C. Maia, M. Svenda, J. Andreasson, O. Jönsson, D. Odić, B. Iwan, A. Rocker, D. Westphal, M. Hantke, D. P. Deponte, A. Barty, J. Schulz, L. Gumprecht, N. Coppola, A. Aquila, M. Liang, T. A. White, A. Martin, C. Caleman, S. Stern, C. Abergel, V. Seltzer, J.-M. Claverie, C. Bostedt, J. D. Bozek, S. Boutet, A. A. Miahnahri, M. Messerschmidt, J. Krzywinski, G. Williams, K. O. Hodgson, M. J. Bogan, C. Y. Hampton, R. G. Sierra, D. Starodub, I. Andersson, S. Bajt, M. Barthelmess, J. C. H. Spence, P. Fromme, U. Weierstall, R. Kirian, M. Hunter, R. B. Doak, S. Marchesini, S. P. Hau-Riege, M. Frank, R. L. Shoeman, L. Lomb, S. W. Epp, R. Hartmann, D. Rolles, A. Rudenko, C. Schmidt, L. Foucar, N. Kimmel, P. Holl, B. Rudek, B. Erk, A. Hömke, C. Reich, D. Pietschner, G. Weidenspointner, L. Strüder, G. Hauser, H. Gorke, J. Ullrich, I. Schlichting, S. Herrmann, G. Schaller, F. Schopper, H. Soltau, K.-U. Kühnel, R. Andritschke, C.-D. Schröter, F. Krasniqi, M. Bott, S. Schorb, D. Rupp, M. Adolph, T. Gorkhover, H. Hirsemann, G. Potdevin, H. Graafsma, B. Nilsson, H. N. Chapman, and J. Hajdu, *Nature* **470**, 78 (2011). DOI: 10.1038/nature09748.
-

- [161] L. Worbs, J. Lübke, A. D. Estillore, A. K. Samanta, and J. Küpper, *J. Phys. Chem. C* (2022), in preparation.
- [162] N. Roth, S. Awel, D. A. Horke, and J. Küpper, *J. Aerosol. Sci.* **124**, 17 (2018). DOI: 10.1016/j.jaerosci.2018.06.010.
- [163] L. Worbs, N. Roth, J. Lübke, A. D. Estillore, P. L. Xavier, A. K. Samanta, and J. Küpper, *J. Appl. Cryst.* **54**, 1730 (2021). DOI: 10.1107/S1600576721009973.
- [164] L. Worbs, J. Lübke, N. Roth, A. K. Samanta, D. A. Horke, and J. Küpper, *Opt. Exp.* **27**, 36580 (2019). DOI: 10.1364/OE.27.036580.
- [165] *Prime 95B: Customer Applications Handbook*, Teledyne Photometrics, Tucson, AZ, USA (2019).
- [166] B. P. Marsh, N. Chada, R. R. Sanganna Gari, K. P. Sigdel, and G. M. King, *Sci. Rep.* **8**, 978 (2018). DOI: 10.1038/s41598-018-19379-x.
- [167] J. M. Yon, *J. Cell. Mol. Med.* **6**, 307 (2002). DOI: 10.1111/j.1582-4934.2002.tb00511.x.
- [168] R. D. Sleator, *Bioeng. Bugs* **3**, 80 (2012). DOI: 10.4161/bbug.18303.
- [169] K. Rogers, in *Encyclopedia Britannica* (Encyclopædia Britannica, Inc., 2016), ISBN 978-1-59339-292-5, accessed 2022-06-14, URL <https://www.britannica.com/science/biomolecule>.
- [170] N. L. Craig, R. Green, C. Greider, G. Storz, C. Wolberger, and O. Cohen-Fix, *Molecular Biology - Principles of Genome Function* (Oxford University Press, 2021), 3rd ed., ISBN 978-0-19-878865-2.
- [171] E. Buxbaum, *Fundamentals of Protein Structure and Function* (Springer Verlag, 2015), 2nd ed., ISBN 978-3-319-19920-7. DOI: 10.1007/978-3-319-19920-7.
- [172] T. Hachiya, I. Terashima, and K. Noguchi, *Plant Cell Environ.* **30**, 1269 (2007). DOI: 10.1111/j.1365-3040.2007.01701.x.
- [173] A. Tiessen, P. Pérez-Rodríguez, and L. J. Delaye-Arredondo, *BMC Res. Notes* **5**, 85 (2012). DOI: 10.1186/1756-0500-5-85.
- [174] E. J. Stollar and D. P. Smith, *Essays Biochem.* **64**, 649 (2020). DOI: 10.1042/EBC20190042.
- [175] K. Linderstrøm-Lang, *C. R. Trav. Lab. Carlsberg* **15**, 1 (1924).
- [176] C. Tanford, *Adv. Protein Chem.* **17**, 69 (1963). DOI: 10.1016/S0065-3233(08)60052-2.
- [177] H. J. Cleaves, in *Encyclopedia of Astrobiology* (Springer Verlag, 2011), ISBN 978-3-642-11274-4, URL https://doi.org/10.1007/978-3-642-11274-4_819.

-
- [178] X. Xia, in *Bioinformatics and the Cell* (Springer Verlag, 2007), ISBN 978-0-387-71337-3, URL <https://link.springer.com/book/10.1007/978-0-387-71337-3>.
- [179] I. Gitlin, J. D. Carbeck, and G. M. Whitesides, *Angew. Chem. Int. Ed.* **45**, 3022 (2006). DOI: 10.1002/anie.200502530.
- [180] A. M. Gañán-Calvo, *J. Aerosol. Sci.* **30**, 863 (1999). DOI: 10.1016/S0021-8502(98)00780-0.
- [181] L. Landau and E. Lifshitz, *Chapter I - Electrostatics of Conductors* (Pergamon, Kronberg-Taunus, Germany, 1984), vol. 8 of *Course of Theoretical Physics*, pp. 1–33, 2nd ed., ISBN 0-08-030275-0, URL <https://doi.org/10.1016/B978-0-08-030275-1.50007-2>.
- [182] J. D. Carbeck, J. C. Severs, J. Gao, Q. Wu, R. D. Smith, and G. M. Whitesides, *J. Phys. Chem. B* **102**, 10596 (1998). DOI: 10.1021/jp980768u.
- [183] M. Hautreux, N. Hue, A. du Fou de Kerdaniel, A. Zahir, V. Malec, and O. Laprévôte, *Int. J. Mass Spectrom.* **231**, 131 (2004). DOI: 10.1016/j.ijms.2003.10.009.
- [184] M. L. Abramsson, C. Sahin, J. T. S. Hopper, R. M. M. Branca, J. Danielsson, M. Xu, S. A. Chandler, N. Österlund, L. L. Ilag, A. Leppert, J. Costeira-Paulo, L. Lang, K. Teilum, A. Laganowsky, J. L. P. Benesch, M. Oliveberg, C. V. Robinson, E. G. Marklund, T. M. Allison, J. R. Winther, and M. Landreh, *JACS Au* **1**, 2385 (2021). DOI: 10.1021/jacsau.1c00458.
- [185] M. I. Catalina, R. H. H. van den Heuvel, E. van Duijn, and A. J. R. Heck, *Chem. Eur. J* **11**, 960 (2005). DOI: 10.1002/chem.200400395.
- [186] Scientific Instrument Services Inc., USA, *Simion 8.1* (2011), URL: <http://simion.com>.
- [187] S. Welker, M. Amin, and J. Küpper, *Comp. Phys. Comm.* **270**, 108138 (2022). DOI: 10.1016/j.cpc.2021.108138.
- [188] *Python Language Reference, v3.8*, Python Software Foundation (2019), URL <https://www.python.org>.
- [189] L. Worbs, Dissertation, Universität Hamburg, Hamburg, Germany (2022), in preparation.
- [190] M. J. Bogan, W. H. Benner, S. Boutet, U. Rohner, M. Frank, A. Barty, M. M. Seibert, F. Maia, S. Marchesini, S. Bajt, B. Woods, V. Riot, S. P. Hau-Riege, M. Svenda, E. Marklund, E. Spiller, J. Hajdu, and H. N. Chapman, *Nano Lett.* **8**, 310 (2008). DOI: 10.1021/nl072728k.
- [191] A. Barty, J. Küpper, and H. N. Chapman, *Annu. Rev. Phys. Chem.* **64**, 415 (2013). DOI: 10.1146/annurev-physchem-032511-143708.
-

- [192] I. Martiel, H. M. Müller-Werkmeister, and A. E. Cohen, *Acta Cryst. D* **75**, 160 (2019). DOI: 10.1107/S2059798318017953.
- [193] K. Ayyer, *Optica* **7**, 593 (2020). DOI: 10.1364/OPTICA.391373.
- [194] X. Han, W.-H. Shin, C. W. Christoffer, G. Terashi, L. Monroe, and D. Kihara, in *Encyclopedia of Bioinformatics and Computational Biology*, edited by S. Ranganathan, M. Gribskov, K. Nakai, and C. Schönbach (Adv. Phys., 2019), pp. 606–619, ISBN 978-0-12-811432-2, URL <https://www.sciencedirect.com/science/article/pii/B9780128096338201489>.
- [195] A. M. R. de Graff, M. J. Hazoglou, and K. A. Dill, *Structure* **24**, 329 (2016). DOI: 10.1016/j.str.2015.11.006.
- [196] A. C. Leney and A. J. R. Heck, *J. Am. Soc. Mass Spectrom.* **28**, 5 (2017). DOI: 10.1007/s13361-016-1545-3.
- [197] C. Santambrogio, A. Natalello, S. Brocca, E. Ponzini, and R. Grandori, *Proteomics* **19**, 1800060 (2018). DOI: 10.1002/pmic.201800060.
- [198] M. Bierwirth, M. Gensch, and A. P. Weber, *Chem. Ing. Tech.* **93**, 1 (2021). DOI: 10.1002/cite.202000196.
- [199] S. Awel, R. A. Kirian, M. O. Wiedorn, K. R. Beyerlein, N. Roth, D. A. Horke, D. Oberthür, J. Knoska, V. Mariani, A. Morgan, L. Adriano, A. Tolstikova, P. L. Xavier, O. Yefanov, A. Aquila, A. Barty, S. Roy-Chowdhury, M. S. Hunter, D. James, J. S. Robinson, U. Weierstall, A. V. Rode, S. Bajt, J. Küpper, and H. N. Chapman, *J. Appl. Cryst.* **51**, 133 (2018). DOI: 10.1107/S1600576717018131.
- [200] P. Liu, P. J. Ziemann, D. B. Kittelson, and P. H. McMurry, *Aerosol Sci. Techn.* **22**, 293 (1995). DOI: 10.1080/02786829408959748.
- [201] S. Awel, R. A. Kirian, N. Eckerskorn, M. Wiedorn, D. A. Horke, A. V. Rode, J. Küpper, and H. N. Chapman, *Opt. Exp.* **24**, 6507 (2016). DOI: 10.1364/OE.24.006507.
- [202] P. Virtanen, R. Gommers, T. E. Oliphant, M. Haberland, T. Reddy, D. Cournapeau, E. Burovski, P. Peterson, W. Weckesser, J. Bright, S. J. van der Walt, M. Brett, J. Wilson, K. Jarrod Millman, N. Mayorov, A. R. J. Nelson, E. Jones, R. Kern, E. Larson, C. Carey, Í. Polat, Y. Feng, E. W. Moore, J. VanderPlas, D. Laxalde, J. Perktold, R. Cimrman, I. Henriksen, E. A. Quintero, C. R. Harris, A. M. Archibald, A. H. Ribeiro, F. Pedregosa, P. van Mulbregt, and SciPy 1.0 Contributors, *Nat. Methods* **17**, 261 (2020). DOI: 10.1038/s41592-019-0686-2.
- [203] M. Yang, *Appl. Econ. Lett.* **15**, 737 (2008). DOI: 10.1080/13504850600749073.
- [204] J. Haeberle, A. Schella, M. Sperl, M. Schröter, and P. Born, *Soft Matter* **14**, 4987 (2018). DOI: 10.1039/C8SM00603B.

-
- [205] N. A. Heckert, J. J. Filliben, C. M. Croarkin, B. Hembree, W. F. Guthrie, P. Tobias, and J. Prins, *NIST/SEMATECH e-Handbook of Statistical Methods* (NIST, 2002), accessed 2020-12-16.
- [206] K. A. Baggerly, *Cytometry* **45**, 141 (2001). DOI: 10.1002/1097-0320(20011001)45:2<141::aid-cyto1156>3.0.co;2-m.
- [207] A. Fernández Barbero, R. Martínez García, M. A. Cabrerizo Vílchez, and R. Hidalgo-Alvarez, *Colloids Surf. A Physicochem. Eng. Asp.* **92**, 121 (1994). DOI: 10.1016/0927-7757(94)02829-X.
- [208] P. E. Shaw, *Nature* **118**, 659 (1926). DOI: 10.1038/118659c0.
- [209] T. Shinbrot, T. S. Komatsu, and Q. Zhao, *Europhys. Lett.* **83**, 24004/p1 (2008). DOI: 10.1209/0295-5075/83/24004.
- [210] R. Pham, R. C. Virnelson, R. M. Sankaran, and D. J. Lacks, *J. Electrostat.* **69**, 456 (2011). DOI: 10.1016/j.elstat.2011.05.003.
- [211] C. Xu, B. Zhang, A. C. Wang, H. Zou, G. Liu, W. Ding, C. Wu, M. Ma, P. Feng, Z. Lin, and Z. L. Wang, *ACS Nano* **13**, 2034 (2019). DOI: 10.1021/acsnano.8b08533.
- [212] J. L. Carneiro, Bachelor's thesis, Technische Hochschule Ostwestfalen-Lippe (2022).
- [213] C. Larriba and J. F. de la Mora, *J. Phys. Chem. B* **116**, 593 (2012). DOI: 10.1021/jp2092972.
- [214] J. B. Fenn, M. Mann, C. K. Meng, S. F. Wong, and C. M. Whitehouse, *Science* **246**, 64 (1989). DOI: 10.1126/science.2675315.
- [215] R. D. Smith, J. A. Loo, C. G. Edmonds, C. J. Barinaga, and H. R. Udseth, *Anal. Chem.* **62**, 882 (1990). DOI: 10.1021/ac00208a002.
- [216] G. R. D. Prabhu, V. K. Ponnusamy, H. A. Witek, and P. L. Urban, *Anal. Chem.* **92**, 13042 (2020). DOI: 10.1021/acs.analchem.0c01945.
- [217] J. Lübke, N. Roth, L. Worbs, D. A. Horke, A. D. Estillore, A. K. Samanta, and J. Küpper, *J. Phys. Chem. C* **125**, 25794 (2021). DOI: 10.1021/acs.jpcc.1c06912.
- [218] C. Östlin, N. Timneanu, C. Caleman, and A. V. Martin, *Struct. Dyn.* **6**, 044103 (2019). DOI: 10.1063/1.5098309.
- [219] F. R. N. C. Maia, T. Ekeberg, D. Nicușor Tîmneanu, van der Spoel, and J. Hajdu, *Phys. Rev. E* **80**, 031905 (2009). DOI: 10.1103/PhysRevE.80.031905.
- [220] D.-R. Chen, D. Y. Pui, and S. L. Kaufman, *J. Aerosol. Sci.* **26**, 963 (1995). DOI: [http://dx.doi.org/10.1016/0021-8502\(95\)00027-A](http://dx.doi.org/10.1016/0021-8502(95)00027-A).
- [221] S. M. Kaufman, *J. Aerosol. Sci.* **29**, 537—552 (1998). DOI: 10.1016/S0021-8502(97)00462-X.

- [222] P. D. Schnier, D. S. Gross, and E. R. Williams, *J. Am. Chem. Soc.* **117**, 6747 (1995). DOI: 10.1021/ja00130a015.
- [223] Y. Mao, J. Woenckhaus, J. Kolafa, M. A. Ratner, and M. F. Jarrold, *J. Am. Chem. Soc.* **121**, 2712 (1999). DOI: 10.1021/ja980324b.
- [224] Y. Zhong, L. Han, and B. T. Ruotolo, *Angew. Chem. Int. Ed.* **53**, 9209 (2014). DOI: 10.1002/anie.201403784.
- [225] W. E. Royer Jr., H. Sharma, K. Strand, J. E. Knapp, and B. Bhyravbhatla, *Structure* **14**, 1167 (2006). DOI: 10.1016/j.str.2006.05.011.
- [226] E. V. Asadollaheia and M. Gamero-Castaño, *AIP Adv.* **9**, 125006 (2019). DOI: 10.1063/1.5128113.
- [227] R. Ahmed and R. Gopalakrishnan, *J. Aerosol. Sci.* **137**, 105443 (2019). DOI: 10.1016/j.jaerosci.2019.105443.
- [228] K. Raspe, M. Müller, N. Iwe1, R. N. Wolf, P. Oelßner, F. Martinez, L. Schweikhard, K.-H. Meiwes-Broer, and J. Tiggesbäumker, *Rev. Sci. Instrum.* **93**, 043301 (2022). DOI: 10.1063/5.0085187.
- [229] Z. Li, L. Shi, L. Cao, Z. Liu, and J. Küpper, *Phys. Rev. Appl.* **11**, 064036 (2019). DOI: 10.1103/PhysRevApplied.11.064036.
- [230] P. L. Xavier, H. N. Chapman, S. Bajt, M. S. Hunter, A. V. Martin, T. Grant, J. Küpper, J. Lübke, and A. K. Samanta (2022), in preparation.
- [231] H. Hernández and C. V. Robinson, *Nat. Protoc.* **2**, 715 (2007). DOI: 10.1038/nprot.2007.73.
- [232] J. Stetefeld, S. A. McKenna, and T. R. Patel, *Biophys. Rev.* **8**, 409–427 (2016). DOI: 10.1007/s12551-016-0218-6.
- [233] S. Trippel, M. Johny, T. Kierspel, J. Onvlee, H. Bieker, H. Ye, T. Mullins, L. Gumprecht, K. Długolecki, and J. Küpper, *Rev. Sci. Instrum.* **89**, 096110 (2018). DOI: 10.1063/1.5026145.
- [234] G. Ben-Nissan and M. Sharon, *Curr. Opin. Chem. Biol.* **42**, 25 (2018). DOI: 10.1016/j.cbpa.2017.10.026.
- [235] A. Kadek, K. Lorenzen, and C. Uetrecht, *Drug Discov. Today Technol.* **39**, 89 (2021). DOI: 10.1016/j.ddtec.2021.07.001.
- [236] F. A. Mellon, *Mass Spectrometry - Principles and Instrumentation* (Adv. Phys., Cambridge, USA, 2003), pp. 3739–3749, ISBN 978-0-12-227055-0, URL <https://doi.org/10.1016/B0-12-227055-X/00746-X>.
- [237] C. Uetrecht, K. Lorenzen, M. Kitel, J. Heidemann, J. H. Robinson Spencer, H. Schlüter, and J. Schulz, *J. Synchrotron Rad.* **26**, 653 (2019). DOI: 10.1107/S1600577519002686.

-
- [238] C. Brand, B. A. Stickler, C. Knobloch, A. Shayeghi, K. Hornberger, and M. Arndt, *Phys. Rev. Lett.* **121**, 173002 (2018). DOI: 10.1103/PhysRevLett.121.173002.
- [239] D. Suckau, Y. Shi, S. C. Beu, M. W. Senko, J. P. Quinn, F. M. Wampler 3rd, and F. W. McLafferty, *PNAS* **90**, 790 (1993). DOI: 10.1073/pnas.90.3.790.
- [240] P. A. Sullivan, J. Axelsson, S. Altmann, A. P. Quist, B. U. Sunqvist, and C. T. Reimann, *J. Am. Soc. Mass Spectrom.* **7**, 329 (1996). DOI: 10.1016/1044-0305(95)00702-4.
- [241] F. Filsinger, U. Erlekam, G. von Helden, J. Küpper, and G. Meijer, *Phys. Rev. Lett.* **100**, 133003 (2008). DOI: 10.1103/PhysRevLett.100.133003.
- [242] F. Filsinger, J. Küpper, G. Meijer, J. L. Hansen, J. Maurer, J. H. Nielsen, L. Holmegaard, and H. Stapelfeldt, *Angew. Chem. Int. Ed.* **48**, 6900 (2009). DOI: 10.1002/anie.200902650.
- [243] M. Johny, J. Onvlee, T. Kierspel, H. Bieker, S. Trippel, and J. Küpper, *Chem. Phys. Lett.* **721**, 149–152 (2019). DOI: 10.1016/j.cplett.2019.01.052.
- [244] M. J. Wieduwilt and M. M. Moasser, *Cell. Mol. Life Sci.* **65**, 1566 (2008). DOI: 10.1007/s00018-008-7440-8.
- [245] L. Orellana, *Front. Mol. Biosci.* **6**, 117 (2019). DOI: 10.3389/fmolb.2019.00117.
- [246] A. J. de Nijs and H. L. Bethlem, *Phys. Chem. Chem. Phys.* **13**, 19052 (2011). DOI: 10.1039/c1cp21477b.
- [247] N. F. Ramsey, *Molecular Beams*, The International Series of Monographs on Physics (Oxford University Press, London, GB, 1956), reprinted in *Oxford Classic Texts in the Physical Sciences* (2005).
- [248] K. Ferguson, M. Berger, J. Mendrola, H. Cho, D. Leahy, and M. Lemmon, *Mol. Cell* **11**, 507 (2003). DOI: 10.1016/S1097-2765(03)00047-9.
- [249] C. Lu, L.-Z. Mi, M. J. Grey, J. Zhu, E. Graef, S. Yokoyama, and T. A. Springer, *Mol. Cell. Biol.* **30**, 5432 (2010). DOI: 10.1128/MCB.00742-10.
- [250] C. H. Townes and A. L. Schawlow, *Microwave Spectroscopy* (Dover Publications, New York, 1975), ISBN 048661798X.
- [251] A. D. McNaught and A. Wilkinson, *IUPAC. Compendium of Chemical Terminology (the “Gold Book”)* (Blackwell Scientific Publications, Oxford, UK, 1997), 2nd ed., ISBN 0-9678550-9-8, online version published 2019, created by S. J. Chalk. DOI: 10.1351/goldbook.
- [252] A. K. Samanta, M. Amin, A. D. Estillore, N. Roth, L. Worbs, D. A. Horke, and J. Küpper, *Struct. Dyn.* **7**, 024304 (2020). DOI: 10.1063/4.0000004.
- [253] L. Worbs, A. D. Estillore, S. K. Peravali, A. K. Samanta, and J. Küpper, *Rev. Sci. Instrum.* (2022), in preparation.

- [254] A. S. Chatterley, C. Schouder, L. Christiansen, B. Shepperson, M. H. Rasmussen, and H. Stapelfeldt, *Nat. Commun.* **10**, 133 (2019). DOI: 10.1038/s41467-018-07995-0.
- [255] V. Loriot, P. Tzallas, E. P. Benis, E. Hertz, B. Lavorel, D. Charalambidis, and O. Faucher, *J. Phys. B* **40**, 2503 (2007).
- [256] E. Peronne, M. Poulsen, C. Bisgaard, H. Stapelfeldt, and T. Seideman, *Phys. Rev. Lett.* **91**, 04300 (2003). DOI: 10.1103/PhysRevLett.91.043003.
- [257] T. Mullins, E. T. Karamatskos, J. Wiese, J. Onvlee, A. Rouzée, A. Yachmenev, S. Trippel, and J. Küpper, *Nat. Commun.* **13**, 1431 (2022). DOI: 10.1038/s41467-022-28951-z.
- [258] J. Küpper, S. Stern, L. Holmegaard, F. Filsinger, A. Rouzée, A. Rudenko, P. Johnsson, A. V. Martin, M. Adolph, A. Aquila, S. Bajt, A. Barty, C. Bostedt, J. Bozek, C. Caleman, R. Coffee, N. Coppola, T. Delmas, S. Epp, B. Erk, L. Foucar, T. Gorkhover, L. Gumprecht, A. Hartmann, R. Hartmann, G. Hauser, P. Holl, A. Hömke, N. Kimmel, F. Krasniqi, K.-U. Kühnel, J. Maurer, M. Messerschmidt, R. Moshhammer, C. Reich, B. Rudek, R. Santra, I. Schlichting, C. Schmidt, S. Schorb, J. Schulz, H. Soltau, J. C. H. Spence, D. Starodub, L. Strüder, J. Thøgersen, M. J. J. Vrakking, G. Weidenspointner, T. A. White, C. Wunderer, G. Meijer, J. Ullrich, H. Stapelfeldt, D. Rolles, and H. N. Chapman, *Phys. Rev. Lett.* **112**, 083002 (2014). DOI: 10.1103/PhysRevLett.112.083002.
- [259] M. Faubel, S. Schlemmer, and J. P. Toennies, *Z. Phys. D* **10**, 269 (1988). DOI: 10.1007/BF01384861.
- [260] C. Vega and E. de Miguel, *J. Chem. Phys.* **126**, 154707 (2007). DOI: 10.1063/1.2715577.
- [261] Ø. Wilhelmsen, D. Bedeaux, and D. Reguera, *J. Chem. Phys.* **142**, 171103 (2015). DOI: 10.1063/1.4919689.
- [262] R. C. Tolman, *J. Chem. Phys.* **17**, 333 (1949). DOI: 10.1063/1.1747247.
- [263] M. H. Factorovich, V. Molinero, and D. A. Scherlis, *J. Am. Chem. Soc.* **136**, 4508 (2014). DOI: 10.1021/ja405408n.
- [264] D. Schlesinger, J. A. Sellberg, A. Nilsson, and L. G. M. Petterson, *J. Chem. Phys.* **144**, 124502 (2016). DOI: 10.1063/1.4944387.
- [265] F. O. Goodman and H. Y. Wachman, *Dynamics of Gas-Surface Scattering* (Adv. Phys., 1976), ISBN 0-12-290450-8.
- [266] B. P. E. Clapeyron, *J. E. Polytech.* **14**, 153 (1834).
- [267] H. Sippola and P. Taskinen, *J. Chem. Eng. Data* **63**, 2986 (2018). DOI: 10.1021/acs.jced.8b00251.

- [268] M. J. Chase, *NIST-JANAF Thermochemical Tables, 4th edition* (American Institute of Physics, 1998).
- [269] U. Weierstall, R. B. Doak, J. C. H. Spence, D. Starodub, D. Shapiro, P. Kennedy, J. Warner, G. G. Hembree, P. Fromme, and H. N. Chapman, *Exp. Fluids* **44**, 675 (2008). DOI: 10.1007/s00348-007-0426-8.
- [270] C. Goy, M. A. C. Potenza, S. Dederá, M. Tomut, E. Guillermin, A. Kalinin, K.-O. Voss, A. Schottelius, N. Petridis, A. Prosvetov, G. Tejada, J. M. Fernández, C. Trautmann, F. Caupin, U. Glasmacher, and R. E. Grisenti, *Phys. Rev. Lett.* **120**, 015501 (2020). DOI: 10.1103/PhysRevLett.120.015501.
- [271] G. Rovelli, M. I. Jacobs, M. D. Willis, R. J. Rapf, A. M. Prophet, and K. R. Wilson, *Chem. Sci.* **11**, 13026 (2020). DOI: 10.1039/d0sc04611f.
- [272] J. Finneran, C. P. Garner, and F. Nadal, *Proc. R. Soc. A* **477**, 20210078 (2021). DOI: 10.1098/rspa.2021.0078.
- [273] D. Jakubczyk, M. Kolwas, G. Derkachov, K. Kolwas, and M. Zientara, *Acta Phys. Pol. A* **122**, 709 (2012). DOI: 10.12693/APhysPolA.122.709.
- [274] Y. Shechtman, *Biophys. Rev.* **12**, 1303 (2020). DOI: 10.1007/s12551-020-00773-7.
- [275] J. Lübke, L. P. Xavier, L. Worbs, H. N. Chapman, A. K. Samanta, and J. Küpper (2022), in preparation.

Eidesstattliche Versicherung / Declaration on Oath

Hiermit versichere ich an Eides statt, dass ich die vorliegende Dissertation selbst verfasst und keine anderen als die angegebenen Quellen und Hilfsmittel benutzt habe. Ich versichere, dass das in elektronischer Form eingereichte Dissertationsexemplar (über den Docata-Upload) und das bei der Fakultät (zuständiges Studienbüro bzw. Promotionsbüro Physik) zur Archivierung eingereichte gedruckte gebundene Exemplar der Dissertationsschrift identisch sind.

I hereby declare upon oath that I have written the present dissertation independently and have not used further resources and aids than those stated in the dissertation. I, the undersigned, declare that the dissertation submitted in electronic form (via the Docata upload) and the printed bound copy of the dissertation submitted to the faculty (responsible Academic Office or the Doctoral Office Physics) for archiving are identical.

Hamburg, 09.10.2022

Jannik Lübke